Master's thesis

Square-waves and pulsating dynamics in time-delayed active micro-cavities

Submitted by

Elias R. Koch

September 14, 2022

First examiner
PD Dr. Svetlana Gurevich

Second examiner
Prof. Dr. Julien Javaloyes

Westfälische Wilhelms-Universität Münster
Fachbereich Physik
Institut für Theoretische Physik

Contents

1. Introduction

Throughout the last decades, time-delayed systems (TDSs) have gained a large significance within different fields of nonlinear science. So-called delay-differential equations (DDEs) are not only able to describe a multitude of physical systems very accurately, but often they even contain observed dynamics which cannot be described by simpler approaches. A simple example is the occurrence of oscillations in a one-dimensional first-order ordinary differential equation, which is not possible until a delay is introduced. This can be seen by considering an equation

$$\dot{x}(t) = -x(t), \tag{1.1}$$

which simply describes the decay of an amplitude $x(t_0)$ into the fixed point $x = 0$. Just from imagination, there is no way to get from one side of the stable fixed point to the other without passing the fixed point. To get any kind of oscillation, at least a second degree of freedom is needed, e.g. a second component or a second derivative, which can be rewritten as a two-dimensional dynamical system. In both cases, the system can oscillate by circling the unstable fixed point in the phase plane as it is the case for the conversion of potential into kinetic energy in the case of a harmonic oscillator. Including a single delay time into Eq. (1.1) leads to

$$\dot{x}(t) = -x(t - \tau), \tag{1.2}$$

where τ is called the delay. Starting with an adequate deviation from the fixed point, the system will not converge to the fixed point, but pass it, since the rate of change does not depend on the current state but the history of the system. By looking closely one can also notice that this is not a one-dimensional system in the sense of degrees of freedom. Indeed, the system is infinite dimensional, since its initial condition needs to be defined on a continuous interval $t \in [-\tau, 0]$ [Ern08]. The number of initial conditions needed to initialize the system, always equals the number of degrees of freedom the system has.
Most real-world systems depend on the exchange of some type of information, which takes a finite amount of time. Interactions and processes do not happen instantaneously, which results in the current rate of change of a state depending on past states. In many physical systems, however, the resulting effects are considered to be small and are thus neglected. If the delay τ is small compared to all other time scales in the system, this becomes a valid approximation. For example Eq. (1.2) approaches Eq. (1.1) in the limit of short delays. If, however, the time-delay becomes a relevant time scale it can drastically influence the system's behavior.
A little toy example is the description of a shower [Ern08] which always takes a finite time to adjust to a set temperature. If one sets a desired temperature T_0, water with that temperature enters the shower hose and takes a time τ to come out of the shower. Thus, if someone constantly increases the set temperature until feeling the desired temperature T_0, he will surpass T_0 due to the delay. Here, the delay effects depend on the velocity or intensity at which the person spins the water tap in response to the temperature difference. This is due to the system having two time scales: The time scale on which the tap is spun and the delay time. If the delay time becomes a relevant time scale, delay effects such as oscillations between hot and cold water can occur.
Note, that a DDE could potentially depend on several delays. Thus, a DDE in its general form can be written as

$$\dot{x}(t) = f(x(t), x(t - \tau_1), ..., x(t - \tau_N), t), \tag{1.3}$$

where x could be a state vector of any dimension. The initial condition for such a DDE has to have the length of the longest delay.
There are many important fields, for which delay effects are of relevance, such as climate models, where delayed feedback loops can play a role in transport times of mass or energy [KKP17]. Here, DDEs have been used to, e.g., model the global energy balance or the El Nino Southern Oscillation system. Delayed systems have also been used in economics, to include the influence of the time-delay between the initiation of production and the delivery of goods on price fluctuations of commodities [Mac89], since supply usually will not follow demand instantaneously. Another very intuitive example is traffic flow, which is largely influenced by driver's reaction times [Oro+09][OWS10]. In machine learning, DDEs have found increasing attention lately as well, e.g. in a method that allows reducing a large deep neural network into a single neuron using time-delayed feedback with multiple delay times [Ste+21]. These examples are only a few amongst many. In this thesis, however, the focus will be on time-delayed models in laser physics, where they are widely used for different laser systems such as ring cavities, passive-mode locking in semiconductor lasers, and employing external cavities as feedback loops in general [Ike79] [RBM11][Reb+11][LK80].
To get an initial insight into the use of TDS in the modeling of laser systems, consider a laser cavity containing circulating modes of an electric field. These modes will return to any point after one round-trip. Hence the resulting electric field depends on the current state as well as states from past round-trips [Sch21]. The inclusion of time-delays allows modeling these effects, serving as a natural boundary condition for the field. As a result, DDEs could be used successfully, to describe e.g. passive-mode locking in semiconductor lasers [VT05]. But time-delay can also be introduced in the modeling of external feedback, as it is used in Vertical-external-cavity surface-emitting lasers (VECSELs) [Tro+04]. This is based on the idea, that part of the output of a laser cavity can be reinjected, for example by using constructions such as fiber loops or external cavities. Assuming that the light takes a time τ to travel towards the point where it reenters the cavity, the injection at time t depends on the output at time $t-\tau$. External time-delayed feedback allows to control pulse-shape stabilizing terms such as second and third order dispersion [Sch+19a][Sch+20][Sch+19b][HGJ21]. Finally, by adding a phase at the feedback mirror within an external cavity, antiresonant feedback can be found, which allows for the formation of stable plateau solutions such as square-waves (SWs).
TDSs are also known for being rich in fascinating dynamics. Interesting behavior such as temporal localized structures [JAH15], coarsening [Gia+12] and pattern formation [YG14], as well as concepts like Eckhaus instability [WY06], chimera states [LPM13], e.g. when periodicity and chaos coexist, or chaos [Doy82][YLM93] has been shown in different applications.

1.1. Outline

Within this thesis the dynamics of square-waves (SWs) and pulsating periodic solutions are discussed and analyzed. After the foregoing short introduction Section 2 will give an overview over theoretical concepts and knowledge that is a prerequisite or at least helpful for the understanding of this thesis and its context. It also contains a detailed derivation of the systems that are analyzed in later sections. In Section 3, a short introduction to the numerical methods used to contain the results presented in this work will be given. Section 4 contains the analysis and discussion of the dynamics of SWs in a Kerr Gires-Tournois interferometer (KGTI) which is a delay algebraic equation (DAE) system and the main topic of this thesis. Using a combination of bifurcation analyses and analytical calculations SWs are systematically described over extended parameter regimes. In this context, two different mechanisms of SW formation are introduced. Furthermore, the arising of period doubling routes to chaos as well as multi-plateau SWs are discussed. Finally, the dynamics of more complex patterns consisting of temporal localized structures of different sizes that are written on plateau values of stable SWs are considered. Note that some of the results presented here have also been published recently [Koc+22].
In Section 5 a second system is introduced. It is similar to the KGTI, however the Kerr nonlinearity is replaced by a quantum well which is mathematically described by a new and more complex susceptibility. Hence, the system is called Quantum well Gires-Tournois interferometer (QGTI). Different parameter regimes are discussed for the higher dimensional parameter space of this system and it is related to the KGTI and the results found there. Dark and bright pulses as well as SWs are found and described for the QGTI using numerical path continuation.
Motivated by the observation of periodic solutions in a limit of small cavity losses, a normal form is derived in this limit in Section 6. The resulting partial differential equation (PDE) system can help to give a better understanding of the systems dynamics and the contributions of the involved parameters since it can be compared to other well known PDEs describing pattern formation in nonlinear physics. The section closes with an analysis of the PDE system trying to reproduce results such as temporal localized states (TLSs) that have been observed in the QGTI system before. Section 7, finally, will contain a short summary and an outlook on potential further research based on the results provided in this thesis.

2. Theoretical Preliminary Remarks

2.1. Dynamical Systems and Stability

Most complex dynamics in nonlinear physics are mathematically modeled by dynamical systems. A dynamical system can be described by a set of evolution equations with an initial condition, i.e.

$$\dot{\boldsymbol{x}}(t) = \boldsymbol{F}(\boldsymbol{x}(t), t, \boldsymbol{\mu}), \quad \boldsymbol{x_0} = \boldsymbol{x}(t_0), \tag{2.1}$$

where $\boldsymbol{x}(t)$ is a state vector and $\boldsymbol{\mu}$ a vector of parameters. A solution of this dynamical system has to satisfy both, the evolution equation and the initial condition. In general, physical systems are not described as first-order differential equations with the harmonic oscillator as a well known example. Consider a differential equation of order n, where $x^{(n)}$ describes the n-th time derivative such as

$$x^{(n)} = f(x(t), x^{(1)}(t), ..., x^{(n-1)}(t), t, \boldsymbol{\mu}). \tag{2.2}$$

A trajectory solving this equation can be identified with a curve $c(t)$ in the n-dimensional vector space with variables $c_i = x^{(i)}$, $i = \{0, ..., n-1\}$. The curve can be received using a substitution $c_i = x^{(i)}$ which leads to a new system of n first order differential equations

$$\dot{c}_{n-1}(t) = f(c_0(t), c_1(t), ..., c_{n-1}(t), t, \boldsymbol{\mu}), \tag{2.3}$$
$$\dot{c}_{n-2}(t) = c_{n-1}(t), \tag{2.4}$$
$$..., \tag{2.5}$$
$$\dot{c}_0(t) = c_1(t). \tag{2.6}$$

The corresponding trajectory $c(t)$ lives in the so-called phase space. While it is generally complicated or even impossible to fully solve a nonlinear dynamical system, the toolbox of nonlinear physics allows to understand a lot about the system without knowing its exact solutions. Starting by interpreting $\boldsymbol{F}$ as a vector field in the mentioned phase space the uniqueness and existence theorem ensures that every initial condition has a definite future. It effectively demands that the above described dynamical system $\boldsymbol{F}$ and all it's partial derivatives $\frac{\partial \boldsymbol{F}}{\partial x_i}(\boldsymbol{x}, t, \boldsymbol{\mu})$ are continuous for $\boldsymbol{x} \in \mathbb{R}^n$ on an open and connected set $D \subset \mathbb{R}^n$. Then, if $\boldsymbol{x_0} \in D$ it ensures a unique solution curve $\boldsymbol{x}(t)$ on a time interval starting from the initial time t_0 [Str18][LS88]. This theorem implies that trajectories never intersect. The vector field may then have certain attracting and repelling manifolds. If an initial condition lies in the basin of attraction of an invariant manifold, it will converge towards it, which allows to describe the behavior of the system in the long-term limit without actually solving it. The manifolds with the lowest dimension are so-called fixed points x^* that fulfill $0 = \boldsymbol{F}(\boldsymbol{x}^*, t, \boldsymbol{\mu})$.
A one-dimensional manifold that can act as an attractor is for example a limit cycle, while a two-dimensional attractor is for example a torus. Further, attractors with fractal dimensions can be found corresponding to chaotic long-term behavior. However, these are not of importance for this thesis.
In many cases there is no interest in the transient solutions of a system describing the trajectory towards some attractor, but in the stable solutions approached in the long-term limit. Thus, from now on the term solution will always refer to a settled solution such as $\boldsymbol{x}^*$ satisfying $\boldsymbol{F}(\boldsymbol{x}^*, t, \boldsymbol{\mu}) = 0$, while other solutions of $\dot{\boldsymbol{x}}(t) = \boldsymbol{F}(\boldsymbol{x}(t), t, \boldsymbol{\mu})$ will be called a point on a trajectory. In order to calculate the stability of such a solution the linear stability analysis is introduced, where the solution is perturbed by a small $\boldsymbol{\delta}(t)$.

Inserting $\boldsymbol{x}(t) = \boldsymbol{x}^* + \boldsymbol{\delta}(t)$ as a solution and expanding the system for a small perturbation up to linear order yields the linearized time evolution of the perturbation which is an eigenvalue equation. The resulting eigenvalues reveal whether the perturbation decays or grows corresponding to unstable or stable solutions, respectively. This leads to

$$\dot{\boldsymbol{\delta}}(t) = \boldsymbol{F}(\boldsymbol{x}^*, t, \boldsymbol{\mu}) + (\boldsymbol{\nabla F})(\boldsymbol{x}, t, \boldsymbol{\mu})|_{\boldsymbol{x}=\boldsymbol{x}^*}\boldsymbol{\delta}(t) + \mathcal{O}(\delta^2) \tag{2.7}$$

$$= (\boldsymbol{\nabla F})(\boldsymbol{x}, t, \boldsymbol{\mu}))|_{\boldsymbol{x}=\boldsymbol{x}^*}\boldsymbol{\delta}(t) + \mathcal{O}(\delta^2). \tag{2.8}$$

Considering a system that does not depend on time explicitly, the Jacobian matrix $\boldsymbol{\mathcal{L}} = (\boldsymbol{\nabla F})(\boldsymbol{x}^*)$ becomes a constant quantity since the dynamics on a fixed point are time independent. This equation can be solved using an exponential ansatz $\boldsymbol{\delta}(t) = \boldsymbol{\delta}_0 e^{\lambda t}$, which transforms the first order differential equation into an eigenvalue equation. $\boldsymbol{\mathcal{L}}$ is generally an $n \times n$ matrix, and $\boldsymbol{\delta}_0$ an n-component vector, for an n-dimensional system. Thus, n eigenvalues and respective eigenvectors can be found. The eigenvalues describe the time evolution around the fixed points in the local manifolds spanned by the eigenvectors. In a two-dimensional case, the eigenvalues can be calculated from the matrix $\boldsymbol{\mathcal{L}}$ by

$$\lambda_\pm = \frac{1}{2}\left[\mathrm{tr} \pm \sqrt{\mathrm{tr}^2 - 4\mathrm{det}}\right], \tag{2.9}$$

where tr and det are the trace and determinant of $\mathcal{L}$, respectively. A negative real part of the eigenvalues generally belongs to a stable solution, while a solution with a positive real part is unstable. In at least two-dimensional systems complex conjugated eigenvalues can be found as well, where the imaginary part describes a frequency. In that case, the trajectory oscillates around the fixed point, where a positive or negative real part leads to an outward or inward spiral in the phase space, respectively.

To determine the linear stability of periodic solutions $x^*(t) = x^*(t+T)$ in an n-dimensional phase space, Floquet theory can be used [Str18][Arg+15]. Consider an $n-1$ dimensional surface S which is transverse to the flow, meaning that all trajectories, in particular the periodic solution, cut it in only one point. So a periodic orbit in the n-dimensional phase space corresponds to a fixed point $\boldsymbol{x}^*$ on the Poincare map. To determine the linear stability of the periodic orbit, the linear stability of the fixed point can be calculated. Firstly, an initial condition $\boldsymbol{x}^* + \boldsymbol{\delta}_0$ will be introduced, which is slightly perturbed from the fixed point on the surface S.
Now the interest is in the perturbation occurring after one round-trip of the flow. To get there, one shall introduce the Poincare map $\boldsymbol{\mathcal{P}}$, which is defined as

$$\boldsymbol{x}^* + \boldsymbol{\delta}_1 = \boldsymbol{\mathcal{P}}(\boldsymbol{x}^* + \boldsymbol{\delta}_0). \tag{2.10}$$

The Poincare map can be linearized using the definition $\boldsymbol{x}^* = \boldsymbol{\mathcal{P}}(\boldsymbol{x}^*)$ of a fixed point on S, leading to

$$\boldsymbol{x}^* + \boldsymbol{\delta}_1 = \boldsymbol{x}^* + (\boldsymbol{\nabla \mathcal{P}})(\boldsymbol{x}^*) \cdot \boldsymbol{\delta}_0 + \mathrm{h.o.t.}, \tag{2.11}$$

where $\boldsymbol{\mathcal{J}}(\boldsymbol{x}^*)$ is the Jacobian of the Poincare map at the fixed point. This equation yields

$$\boldsymbol{\delta}_1 = \boldsymbol{\mathcal{J}}(\boldsymbol{x}^*)\boldsymbol{\delta}_0. \tag{2.12}$$

The eigenvalues λ_i of this so-called monodromie matrix [Arg+15] are the Floquet multipliers of the periodic solution. Since they describe a map, the absolute value of the

eigenvalues determines the stability, where $|\lambda_i| < 1$ describes a decaying perturbation for that eigenvector, while $|\lambda_i| > 1$ describes a growing perturbation. In general, only if $|\lambda_i| < 1$ for all $i = 1, ..., n-1$, the corresponding periodic solution is linearly stable, although there is always one multiplier with $\lambda = 1$, which describes perturbations that occur along the periodic solution [Str18]. While this section rather aimed at introducing the concepts and terminology of dynamical systems and stability, the resulting analyses themselves tend to get more complicated for DDEs. The characteristic equation arising in a linear stability analysis, e.g., is transcendental [Ern08] describing the infinite dimensional nature of DDE systems. Thus, numerical methods are needed to investigate time-delayed systems effectively.

2.2. Bifurcations

A bifurcation describes a substantial change in topology of the phase space due to a change in parameters. To get a better understanding of this phenomenon, a system with a single control parameter μ is introduced. Now the evolution of the phase space topology shall be investigated if this parameter is varied. Any regular solution $(\boldsymbol{x}^*, \mu^*)$ for $0 = \boldsymbol{F}(\boldsymbol{x}^*, \mu^*)$ is part of a unique one-dimensional continuum of states in μ, which is called a solution branch [Thi21]. This is, due to this equation proposing an implicit function. The implicit function theorem [KP02] predicts a unique solution $(\boldsymbol{x}^*, \mu^*)$ with a unique continuation for any implicit function, if the systems Jacobian $\boldsymbol{\mathcal{L}}(\boldsymbol{x}^*, \mu^*)$ is of full rank at this point. This condition is equivalent to all eigenvalues being unequal to zero. Most solutions along a branch fulfill this requirement and the Jacobian is invertible almost everywhere. This is different at bifurcation points since they break with uniqueness. As a solution branches into two, the continuation of a solution is not unique. Since also solutions change their stability, at least one eigenvalue crosses the imaginary axis. This enables a reduced description of dynamics in the vicinity of the bifurcation point, since the real part becomes small, which corresponds to very slow dynamics. A separation of time scales is found, where all trajectories rapidly fall onto the so-called center manifold, which is tangential to the eigenspace of the slow eigenvalue. As a result, one can describe the behavior close to bifurcations with simplified normal forms, which are one-dimensional differential equations, that contain the dynamics on the center manifold. These also help with the identification and classification of bifurcations, even in complicated systems. Within this section the most important types of bifurcations for this thesis will be introduced.

2.2.1. Saddle-Node Bifurcation

The saddle-node bifurcation is a major mechanism for the creation or annihilation of fixed points. It is described by the normal form

$$\dot{x} = \mu - x^2. \tag{2.13}$$

The Jacobian of this system is $\mathcal{J} = -2x$. This reduced dynamical system has no real solutions for $\mu < 0$. In this parameter regime, the one-dimensional flow pulls any initial condition $x(t_0)$ towards positive x values. At $\mu = 0$ a saddle-node bifurcation appears, thus the Jacobian $\mathcal{J}(0) = 0$ is not invertible. The only eigenvalue of the linearized system is here zero, which means that the flow becomes infinitely slow around the bifurcation point, which is a preparation for the change of the flow direction between the two fixed points after the bifurcation. For $\mu > 0$ two fixed points $x^* = \pm\sqrt{\mu}$ are found. In the one-dimensional case, the Jacobian equals the eigenvalues, so $x^* = \sqrt{\mu}$ is the stable

fixed point due to the negative eigenvalue, while $x^* = -\sqrt{\mu}$ is unstable. All in all, at a saddle-node bifurcation two steady states are created, where one is stable and one unstable.
There is a saddle-node bifurcation of cycles as well, which is also referred to as fold bifurcation. It occurs, when two cycles are created or collide and annihilate. This bifurcation will be observed several times throughout this thesis. As a bifurcation of periodic orbits, it can be seen in the Floquet multipliers, when a real multiplier crosses the point $\lambda = 1$, as shown in Fig. 2.2 b). Since a Floquet multiplier describes, how a perturbation evolves after each repetition on a periodic orbit, a positive real multiplier corresponds to monotonous growth or decay if it is out of or within the unit circle.

2.2.2. Hopf and Torus Bifurcations

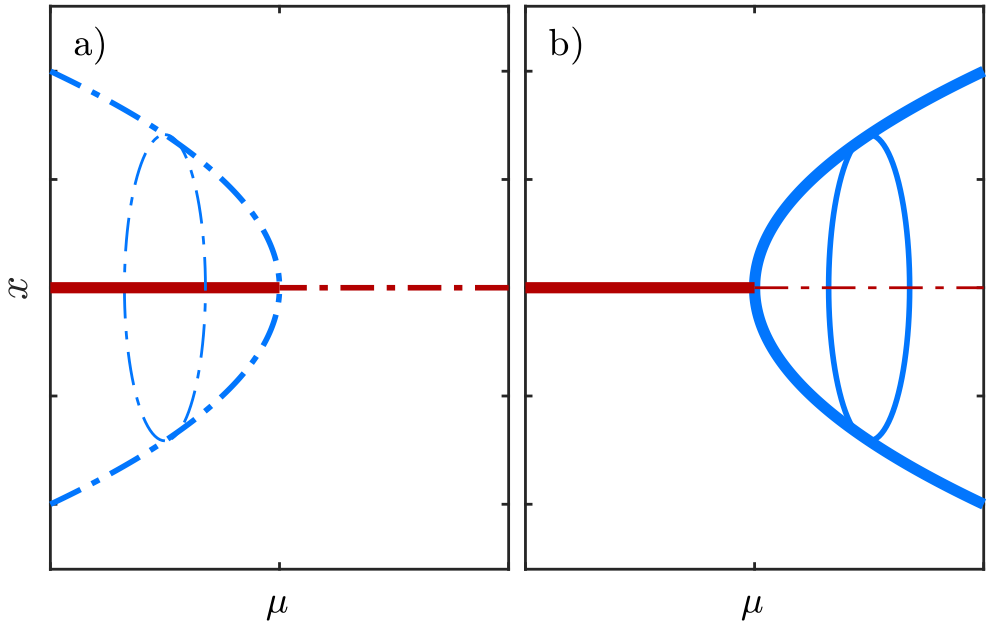

Figure 2.1: a) Subcritical Hopf bifurcation where a stable fixed point collides with an unstable limit cycle, losing stability in the process. b) Supercritical Hopf bifurcation where a stable fixed point loses stability, creating a stable limit cycle.

The Hopf bifurcation is another bifurcation occurring on fixed point branches, that can only be found in an at least two-dimensional phase space. This is due to the need for two complex conjugated eigenvalues for this type of bifurcation. Two types of Hopf bifurcations are to be distinguished, both shown in Fig. 2.1: In a supercritical Hopf bifurcation a) a stable fixed point loses stability in favor of a periodic limit cycle, which is created in the bifurcation point, while in a subcritical Hopf bifurcation b) an unstable fixed point becomes stable by creating an unstable limit cycle. In polar coordinates, the normal form for the supercritical Hopf bifurcation reads

$$\dot{r} = \mu r - r^3, \tag{2.14}$$

$$\dot{\theta} = \omega + br^2, \tag{2.15}$$

where μ determines the stability of the fixed point, while ω is the frequency of the smallest limit cycle and ultimately b gives a frequency dependence on the amplitude. Although the radius r is positive here, the first equation gives the normal form of a so-called supercritical pitchfork bifurcation, which describes the creation of two stable fixed points, when a third fixed point in the origin loses stability. Rewriting the system in Cartesian coordinates yields the Jacobian matrix

$$\mathcal{J} = \begin{bmatrix} \mu & -\omega \\ \omega & \mu \end{bmatrix} \tag{2.16}$$

which has the eigenvalues

$$\lambda_{\pm} = \mu \pm i\omega. \tag{2.17}$$

Hence, for $\mu = 0$ a Hopf bifurcation occurs when two complex conjugated eigenvalues cross the imaginary axis. A small perturbation oscillates around the fixed point. The real part μ switches sign at the Hopf bifurcation point, which corresponds to the transition from an inward to an outward spiral in the phase space, or the other way around. A similar bifurcation can potentially occur on a branch, that is already periodic with frequency ω_1. In that case, a second frequency ω_2 is introduced in a secondary Hopf bifurcation on the periodic branch. The corresponding Floquet multipliers are two complex conjugated multipliers, that leave the unit circle, as seen in Fig. 2.2 a). They describe a perturbation that oscillates around the limit cycle, while the new frequency ω_2 can be derived from the Floquets imaginary part. The resulting trajectories live on a two-dimensional manifold, which is a torus. Thus, this type of bifurcation is referred to as a Torus bifurcation. Considering the frequency relation $\frac{\omega_1}{\omega_2}$ two different cases have to be distinguished: If $\frac{\omega_1}{\omega_2}$ is a rational number, the total trajectory is a closed orbit on the torus, which corresponds to a periodic solution. However, $\frac{\omega_1}{\omega_2}$ could be an irrational number. In that case, the trajectory on the torus will neither intersect itself, nor close [Str18]. It will also get arbitrarily close to any point on the torus surface.

2.2.3. Period-Doubling Bifurcation

Next, a stable branch of periodic solutions with a period of T shall be considered. Generally, a period-doubling (PD) bifurcation can occur in two cases. In a supercritical PD bifurcation, the stable branch of period T loses stability, and a new stable branch of solutions with period $2T$ emerges. In the subcritical case, however, an unstable branch of solutions with period $2T$ collides with the stable branch of period T, which loses stability again [TCF14]. A PD bifurcation occurs when a Floquet multiplier passes $\lambda = -1$ as shown in Fig. 2.2 c). Note that the Floquet multipliers describe how a perturbation on a periodic orbic has evolved after each round-trip, for a certain dimension. For $\lambda = 1$ the perturbation stays unchanged, which happens always trivially for perturbations tangential to the periodic orbit. However, $\lambda = -1$ means that a perturbation ϵ switches sign to $-\epsilon$ after each round-trip. If $\lambda < -1$ and is real, this perturbation with period $2T$ is growing, leading to a situation where the periodic solution itself becomes $2T$ periodic.

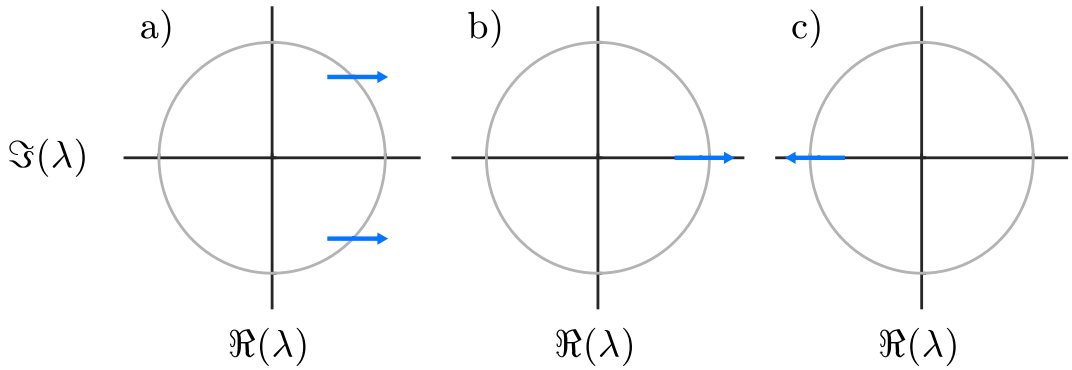

Figure 2.2: The behavior of Floquet multipliers at a torus a), a fold b), and a period-doubling (PD) bifurcation b) of periodic solutions . All three plots are centered around the origin, while the grey circle stands for the unit circle. The axis shows the real $\Re$ and imaginary $\Im$ part of the multipliers which leave the unit cycle, which corresponds to a transition from a stable, to an unstable solution.

2.3. Kerr Gires-Tournois Interferometer

This thesis will be an analysis of periodic solutions and bifurcations occuring in a vertical external cavity delayed Kerr Gires-Tournois interferometer (KGTI) which is shown in Fig. 2.3. The setup as shown in the figure differentiates between the microcavity field

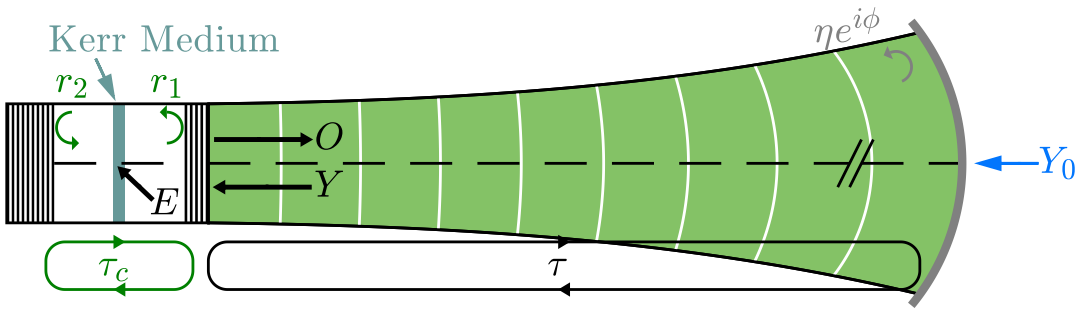

Figure 2.3: Sketch of the Kerr Gires-Tournois interferometer (KGTI) [SJG22]. It consists of a microcavity with round-trip time τ_c of the microcavity field E and an external cavity with round-trip time τ. The external cavity field $Y(t)$ consists of the external injection Y_0 and the reflected output $\eta e^{i\varphi} O(t-\tau)$. While $r_2 = 1$ closes the cavity at one side, $r_1 < 1$ which leads to a coupling of the cavities. Within the microcavity, a nonlinear Kerr medium is placed, which enables nonlinear effects such as pattern formation.

E, the external cavity field Y, the microcavity output O, and the external injection Y_0. The output O is reflected with $\eta e^{i\varphi}$, where the magnitude of η determines the strength of the feedback.
$\varphi = \phi + \omega\tau$ describes an accumulated effective phase considering the fact that in traveling around the external cavity the field with injection frequency ω gains an additional phase factor through the finite traveling time τ that is proportional to ω while the actual phase

factor gained from the feedback mirror is ϕ as indicated in Fig. 2.3. The microcavity input Y consists of the injection Y_0 as well as $\eta e^{i\varphi} O(t-\tau)$, which is the output from one round-trip before, that gained an additional prefactor when it was reflected. τ is the round-trip duration and thus the delay within the system equations. There is also the microcavity round-trip time τ_c, which will however not be used here since it is small compared to τ for a long external cavity.
In general, the fields E, Y and Y_0 denote the slowly varying envelope of electric fields that will perform the presented nonlinear dynamics such as formation of SWs or pulses. The fastly varying modes within the microcavity interact with the external feedback and the nonlinear medium leading to a slow modulation as the envelope fields E and Y vary in time and draw these temporal localized states (TLS) into the timetrace. Nevertheless, E and Y will be referred to as electric fields throughout this thesis.
The nonlinear Kerr medium will be placed within the microcavity described by a cubic nonlinearity. It is responsible for the possible occurrence of bistability. In Fig. 2.3, two reflection coefficients are shown as well. They describe the distributed Bragg mirrors at each end of the microcavity that are assumed to be lossless which is why the Stokes relations can be used to describe their properties within the derivation. Since there is a part of the external cavity field Y, that is reflected at the outside of the microcavity, with adequate scaling the output relation can be written down as

$$O = E - Y. \tag{2.18}$$

This will ultimately result in the external cavity field

$$Y(t) = \eta e^{i\varphi} \left[E(t-\tau) - Y(t-\tau)\right] + \sqrt{1-\eta^2} Y_0, \tag{2.19}$$

which is the description of the feedback loop. The external cavity field $Y(t)$ will then be injected into the microcavity and act as pumping for the field E. The previously derived full KGTI system is described by

$$\dot{E}(t) = \left[-1 - i\delta + i|E(t)|^2\right] E(t) + hY(t), \tag{2.20}$$

$$Y(t) = \eta e^{i\varphi} \left[E(t-\tau) - Y(t-\tau)\right] + \sqrt{1-\eta^2} Y_0, \tag{2.21}$$

where δ is the detuning between the injection frequency and the microcavity mode, h is a coupling strength between the cavities, η is the reflection coefficient of the feedback mirror with φ as an additional phase and Y_0 is the external injection strength. Throughout this thesis a perfectly reflecting mirror $|r_2| = 1$ will be chosen which leads to $h(r_1, 1) = 2$ corresponding to the so-called Gires–Tournois interferometer regime [GT64]. Finally one may notice that the equation for $Y(t)$ does not contain a time derivative. Hence it has to be seen as an algebraic constraint leading to a delay algebraic equation (DAE) system for the KGTI. The constraint (2.21) can be inserted into (2.20) resulting in a dependence of the current rate of change $\dot{E}(t)$ on $Y(t-\tau)$. Repeatedly inserting (2.21) shows how the present dynamics depend on all previous roundtrips $Y(t-n\tau)$ with $n \in \mathbb{N}$ through the algebraic constraint, especially in case of a strong feedback implied by a high reflection coefficient η.

2.4. System Derivation

Throughout the following section the KGTI system equations will be derived in detail from first principles, namely the Maxwell equations. The derivation is based on [Sch21] and [MB05], both discussing the derivation in a more general form. For simplification

nonmagnetic materials as well as no currents and free charges will be assumed. The corresponding Maxwell equations read:

$$\nabla \cdot \mathbf{D} = 0 \tag{2.22}$$
$$\nabla \cdot \mathbf{B} = 0 \tag{2.23}$$
$$\nabla \times \mathbf{E} = -\dot{\mathbf{B}} \tag{2.24}$$
$$\nabla \times \mathbf{H} = \dot{\mathbf{D}}, \tag{2.25}$$

with

$$\mathbf{D} = \epsilon_0(1+\chi)\mathbf{E} = \epsilon_0\mathbf{E} + \mathbf{P} \tag{2.26}$$
$$\mathbf{H} = \frac{1}{\mu_0}\mathbf{B}, \tag{2.27}$$

where χ is the electric susceptibility and P the polarization. The electric susceptibility is an important property for laser systems since it describes the ability of the material to polarize in response to an external electric field. It contains, e.g., the absorption, which is responsible for population inversion to surpass the lasing threshold. Thus, the susceptibility will be used to describe the interaction between the Kerr medium and the field within the microcavity. To do so the susceptibility is divided into a contribution of the nonlinearity χ_{nl} and a background part χ_b, leading to

$$\mathbf{D} = \epsilon_0(1+\chi_b)\mathbf{E} + \epsilon_0\chi_{\mathrm{nl}}\mathbf{E} = \epsilon_0\epsilon_r\mathbf{E} + \mathbf{P}_{\mathrm{nl}}. \tag{2.28}$$

To describe the propagation of electromagnetic waves the wave equation can be derived, which can be received by applying the curl operator onto the third Maxwell equation, followed by the vector identity

$$\nabla \times (\nabla \times \mathbf{A}) = \nabla(\nabla \cdot \mathbf{A}) - \nabla^2\mathbf{A}. \tag{2.29}$$

One can then identify the time derivative on the right-hand side, to get

$$\nabla(\nabla \cdot \mathbf{E}) - \nabla^2\mathbf{E} = -\mu_0\ddot{\mathbf{D}}. \tag{2.30}$$

Assuming $\nabla \cdot \mathbf{P}_{\mathrm{nl}} \ll 1$ results in $\nabla\mathbf{E} = 0$, due to the first Maxwell equation. Thereupon inserting the equation for the electric displacement into $\ddot{\mathbf{D}}$ yields

$$\nabla^2\mathbf{E} - \frac{n_b^2}{c^2}\ddot{\mathbf{E}} = +\mu_0\ddot{\mathbf{P}}_{\mathrm{nl}}, \tag{2.31}$$

which can be Fourier transformed to get rid of the time derivatives:

$$\left[\nabla^2 + \omega^2\frac{n_b^2}{c^2}\right]\mathbf{E} = -\omega^2\mu_0\mathbf{P}_{\mathrm{nl}} \tag{2.32}$$

2.4.1. Transversal Modes

This sections main goal is a scalar differential equation for the electric field. A few approximations have to be made in order to get there. Firstly, a radial symmetry will be assumed combined with a separation ansatz to solve the radial part separately. In this case, the remaining equation will describe the field amplitude along the longitudinal z-direction, plotted in Fig. 2.4. A transverse profile of the background refractive index

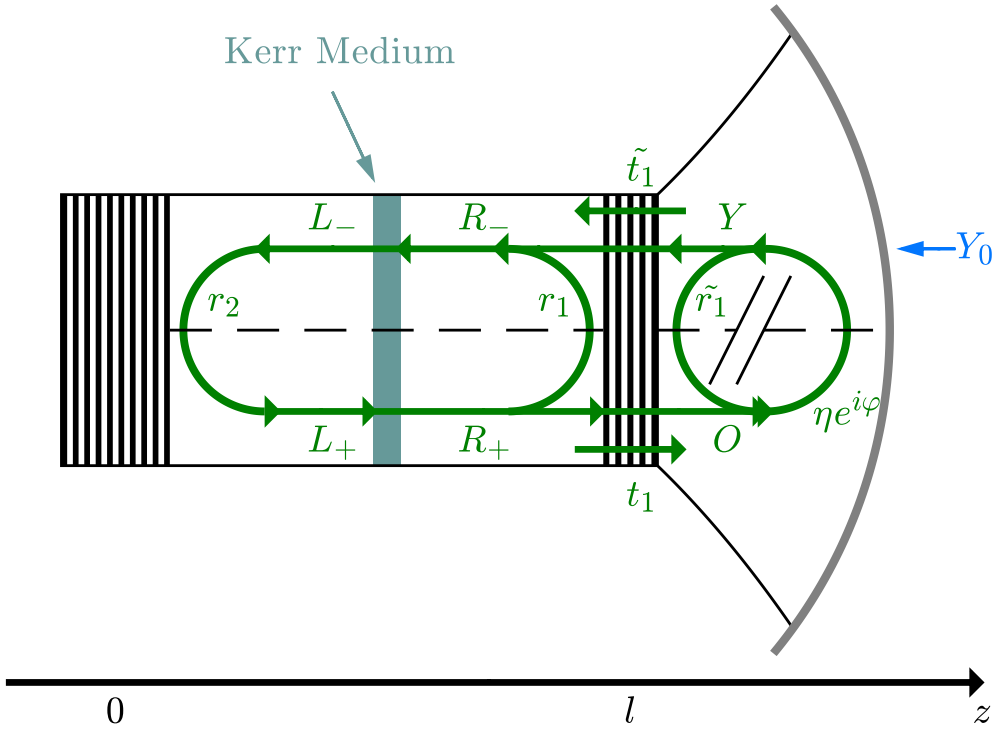

Figure 2.4: More detailed sketch of the fields within the KGTI . The microcavity field has been divided by traveling directions and sides of the Kerr medium. The mirrors are placed at $z = 0$ and $z = l$. This allows for good use of different boundary conditions throughout the derivation of the system equations.

$n_\perp(\mathbf{r}_\perp)$ will be introduced and a constant transverse mode $\phi(\mathbf{r}_\perp, \omega)$ is assumed to solve the eigenvalue equation

$$\left[\nabla_\perp^2 + \omega^2 \frac{n_\perp^2((\mathbf{r}_\perp, \omega))}{c^2}\right] \phi(\mathbf{r}_\perp, \omega) = \frac{\omega^2}{c^2} n_e^2 \phi(\mathbf{r}_\perp, \omega), \tag{2.33}$$

with the effective refractive index n_e. Since the field vectors are always orthogonal to the direction of propagation, it can be written with a transverse unit vector $\mathbf{e}_\perp$ as

$$\mathbf{E}(\mathbf{r}, \omega) = \phi(\mathbf{r}_\perp)\mathcal{E}_\perp(z, \omega)\mathbf{e}_\perp, \tag{2.34}$$

which is a separation ansatz with $\phi(\mathbf{r}_\perp)$ that contains the transverse profile, as well as $\mathcal{E}_\perp(z, \omega)$, which varies along the propagation direction. Now the transverse and longitudinal directions can be separated within the wave equation, to solve the transverse eigenvalue problem:

$$\left[\nabla^2 + \omega^2 \frac{n_b^2}{c^2}\right] \mathbf{E} = \left[\partial_z^2 + \nabla_\perp^2 + \omega^2 \frac{n_\perp^2}{c^2}\right] \phi(\mathbf{r}_\perp)\mathcal{E}_\perp(z, \omega)\mathbf{e}_\perp \tag{2.35}$$

$$= \left[\partial_z^2 + \omega^2 \frac{n_e}{c^2}\right] \phi(\mathbf{r}_\perp)\mathcal{E}_\perp(z, \omega)\mathbf{e}_\perp \tag{2.36}$$

$$= \phi(\mathbf{r}_\perp) \left[\partial_z^2 + \omega^2 \frac{n_e}{c^2}\right] \mathcal{E}_\perp(z, \omega)\mathbf{e}_\perp = -\omega^2 \mu_0 \mathbf{P}_{\mathrm{nl}} \tag{2.37}$$

In the next step, both sides are multiplied by the complex conjugated mode, to get the absolute value, followed by an integral over the plane spanned by the transverse

dimensions which is

$$\int_{-\infty}^{\infty}\int_{-\infty}^{\infty}|\phi(\mathbf{r}_\perp)|^2 d^2r_\perp \left[\partial_z^2+\omega^2\frac{n_e}{c^2}\right]\mathcal{E}_\perp(z,\omega)\mathbf{e}_\perp = -\omega^2\mu_0\int_{-\infty}^{\infty}\int_{-\infty}^{\infty}\phi^*(\mathbf{r}_\perp)\mathbf{P}_{\mathrm{nl}}(\mathbf{r})d^2r_\perp. \tag{2.38}$$

The polarization is the product of electric field and susceptibility. Although a separation for the electric field is known, no assumptions regarding the susceptibility have been made so far. Thus, the polarization cannot be fully separated, leading to

$$\mathbf{P}_{\mathrm{nl}}(\mathbf{r}) = \epsilon_0\chi_{\mathrm{nl}}(\mathbf{r})\phi(\mathbf{r}_\perp)\mathcal{E}_\perp(z,\omega)\mathbf{e}_\perp, \tag{2.39}$$

which turns the right-hand side into an expectation value of the nonlinear susceptibility. The right-hand side (rhs.) can be written as

$$\text{rhs.} = -\omega^2\frac{1}{c^2}\int_{-\infty}^{\infty}\int_{-\infty}^{\infty}|\phi(\mathbf{r}_\perp)|^2\chi_{\mathrm{nl}}(\mathbf{r})d^2r_\perp\mathcal{E}_\perp(z,\omega)\mathbf{e}_\perp, \tag{2.40}$$

where the relation $\epsilon_0\mu_0 = \frac{1}{c^2}$ has been used. Without limiting generality, the nonlinear Kerr medium will be assumed to be centered around $\mathbf{r}_\perp = 0$. Also the transverse profile of the susceptibility $\chi_{\mathrm{nl}}(\mathbf{r}_\perp, z)$ should be approximately constant within the active region, but zero everywhere else. This simply assumes the active material to be homogeneous without any directional dependencies. This results in $\chi_{\mathrm{nl}}(\mathbf{r}_\perp, z) = \chi_{\mathrm{nl}}(0, z)$, which leads to a simplification of the integral to

$$\text{rhs.} = -\omega^2\frac{1}{c^2}\int\int_{\mathrm{AR}}|\phi(\mathbf{r}_\perp)|^2 d^2r_\perp\chi_{\mathrm{nl}}(0,z)\mathcal{E}_\perp(z,\omega)\mathbf{e}_\perp. \tag{2.41}$$

The remaining integrals can be summarized within the so-called transverse confinement factor [Sch21]:

$$\Gamma_\perp = \frac{\int\int_{\mathrm{AR}}|\phi(\mathbf{r}_\perp)|^2 d^2r_\perp}{\int_{-\infty}^{\infty}\int_{-\infty}^{\infty}|\phi(\mathbf{r}_\perp)|^2 d^2r_\perp} \tag{2.42}$$

Due to all dependencies on the components $\mathbf{r}_\perp$ being within $\Gamma_\perp$ where they vanish due to integration, a rotational symmetry around the z-axis is found. The remaining equation

$$\left[\frac{\partial^2}{\partial z^2}+\omega^2\frac{n_e^2}{c^2}\right]\mathcal{E}_\perp(z) = -\frac{\omega^2}{c^2}\Gamma_\perp\chi_{\mathrm{nl}}(0,z)\mathcal{E}_\perp(z) \tag{2.43}$$

$$= -\omega^2\mu_0\Gamma_\perp\mathcal{P}_\perp \tag{2.44}$$

describes the modulation of the electric field along the longitudinal axis, as demanded.

2.4.2. Microcavity with Thin Nonlinear Region

Now a microcavity with injection and feedback loop will be considered, as it is the case for the KGTI. One can start with the final equation from last section, however $n_e = n$ the removal of all $\perp$ will be used for a simpler notation, leading to

$$\left[\frac{\partial^2}{\partial z^2}+\omega^2\frac{n^2}{c^2}\right]\mathcal{E}(\omega,z) = -\omega^2\mu_0\Gamma\chi_{\mathrm{nl}}(z,\omega)\mathcal{E}(\omega,z). \tag{2.45}$$

If the nonlinear region with width W is considered thin compared to the wavelength and located at $z = z_0$, it can be described by a Dirac's delta. This leads to the equation

$$\left[\frac{\partial^2}{\partial z^2} + \omega^2 \frac{n^2}{c^2}\right] \mathcal{E}(\omega, z) = -\omega^2 \mu_0 \chi(\omega) \delta(z - z_0) \mathcal{E}(\omega, z), \tag{2.46}$$

where $\chi(\omega) = \Gamma W \chi_{nl}(\omega)$ describes the interaction between the mode ω and the nonlinear medium. The form of $\chi(\omega)$ can be derived from material specific models. To get rid of the Dirac's delta, one can integrate over a small region around z_0, leading to

$$\frac{\partial}{\partial z} \mathcal{E}(\omega, z)|_{z_0-\epsilon}^{z_0+\epsilon} + \omega^2 \frac{n^2}{c^2} \int_{z_0-\epsilon}^{z_0+\epsilon} \mathcal{E}(\omega, z) = -\omega^2 \mu_0 \Gamma \chi(\omega) \mathcal{E}(\omega, z_0). \tag{2.47}$$

The remaining integral can be investigated by splitting the electromagnetic field as shown in Fig. 2.4. A mode propagating along the z-axis generally consists of a part propagating in positive $(+)$, as well as in negative $(-)$ direction. For a microcavity of length l with a nonlinear medium placed at $z = z_0$

$$\mathcal{E}(\omega, z) = \begin{cases} L(\omega, z) = L_+ e^{iqz} + L_- e^{-iqz} & \forall 0 < z < z_0 \\ R(\omega, z) = R_+ e^{iqz} + R_- e^{-iqz} & \forall z_0 < z < l \end{cases} \tag{2.48}$$

can be found, where the wave vector $q = \frac{\omega n}{c}$ is assumed to be the same on both sides of the Kerr medium. Rewriting the field allows to simplify Eq. (2.47) to

$$\frac{\partial}{\partial z} \mathcal{R}(\omega, z)|_{z_0+\epsilon} - \frac{\partial}{\partial z} \mathcal{L}(\omega, z)|_{z_0-\epsilon} + \omega^2 \frac{n^2}{c^2} \int_{z_0-\epsilon}^{z_0+\epsilon} \mathcal{E}(\omega, z) = -\omega^2 \mu_0 \chi(\omega) \mathcal{E}(\omega, z_0), \tag{2.49}$$

which introduces the first boundary conditions. Looking at Eq. (2.49) with $\epsilon \to 0$ leads to

$$L(\omega, z_0) = R(\omega, z_0) = \mathcal{E}(\omega, z_0), \tag{2.50}$$

forcing the field to be continuous at the nonlinear medium, but not its derivative due to

$$\frac{\partial}{\partial z} \mathcal{R}(\omega, z)|_{z_0} - \frac{\partial}{\partial z} \mathcal{L}(\omega, z)|_{z_0} = -\omega^2 \mu_0 \chi(\omega) \mathcal{E}(\omega, z_0). \tag{2.51}$$

2.4.3. Injected Micro Cavity with Thin Nonlinear Medium

Further boundary conditions can be found by considering the KGTI setup explicitly as in Fig. 2.4. Firstly, two distributed Bragg mirrors reflectivities r_2 and r_1 are considered. $|r_2| = 1$ is chosen, to close one side of the microcavity. With the reflection coefficients r_i and the transmission coefficients t_i, one can write the output relation as

$$O = t_1 R_+ e^{iql} + \tilde{r}_1 Y, \tag{2.52}$$

while the microcavity input can be written as

$$R_- e^{-iql} = \tilde{t}_1 Y + r_1 R_+ e^{iql}. \tag{2.53}$$

The reflection at the mirror located at $z = 0$ yields

$$r_2 L_- = L_+. \tag{2.54}$$

The continuity condition Eq. (2.50) allows to write all fields as functions of the electric field $\mathcal{E}(\omega, z_0)$ at the nonlinear medium with an additional phase considering the distance to the medium. $\mathcal{E}(\omega, z_0) = \mathcal{E}$ will be introduced for notation purposes. The field at the nonlinear medium is then

$$\mathcal{E} = L_+ e^{iqz_0} + L_- e^{-iqz_0}. \tag{2.55}$$

Once can now replace either L_+ or L_- to find

$$\mathcal{E} = r_2 L_- e^{iqz_0} + L_- e^{-iqz_0} \tag{2.56}$$

$$\mathcal{E} = L_+ e^{iqz_0} + \frac{1}{r_2} L_+ e^{-iqz_0}. \tag{2.57}$$

For the other two fields

$$\mathcal{E} = R_+ e^{iqz_0} + (\tilde{t_1} Y + r_1 R_+ e^{iql}) e^{iql} e^{-iqz_0}, \tag{2.58}$$

as well as

$$\mathcal{E} = \frac{1}{r_1}(R_- e^{-iql} - \tilde{t_1} Y) e^{-iql} e^{iqz_0} + R_- e^{-iqz_0}, \tag{2.59}$$

is found. After rewriting, the equations for the four partial fields as functions of $\mathcal{E}(\omega, z_0)$ are

$$L_- = \frac{e^{iqz_0}\mathcal{E}}{1 + r_2 e^{2iqz_0}} \tag{2.60}$$

$$L_+ = \frac{r_2 e^{-iqz_0}\mathcal{E}}{e^{-2iqz_0} + r_2} \tag{2.61}$$

$$R_- = e^{iql} \frac{r_1 \mathcal{E} e^{iq(l-z_0)} + t_1 Y}{1 + r_1 e^{2iq(l-z_0)}} \tag{2.62}$$

$$R_+ = e^{-iql} \frac{\mathcal{E} e^{-iq(l-z_0)} - \tilde{t}_1 Y}{r_1 + e^{-2iq(l-z_0)}}. \tag{2.63}$$

These expressions can now be inserted in Eq.2.51 leading to

$$-\omega^2 \mu_0 \chi(\omega) \mathcal{E} = \frac{\partial}{\partial z} \mathcal{R}(\omega, z)|_{z_0} - \frac{\partial}{\partial z} \mathcal{L}(\omega, z)|_{z_0} \tag{2.64}$$

$$= iq \left(R_+ e^{iqz_0} - R_- e^{-iqz_0} - L_+ e^{iqz_0} + L_- e^{-iqz_0} \right) \tag{2.65}$$

$$= iq \left(\frac{1 - r_1 e^{2iq(l-z_0)}}{1 + r_1 e^{2iq(l-z_0)}} \mathcal{E} + \frac{1 - r_2 e^{2iqz_0}}{1 + r_2 e^{2iqz_0}} \mathcal{E} - \frac{2\tilde{t_1} e^{iq(l-z_0)}}{1 + r_1 e^{2iq(l-z_0)}} Y \right) \tag{2.66}$$

which has several consequences. Firstly, it was possible to remove any integrals and derivatives, secondly the equation does not depend on the position z. This is possible due to the assumption that the field does not interact with the medium between the mirrors and nonlinear medium. By including all interactions at mirrors and nonlinear medium, the spatially extended field is fully described by the field value at the nonlinear medium $\mathcal{E}(\omega, z_0)$ and the injection Y. However, the equation can be further simplified by multiplying it by the confinement factor

$$\Gamma(q) = (1 + r_1 e^{2iq(l-z_0)})(1 + r_2 e^{2iqz_0}), \tag{2.67}$$

which is the product of the two denominators. This leads to

$$-\omega^2\mu_0\Gamma(q)\chi(\omega)\mathcal{E} = iq\Big(\left(1-r_1e^{2iq(l-z_0)}\right)\left(1+r_2e^{2iqz_0}\right)\mathcal{E}+\left(1+r_1e^{2iq(l-z_0)}\right)\left(1-r_2e^{2iqz_0}\right)\mathcal{E} - \left(1+r_2e^{2iqz_0}\right)2\tilde{t_1}e^{iq(l-z_0)}Y\Big). \tag{2.68}$$

The introduction of

$$F_1(q) = 1 - r_1r_2e^{2iql} \tag{2.69}$$

$$F_2(q) = \left(1+r_2e^{2iqz_0}\right)\tilde{t_1}e^{iq(l-z_0)}, \tag{2.70}$$

yields the compact equation

$$F_1(q)\mathcal{E} - F_2(q)Y = -\omega^2\frac{\mu_0}{2iq}\Gamma(q)\chi(\omega)\mathcal{E} \tag{2.71}$$

$$= i\omega\frac{\mu_0 c}{2n}\Gamma(q)\chi(\omega)\mathcal{E}, \tag{2.72}$$

where the definition of $\omega(q)$ has been used as well. For a further simplification the entire frequency dependence of the reflection coefficients can be assumed to be contained in the phase, by writing $r_i(\omega) = \rho_i e^{i\phi_i(\omega)}$. The newly introduced coefficients are

$$\Gamma(q) = (1+\rho_1e^{2iq(l-z_0)+i\phi_1})(1+\rho_2e^{2iqz_0+i\phi_2}), \tag{2.73}$$

$$F_1(q) = 1-\rho_1\rho_2e^{2iql+i\phi_1+i\phi_2}, \tag{2.74}$$

$$F_2(q) = \left(1+\rho_2e^{2iqz_0+i\phi_2}\right)\tilde{t_1}e^{iq(l-z_0)}. \tag{2.75}$$

2.4.4. Expanding around a Cavity Mode

In the next step injection and emission are assumed to be close to a cavity wave frequency $\omega_0 = \omega(q_0)$. The cavity wave frequencies are resonant within the microcavity, so their frequency has to fit in a round-trip length which consists of twice the cavity length l including the two phase jumps ϕ_1 and ϕ_2. Thus a cavity frequency fulfills

$$2q_0l + \phi_1(\omega_0) + \phi_2(\omega_0) = 2\pi m, \;\; m \in \mathbb{N} \tag{2.76}$$

which is a resonance condition minimizing F_1 for a given ρ_1 and ρ_2. The same way the nonlinear medium should be placed appropriately, leading to the two conditions

$$2q_0(l-z_0) + \phi_1(\omega_0) = 2\pi n_1 \tag{2.77}$$

$$2q_0z_0 + \phi_2(\omega_0) = 2\pi n_2, \tag{2.78}$$

which corresponds to a minimization of the confinement factor. The cavity wave frequency minimizes F_1 by fulfilling

$$\rho_1\rho_2e^{2iq_0l+i\phi_1+i\phi_2} = \rho_1\rho_2e^{2i\frac{\omega_0 n}{c}l+i\phi_1+i\phi_2} \approx 1. \tag{2.79}$$

Considering frequencies $\omega = \omega_0 + \delta\omega$ close to a cavity mode with a slight deviation $\delta\omega$ enables an expansion of F_1 around the cavity mode

$$F_1(\omega) = F_1(\omega_0) + \frac{\partial F_1}{\partial\omega}|_{\omega=\omega_0}\delta\omega + \mathcal{O}(\delta\omega^2) \tag{2.80}$$

$$= 1-\rho_1\rho_2 - i\left(2\frac{n}{c}l + \frac{\partial\phi_1}{\partial\omega}|_{\omega=\omega_0} + \frac{\partial\phi_2}{\partial\omega}|_{\omega=\omega_0}\right)\rho_1\rho_2\delta\omega + \mathcal{O}(\delta\omega^2) \tag{2.81}$$

$$= 1-\rho_1\rho_2 - i\rho_1\rho_2\frac{n}{c}L\delta\omega + \mathcal{O}(\delta\omega^2), \tag{2.82}$$

which is cut after first order. L is called the effective round-trip length since it contains $2l$ with a linearized correction due to the phase jumps at the mirrors. The resulting terms can be inserted into Eq. (2.72) which yields

$$\left(1-\rho_1\rho_2-i\rho_1\rho_2\frac{n}{c}L\delta\omega\right)\mathcal{E}=-\left(1-\rho_1\rho_2\right)\mathcal{E}+i\omega\frac{\mu_0 c}{2n}\Gamma(q_0)\chi(\omega_0)\mathcal{E}+F_2(q_0)Y. \tag{2.83}$$

This corresponds to

$$-i\rho_1\rho_2\frac{n}{c}L\delta\omega\mathcal{E}=i\omega_0\frac{\mu_0 c}{2n}(1+\rho_1)(1+\rho_2)\chi(\omega_0)\mathcal{E}+(1+\rho_2)\,\tilde{t}_1 e^{iq_0(l-z_0)}Y. \tag{2.84}$$

$\frac{n}{c}L=\tau_c$ will be the microcavity round-trip time, which is already known from Fig. 2.3. The frequency deviation $\delta\omega$ consists of a small detuning Δ, the deviation between injection frequency and cavity frequency, as well as remaining frequency variations $\Delta\omega$. Latter turn into a time derivative operator $-i\Delta\omega\rightarrow\partial_t$ after an inverse Fourier transform, yielding

$$\rho_1\rho_2\tau_c\left(\frac{\partial}{\partial_t}-i\Delta\right)\mathcal{E}(t)=i\omega_0\frac{\mu_0 c}{2n}(1+\rho_1)(1+\rho_2)\chi(\omega_0)\mathcal{E}(t)+(1+\rho_2)\,\tilde{t}_1 e^{iq_0(l-z_0)}Y(t). \tag{2.85}$$

2.4.5. Rescaling

This equation is already very close to the KGTI system equation. This will become more apparent after some rescaling. After deviding by $1-\rho_1\rho_2$ one can introduce

$$\kappa=\frac{1-\rho_1\rho_2}{\rho_1\rho_2}\tau_c^{-1} \tag{2.86}$$

$$\delta=\frac{-\Delta}{\kappa} \tag{2.87}$$

$$b=\frac{\omega_0}{2nc}\frac{(1+\rho_1)(1+\rho_2)}{1-\rho_1\rho_2} \tag{2.88}$$

$$\tilde{h}=t_1' e^{i(\pi n_1-\frac{1}{2}\phi_1(\omega_0))}\frac{1+\rho_2}{1-\rho_1\rho_2}. \tag{2.89}$$

κ^{-1} is the photon lifetime, approaching infinity for perfect reflectivities ρ_1 and ρ_2. δ is the scaled detuning that is already known from (2.20), while $\tilde{h}$ is the injection coupling factor where Eq. (2.77) has been used. b, finally, is the polarized prefactor, which will be pulled into the susceptibility as $\frac{b}{\epsilon_0}\chi(\omega_0)\rightarrow\chi$. This leads to

$$\frac{1}{\kappa}\dot{\mathcal{E}}(t)=-i\delta\mathcal{E}(t)+i\chi\mathcal{E}(t)+\tilde{h}Y(t). \tag{2.90}$$

In a last step the field $\mathcal{E}$ will be scaled to the same order of magnitude as Y. Therefor one can start with the output relation Eq. (2.52) and insert the equation for R_+ Eq. (2.63):

$$O=t_1R_+e^{iql}+\tilde{r}_1Y \tag{2.91}$$

$$=t_1\frac{\mathcal{E}e^{-iq(l-z_0)}-\tilde{t}_1Y}{r_1+e^{-2iq(l-z_0)}}+r_1Y \tag{2.92}$$

$$=\alpha\mathcal{E}+\beta Y \tag{2.93}$$

Assuming the Stokes relations $t't = 1 + r'r$ and $r = -r'$ to hold for approximately lossless distributed bragg mirrors and using $r_1 = \rho_1 e^{i\phi_1}$ as well as the conditions derived for resonant frequencies, yields

$$\begin{aligned}
\beta &= \tilde{r}_1 - \frac{t_1 \tilde{t_1}}{r_1 + e^{-2iq(l-z_0)}} && (2.94)\\
&= -r_1 - \frac{(1 + r_1\tilde{r_1}}{1 + r_1 e^{2iq(l-z_0)}} e^{2iq(l-z_0)} && (2.95)\\
&= -r_1 - \frac{1 - r_1^2}{1 + \rho_1} e^{-i\phi_1} && (2.96)\\
&= \frac{-r_1(1 + \rho_1}{1 + \rho_1} - \frac{1 - r_1^2}{1 + \rho_1} e^{-i\phi_1} && (2.97)\\
&= \frac{-\rho_1 e^{i\phi_1} - \rho_1^2 e^{i\phi_1} + \rho_1^2 e^{i\phi_1} - e^{-i\phi_1}}{1 + \rho_1} && (2.98)\\
&= -\frac{e^{-i\phi_1} + \rho_1 e^{i\phi_1}}{1 + \rho_1}. && (2.99)
\end{aligned}$$

While vacuum or a refractive index of approximately one is assumed at the outside of the microcavity, the materials within the microcavity have a substantially larger refractive index. Thus r_1 describing the reflection at the microcavity inside is positive and $\tilde{r}_1$ is negative Together with the lossless distributed Bragg mirror one gets $\phi_1 = 0$. This corresponds to a π-phase shift occurring by reflection at the cavity outside [Sch+19b]. The prefactor β then becomes $\beta = -1$, while α reduces to

$$\begin{aligned}
\alpha &= \frac{t_1 e^{iq(l-z_0)}}{1 + r_1 e^{2iq(l-z_0)}} && (2.100)\\
&= \frac{t_1 e^{i(\pi n_1 - \frac{\phi_1}{2}}}{1 + \rho_1} && (2.101)\\
&= \frac{t_1 e^{i(\pi n_1)}}{1 + \rho_1} && (2.102)\\
&= \frac{(-1)^{n_1} t_1}{1 + \rho_1}. && (2.103)
\end{aligned}$$

Eventually $E(t) = \alpha\mathcal{E}(t)$ as well as $h = \alpha\tilde{h}$ are introduced as new scaling, where h is

$$\begin{aligned}
h &= \frac{t_1 t_1'}{1 + \rho_1} \frac{1 + \rho_2}{1 - \rho_1\rho_2} && (2.104)\\
&= \frac{(1 - \rho_1)(1 + \rho_2)}{1 - \rho_1\rho_2}. && (2.105)
\end{aligned}$$

This is the already known coupling factor, which becomes $h = 2$ for $\rho_2 = 1$ corresponding to the before mentioned perfect mirror at one side of the microcavity. Using these two scalings leads to the final equation system for the injected microcavity with a thin nonlinear region

$$\begin{aligned}
\kappa^{-1}\dot{E} &= [-1 - i\delta + i\chi]E + hY, && (2.106)\\
O &= E - Y. && (2.107)
\end{aligned}$$

2.4.6. Kerr Gires-Tournois Interferometer System Equations

From here the KGTI system can be recovered easily. The time delay for the KGTI system enters in the output relation, which describes the feedback loop through the external cavity. The input consists of two contributions. The output gets reinjected after one round-trip. Upon being reflected at the feedback mirror it will get damped by η and gain a potential phase φ. The other contribution is the external injection beam Y_0, which also has to pass the feedback mirror. The resulting prefactor $\sqrt{1-\eta^2}$ can be derived from the stokes relations as well. So the microcavity injection can be written as

$$Y = \eta e^{i\varphi} O + \sqrt{1-\eta^2} Y_0. \tag{2.108}$$

In the case of a long external cavity, it becomes of increasing relevance, that the input $Y(t)$ depends on the output $O(t-\tau)$, where τ is the external cavity round-trip time. As a result an equation for the injection is found with

$$Y(t) = \eta e^{i\varphi} \left[E(t-\tau) - Y(t-\tau)\right] + \sqrt{1-\eta^2} Y_0. \tag{2.109}$$

Finally, the nonlinearity χ has to be specified. For the standard KGTI a nonlinear Kerr medium is used. The Kerr effect is a nonlinear optical effect where the slowly varying envelope field experiences a change in refractive index that is proportional to its intensity and hence described by $\chi = |E|^2$. This leads to the third order nonlinearity, that has been described before. For the KGTI with active medium that will be investigated in later section, a quantum well will be used as nonlinearity, which is described by a quantum well susceptibility [Bal98], which reads

$$\chi(u, D) = \frac{1}{\pi} \left[\ln(u + i - b) - 2\ln(u + i - D) + \ln(u + i) - \ln(b)\right], \tag{2.110}$$

where u is a rescaled injected frequency. The dynamics of the newly introduced carrier density D are governed by a new differential equation

$$\dot{D}(t) = \gamma_{||} \left[-D(t) + \Im(\chi)|E|^2\right]. \tag{2.111}$$

2.5. Space-time Representation in the Long-delay Limit

A useful approach for the description of dynamics in systems with a delay that is long compared to the other time scales is the folding of time in multiples of the delay. This leads to a two-dimensional or quasi-space-time representation, since every point in time can be described as $t = \theta\tau + \sigma$, where τ is the delay, $\theta \in \mathbb{N}$ and σ is the remainder [Are+92][Gia+12][MG20]. Here, σ can be seen as the position within the quasi-spatial dimension describing dynamics within a period of the system. There, θ is the new time scale describing the evolution of the system over many roundtrips. The long delay leads to dynamics that evolve on separate time scales, which is important to make this transformation applicable since well-separated time scales can be treated as independent variables [MG20]. This representation facilitates to observe periodic solutions such as pulses transforming or moving relative to the delay. Thus, purely temporal behavior on different time scales becomes more transparent, when viewed in a space-time representation and can be compared to one-dimensional spatially extended systems, showing well-known phenomenons such as coarsening, drift, among others [YG17]. Here, the periodic solutions in the purely temporal dynamics become steady states in spatially extended systems and the corresponding bifurcations of limit cycles can be identified with bifurcations of steady states. An example for coarsening in a space-time representation

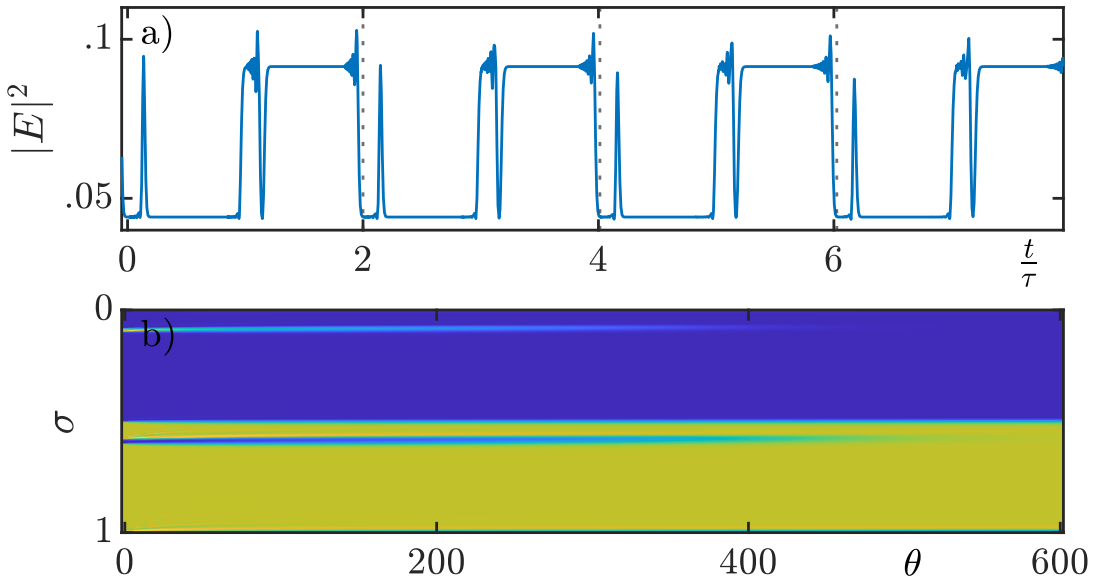

Figure 2.5: a) Extract of a timetrace showing four repetitions of a periodic solution with a period of approximately 2τ. The dotted vertical lines indicate the cuts that led to the space-time representation in b). b) Space-time representation allowing for a compact analysis of a long time-trace. The scale σ describes dynamics within a round-trip of length 2τ while θ counts round-trips. The space-time representation allows to observe the thin pulse decaying towards full coarsening.

is shown in Fig. 2.5. Throughout this thesis, the systems will be treated mainly in the long-delay limit, which makes this description well applicable. The separated time scales in a long-delay limit also allow for other methods such as multiple-time-scale analysis, which will find applications in later chapters. Note, that systems with several delays can be compared to two-dimensional spatially extended systems in the same way, if both delays are large and separated, such as $1 \ll \tau_1 \ll \tau_2$. In such a case, the purely temporal dynamics of a multiple delay system can be identified with well-known spatio-temporal dynamics in a two-dimensional spatially extended system [YG14].
Treating time-delayed systems in long-delay limit has an additional advantage. In this limit the eigenvalue spectrum obtained by linear stability analysis will separate into a discrete and a pseudo-continuous part [Sch21]. While the discrete part has an equivalent for systems without a delay, the pseudo-continuous curve consists of an infinite number of eigenvalues confined to a distance on the curve proportional $\frac{2\pi}{\tau}$ [WY06] that converges to zero in long-delay limit. The resulting pseudo-continuous-curves can behave analogously to the eigenvalue spectra in spatially extended systems, showing typical bifurcations for spatially extended systems such as Turing bifurcations. The corresponding behavior such as short-wavelength pattern formation is then observed in the quasi-space-time representation.
Furthermore, the quasi-continuous eigenvalues can be approximated as

$$\lambda = \frac{\gamma(\omega)}{\tau} + i\omega + \mathcal{O}\left(\frac{1}{\tau^2}\right), \tag{2.112}$$

with $\gamma(\omega)$ defining a curve where the eigenvalues live on [YG17]. The transcendental equation obtained in a linear stability analysis can be simplified and approximately solved using this ansatz [Wol+10], which enables a useful approach for the treatment of time-delayed systems in long-delay limit. Finally, this eigenvalue discussion can be utilized to explain the transformation from Eq. (1.2) into Eq. (1.1) for short delays. Since the additional eigenvalues in the delay case have a distance proportional to $\frac{2\pi}{\tau}$ they diverge to describe infinitely high frequencies when the delay strives towards zero. On this occasion they move along the curve and their real part switches from positive to negative. In the limit of a vanishing delay these additional eigenvalues gather at a real part of $-\infty$ and only the eigenvalues from the equation without delay remain relevant.

2.6. Square-waves in Time-delayed Systems

Within the last chapter, the strong analogy between systems with long delay and spatially extended systems has been outlined. Nevertheless, this thesis will focus on structures, which seem to be less typical for spatially extended systems, which are square-waves (SWs).

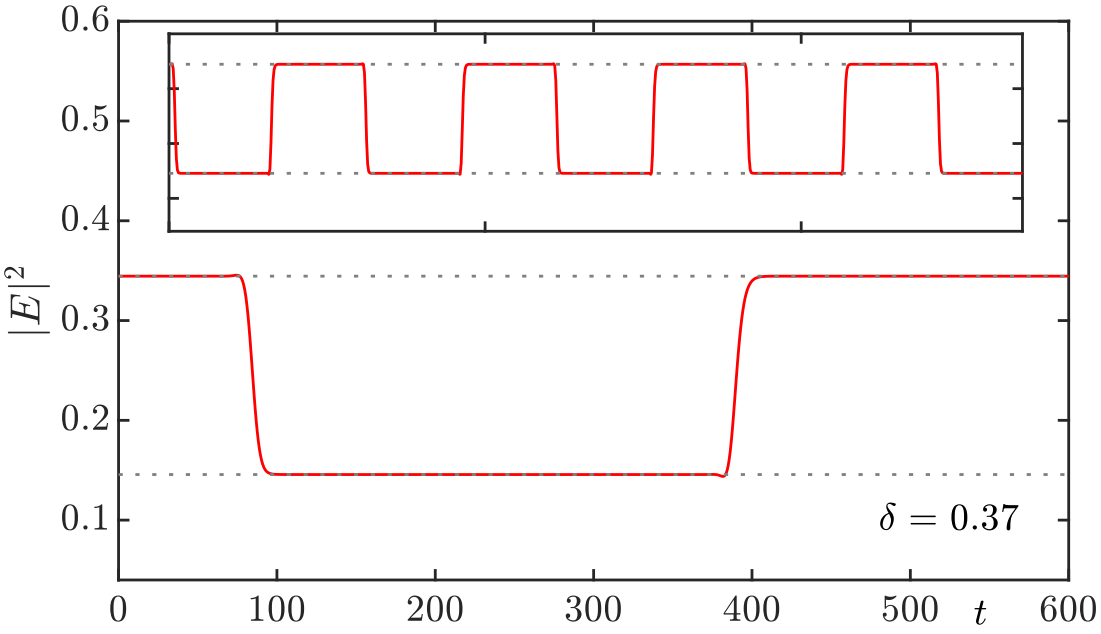

Figure 2.6: Exemplary square-wave (SW) solution consisting of two flat plateaus each with a length of approximately 1τ, where τ is the delay time. Hence, the solution is approximately 2τ-periodic. This is already a solution for the Kerr Gires-Tournois interferometer, which will be introduced in detail later this section.

Coarsening dynamics in bistable systems with long delay have been mentioned before, where fronts propagate and ultimately annihilate, similar to the behavior that can be observed in spatially extended systems [Gia+12]. However, time-delayed systems are also able to prevent coarsening via an arrest of domain walls through the ability of these systems, to generate antiperiodic output, i.e., temporal traces getting inverted after each

time delay τ [JAH15]. The concept of antiperiodicity can be understood by looking at the equation

$$x(t) = e^{i\varphi}x(t-\tau), \tag{2.113}$$

where only the cases $\varphi = 0$ and $\varphi = \pi$ will be of interest here. The first case describes a τ-periodic solution. Any initial condition of length τ will be repeated periodically. In the case $\varphi = \pi$, however, the solution will be inverted after each round-trip. An example for this type of solutions are SWs consisting of two plateaus with sharp transitions, and 50% duty cycle as shown in Fig. 2.6. The sharp transitions after each round-trip are due to the antiresonant feedback resulting from the phase $\varphi = \pi$. This also explains, why SWs are typically observed, to have a period of approximately 2τ [Niz04][Mas+12], although they have been observed to coexist with harmonic SWs of smaller periods $\frac{2\tau}{2n+1}$ [Fri+14]. It is easy to understand, how such a solution can appear in delay differential equations within the long-delay limit. To do so, one can investigate the equation

$$\epsilon\dot{x} = -x + f(\lambda, x(t-1)), \tag{2.114}$$

with a dimensionless time that has been transformed with respect to the delay τ as $\frac{t}{\tau} \to t$ and the smallness parameter $\epsilon = \frac{1}{\tau}$. This equation is investigated for $f = e^{i\varphi}x(t-1)$ in the long-delay limit, which means $\epsilon \to 0$. This reproduces the equation from before and thus, the observation of SWs for $\varphi = \pi$. The importance of a long delay for the occurrence of SWs can be understood by solving this equation for $\dot{x}$, after inserting $\varphi = \pi$

$$\dot{x} = -\tau\big(x(t) + x(t-1)\big). \tag{2.115}$$

This is a normal decay equation, so the system will try to minimize the right-hand side, which is the case for $x(t) = -x(t-1)$. In the long-delay limit this will happen almost instantaneously leading to sharp transition layers and thus, the possibility of SWs. SWs have been observed and analyzed on several occasions. They have occurred especially in several semiconductor laser systems, such as vertical-cavity surface-emitting lasers (VCSELS) [Mul+07][Mar+13], edge-emitting lasers [Gav+06][Fri+14], semiconductor ring lasers [Li+16][Mas+12], and quantum dot lasers[Dil+19]. From a theoretical perspective, Eq. (2.114) has been analyzed in detail by Mallet-Paret et al. [MN98]. T. Erneux describes the arising of SWs in a supercritical Hopf-bifurcation for the Ikeda DDE [Ern08], which is a special case of Eq. (2.114). Here the periodic solution arises, again for small ϵ, as a harmonic oscillation rapidly transforming into a SW with increasingly sharp corners. The case of small ϵ allows to treat the equation as a map. Also, it corresponds to a long delay, where the map discretizes the time in terms of delays.

3. Numerical Methods

3.1. Numerical Integration of Delay Differential Equations

In nonlinear physics, most problems are described by dynamical systems. Although some of these can be solved analytical, for the vast majority even the attempt poses a big problem. The term nonlinear itself hints at the occurrence of nonlinear terms, which breaks the principle of superposition that can often be used to find analytical solutions of a linear differential equation. It is because of this, but as well for the time saving, that numerical methods are a good way, to tackle problems in nonlinear equations efficiently. Hence, it is important to consider the necessary discretization in time and all spatial variables. A very simple algorithm to calculate the temporal evolution of a system is the so-called Euler's method [Str18]. It can be applied to a one-dimensional DDE in its general form

$$\dot{x}(t) = f(x(t), x(t-\tau_1), ..., x(t-\tau_N), t), \tag{3.1}$$

with several delays $\tau_1, ...\tau_N$. The time step h is chosen in a way that $\frac{\tau_i}{h} = m_i \in \mathrm{N}$ for all delays τ_i. In that case the initial condition consists of a discrete function $x_0(s)$ over $s \in \{-\max_i(\tau_i), -\max_i(\tau_i)+h, ..., -h, 0\}$. For a shorter notation the labels $t = hn = t_n$ and $x(t_n) = x_n$ are introduced. Euler's method assumes that between each point in the discrete time the derivative is constant allowing to approximate a new point simply by calculating the derivative from the system's right-hand side, and multiplying it by h. This poses a simple linear equation:

$$x_{n+1} = x_n + h \cdot f(x_n, x_{n-m_1}, ..., x_{n-m_N}, t_n) \tag{3.2}$$

The points x_{n-m_i} are known from the initial condition, or for larger times from the past of the system. Although its simplicity is an advantage, the Euler's method often fails due to the fact, that a linear approximation of the derivative over an interval might be not accurate enough, especially in nonlinear equations. The Euler method can be compared to an expansion, which has been truncated after the linear order. The global truncation error over the whole integration interval is $\mathcal{O}(h)$, while the local truncation error is $\mathcal{O}(h^2)$ [Gur18].
Comparing the different numerical methods efficiency is a very important factor. Within the framework of Runge-Kutta methods the Euler method is a first order method. It only approximates the slope at the starting point of the interval. Higher order Runge-Kutta methods use a mix of weighted approximation at both edges of the step as well as from the middle. The order of the truncation error mirrors the number of approximations for the slope that are being made for the first four Runge-Kutta methods. Note that this is not the case for fifth and higher order Runge-Kutta schemes, where much more computational effort is needed to increase the order of approximation any further. Thus, the fourth order method Runkge-Kutta 4 (RK4) represents an optimal method in terms of efficiency doing a global truncation error of $\mathcal{O}(h^4)$ and a local truncation error of $\mathcal{O}(h^5)$ [Gur18]. Nevertheless, this thesis uses an implicit Euler scheme, due to its low computational effort for long simulations. For more information on RK4 schemes in time-delayed systems, see B.1.
Now the implicit Euler scheme as it is used for the KGTI will be presented. Starting from the equations

$$\dot{E} = \left[-1 + i\left(|E|^2 - \delta\right)\right] E + hY, \tag{3.3}$$

$$Y = \eta e^{i\phi}\left(E_\tau - Y_\tau\right) + \sqrt{1-\eta^2} Y_0, \tag{3.4}$$

once again E_{n+1} has to be calculated from E_n, where $E_{n+1} = E(t_{n+1})$. For simplicity

$$\mathcal{L}_n = -1 + i\left(|E_n|^2 - \delta\right) \tag{3.5}$$

is introduced. Euler's method then leads to

$$\frac{E_{n+1} - E_n}{\Delta t} = \mathcal{L}_n E_n + hY_n \tag{3.6}$$

$$E_{n+1} = E_n + \Delta t\left(\mathcal{L}_n E_n + hY_n\right), \tag{3.7}$$

where Δt is used for the timestep since h is a system parameter. Now implicit Euler introduces t_{n+1} on both sides of the equation to get a better approximation by using the center of the timestep interval. This leads to

$$E_{n+1} = E_n + \Delta t\left(\mathcal{L}_n \frac{E_{n+1} + E_n}{2} + h\frac{Y_{n+1} + Y_n}{2}\right)\left(1 - \frac{\Delta t}{2}\mathcal{L}_n\right) E_{n+1} \tag{3.8}$$

$$= \left(1 + \frac{\Delta t}{2}\mathcal{L}_n\right) E_n + \frac{\Delta t}{2} h\left(Y_{n+1} + Y_n\right) \tag{3.9}$$

and finally

$$E_{n+1} = \frac{1}{1 - \frac{\Delta t}{2}\mathcal{L}_n}\left[\left(1 + \frac{\Delta t}{2}\mathcal{L}_n\right) E_n + \frac{\Delta t}{2} h\left(Y_{n+1} + Y_n\right)\right]. \tag{3.10}$$

Finally $N = \frac{\tau}{\Delta t}$ rounded to the next integer is introduced to write

$$Y_{n+1} = \eta e^{i\phi}\left(E_{n-N} - Y_{n-N}\right) + \sqrt{1 - \eta^2} Y_0, \tag{3.11}$$

which can be inserted for Y_{n+1} into (3.10). This is the first order implicit Euler scheme that is used for direct numerical simulations of the KGTI. To initialize a simulation a parameter array is passed to the integrator, also containing the time delay τ and the timestep Δt. The delay is implemented through the number of timesteps fitting into the delay which is the parameter N leading to a finite resolution of delay values. However, this does not cause problems in long-delay limit where $\tau \gg \Delta t$ is usually given. The initial condition is a $N \times 4$ array containing an interval of one delay in length for the real and imaginary part of each of the two fields E and Y. $V(1,:)$ corresponds to $E(t-\tau) = E_{n-N}$ and $Y(t-\tau) = Y_{n-N}$ while $V(N,:)$ contains the present state $E(t) = E_n$ and $Y(t) = Y_n$.
Finally, K simulation steps are specified where in each step a new point is calculated using the scheme described above. The new point is then written over $V(1,:)$ and either the indices or the array can be shifted in a cyclic way. Additionally, it is possible to save the whole timetrace of each simulation.

3.2. Numerical Path Continuation

Utilizing numerical path continuation, as it will be done throughout this thesis, holds several advantages that other tools such as direct numerical simulation (DNS) do not offer. With numerical path continuation, e.g., one can find and follow unstable solutions or folded structures such as snaking, which are hard to find with other numerical methods.
An example can be seen in Fig. 3.1. Two branches have been plotted in blue and turquoise, while the red and black dots represent DNSs from lower to higher and from

higher to lower values of Y_0, respectively. By only looking at the results from the DNSs, it is hard to interpret the bifurcation structure in this bistable hysteresis regime. Especially when the simulation time per step is not long enough to settle on a stable attractor transient points between the branches can occur as one can see for the black dots in particular. These do not represent real stable solutions. Only the continuation results shed light on the fine snaking structure, which is hidden beyond the hysteresis regime.
Using numerical path continuation, bifurcation points can be identified and tracked throughout the parameter space. This enables a good impression of structural changes occurring along a branch.

In order to understand the basic principles of continuation one has to keep in mind that

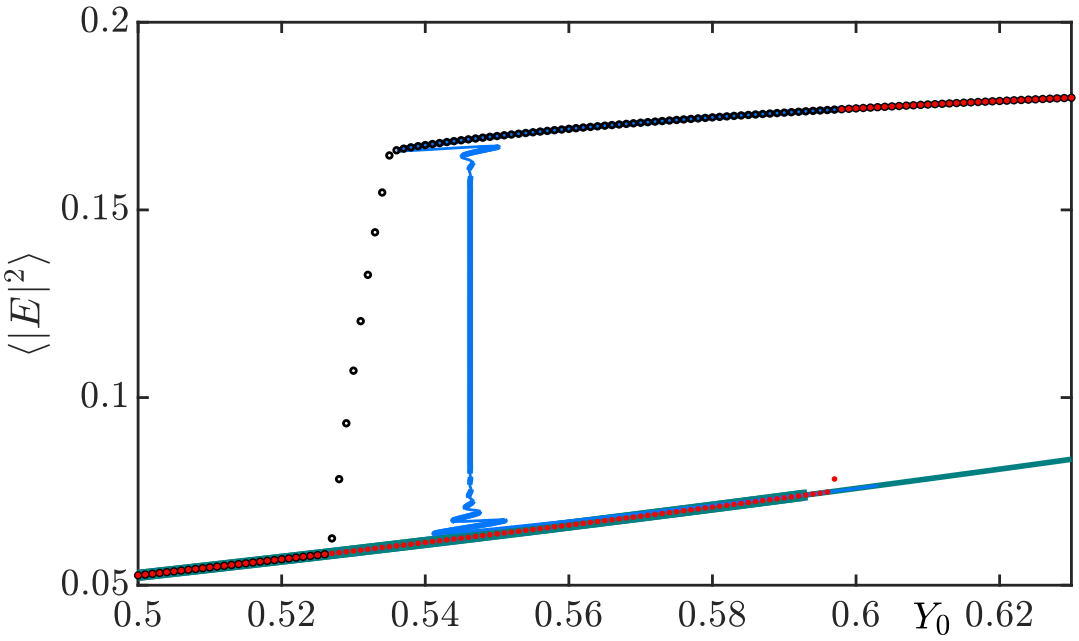

Figure 3.1: A comparison of numerical path continuation as lines and direct numerical simulations (DNSs) as dots. Both methods have used the result from the last step as the initial condition for the next, but unlike the continuation results, the DNSs will only fall onto stable attractors. Also, if the simulation time has not been chosen long enough, transients occur as solutions.

the considered branches consist of settled solutions $(\boldsymbol{x}^*, \mu^*)$. Here, steady state solutions are considered that are zeros of the function $\boldsymbol{F}(\boldsymbol{x}^*, \mu^*)$, since they fulfill

$$0 = \boldsymbol{F}(\boldsymbol{x}^*, \mu^*). \tag{3.12}$$

To start a branch an initial solution $(\boldsymbol{x}^0, \mu^0)$ is needed from which a small step in the parameter space can be taken such as $\mu^0 \rightarrow \mu^0 + \Delta\mu = \mu^1$. Now one has to find the $\boldsymbol{x}^1$, which fulfills $0 = \boldsymbol{F}(\boldsymbol{x}^1, \mu^1)$. There exist several algorithms for finding a zero of a function, such as the Newton's method [Thi21], but they mostly need a good initial prediction in order to converge. However, for a sufficiently small step $\Delta\mu$, $\boldsymbol{x}^0$ could be used as a first predictor. An even better strategy is the calculation of the branches tangent in $(\boldsymbol{x}^0, \mu^0)$ by using the systems Jacobian and extrapolate a predictor for the value of $\boldsymbol{x}^1$ at μ^1. However, this method has still a few flaws. Due to the fixed step Δ_μ, it will break down at saddle-node or fold bifurcations, where the branch does a turn around in μ, leading to a situation where there is no unique solution in μ. Thus,

a substitute bifurcation parameter assigning a unique value to each point of the branch would be desirable. A good option is the arclength, which behaves monotonous along the branch, even at folds. This leads to the pseudo-arclength method [Thi21], which introduces the arclength s as an additional parameter. The arclength is approximated locally as

$$(\Delta s)^2 = (\Delta \mu)^2 + (\Delta \boldsymbol{x})^2 \tag{3.13}$$

$$\approx (\boldsymbol{x}^{n+1} - \boldsymbol{x}^n)\frac{\partial \boldsymbol{x}}{\partial s}\Delta s + (\mu^{n+1} - \mu^n)\frac{\partial \mu}{\partial s}\Delta s. \tag{3.14}$$

This can be rewritten into a new function

$$p(\boldsymbol{x}, \mu, s) = 0 = (\boldsymbol{x}^{n+1} - \boldsymbol{x}^n)\frac{\partial \boldsymbol{x}}{\partial s} + (\mu^{n+1} - \mu^n)\frac{\partial \mu}{\partial s} - \Delta s. \tag{3.15}$$

The variable μ is now treated as an additional dependant variable being a function of the new control parameter s. Using the summary $\boldsymbol{y} = (\boldsymbol{x}, \mu)$, the extended system is

$$\boldsymbol{E}(\boldsymbol{y}, s) = \begin{pmatrix} F(\boldsymbol{y}, s) \\ p(\boldsymbol{y}, s) \end{pmatrix} = 0. \tag{3.16}$$

For a step $s^n \to s^n + \Delta s = s^{n+1}$ a prediction for $\boldsymbol{y}^{n+1} = (\boldsymbol{x}(s^{n+1}), \mu(s^{n+1}))$ can be found by calculating the tangent at $(\boldsymbol{y}^n, s^n)$. Therefor the Jacobian of the extended system $\boldsymbol{E}(\boldsymbol{y}, s)$ has to be used. Finally, Newton's method is applied to find the root of $\boldsymbol{E}(\boldsymbol{y}, s) = 0$ and $\boldsymbol{F}(\boldsymbol{x}, \mu) = 0$ alike. For a more detailed derivation and further explanations regarding this topic, see [Thi21].

4. Square-waves in an Injected Kerr Gires-Tournois Interferometer

4.1. Preliminary Results

To give a better understanding of this system, now a short overview over previously published results regarding the KGTI will be given. Due to the interplay of the Kerr nonlinearity, the detuning, and second-order chromatic dispersion, the KGTI can exhibit temporal-localized states (TLSs), such as dark and bright pulses [Sch+19b]. This has already been shown and analyzed, using a combination of direct numerical simulations and path continuation with the MATLAB continuation tool DDE-BIFTOOL [ELR02] for DDEs. Since this tool has not been designed for the implementation of DAE systems one can rewrite the KGTI system using a singular perturbation ansatz [Sch21]. By rewriting the second equation as

$$\epsilon \dot{Y}(t) = -Y(t) + \eta e^{i\varphi} \left[E(t-\tau) - Y(t-\tau)\right] + \sqrt{1-\eta^2} Y_0, \tag{4.1}$$

for a small ϵ, one can treat the DAE system as a DDE system.
Firstly, the KGTI shows continuous wave (CW) solutions which are the steady state solutions of the system. They result from the constant injection beam Y_0 and can become bistable for certain parameter regimes. The CW solution can be easily calculated analytically by setting $E(t) = E(t-\tau)$ and $Y(t) = Y(t-\tau)$. It is described by

$$|Y_0|^2 = \frac{\eta^2(h^2-2h) + \left[1 + 2\eta\cos(\varphi) + \eta^2\right]\left[1 + (\delta - I)^2\right] - 2h\eta[\cos(\varphi) - (\delta - I)\sin(\varphi)]}{h^2(1-\eta^2)} I, \tag{4.2}$$

where $I = |E|^2$ is the intensity [Sch21]. Within the bistable CW regime branches of periodic solution can be observed to emerge from Hopf bifurcations. These branches feature bright and dark TLSs that coexist within the same parameter regimes with hysteresis between them [Sch+19b]. The dark and bright TLSs can coexist due to third-order dispersion (TOD) within the system [PGG17][Sch+19b]. Lately, a normal form has been derived in the vicinity of the onset of bistability to extend the understanding of the mechanisms behind the formation and behavior of TLS in the KGTI system [SJG22]. It leads to a real cubic Ginzburg-Landau equation with additional terms such as third-order dispersion and nonlinear drift. These terms are responsible for the locking of domain walls in order to form pulses by providing each front with an oscillating tail that acts as a potential for other fronts. In a good cavity limit, for an almost perfect ($\eta \to 1$) feedback mirror, the dynamics are dominated by TOD. In this regime, the KGTI can be described by a Lugiato-Lefever equation [SGJ22].
In order to compare the analytical results from the normal form with the first-principle DAE model for the KGTI using numerical path continuation the DAE model needs to be implemented into MATLAB. Since the system resulting from the singular perturbation ansatz tends to be stiff for larger η, a recently developed extension for DDE-BIFTOOL is used throughout this thesis enabling the direct implementation of DAEs [HGJ21].

4.2. Numerical Path Continuation

4.2.1. Square-waves from a Supercritical Hopf Bifurcation

Starting with results contained from numerical path continuation now several branches of SW solution will be presented. In Fig. 4.1 such a SW branch for the parameter set $(\delta, h, \eta, \varphi, \tau) = (0.1, 2, 0.9, \pi, 300)$ is shown. It shows the formation of a periodic SW solution from the CW state in a supercritical Hopf bifurcation H_1, that grows in amplitude, and ultimately merges again with the CW state in another supercritical Hopf bifurcation H_2. Throughout this thesis, the bold and solid lines represent stable solutions while the thinner and dashed lines resemble unstable solutions. The measure $\langle . \rangle$ in the dependant variable stands for an integral over an orbit of the squared electric field or simply the squared electric field value in case of a periodic solution or a CW solution, respectively. The continuation parameter acting as control variable is the injection Y_0. (b,c) show two profiles for injection values marked by a dotted line in a). The one in

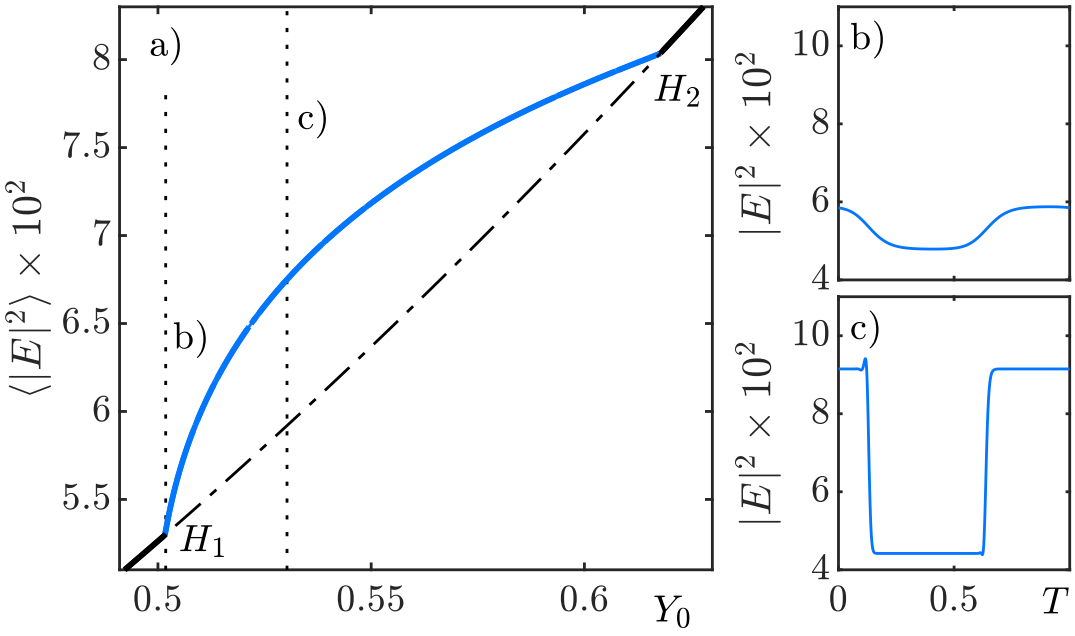

Figure 4.1: Bifurcation diagram showing a supercritical square wave branch (blue), emerging from a CW branch (black) that loses and recovers stability at the H_1 and H_2 in two supercritical Hopf bifurcations. The measure $\langle . \rangle$ in the dependant variable stands for an integral over an orbit of the squared electric field or simply the squared electric field value in case of a periodic solution or a CW solution, respectively. The continuation parameter is the injection Y_0. (b,c) show profiles, that have been taken from the square wave branch at its cross sections with the accordingly marked dotted lines. Parameters: $(\delta, h, \eta, \varphi, \tau) = (0.1, 2, 0.9, \pi, 300)$.

b) occurs right after the onset of SWs H_1 showing a small-amplitude sinus-like periodic solution with a period $T \approx 2\tau$. The solution then transforms along the branch into a well-developed SW with sharp transition layers as presented in c). This mechanism behind the formation of SWs is already well known. It has been described for example by [Ern08]. The sharp transition layers connecting the plateaus of the fully developed SWs exhibit almost no oscillating tail in accordance with the missing snaking in the

branch structure. The occurrence of fronts with an oscillatory tail typically corresponds to a branch with homoclinic snaking. This describes the possibility for different fronts to lock on discrete distances into bound states through interactions induced by their oscillatory tails [SJG22]. Such a behavior can be observed, if the detuning δ is increased as discussed in the following section.

4.2.2. Square-waves from a Subcritical Hopf Bifurcation

In Fig. 4.2 a branch can be seen, where the detuning has been increased to $\delta = 0.2$, while keeping all other parameters the same. As a consequence the lower Hopf bifurcation at

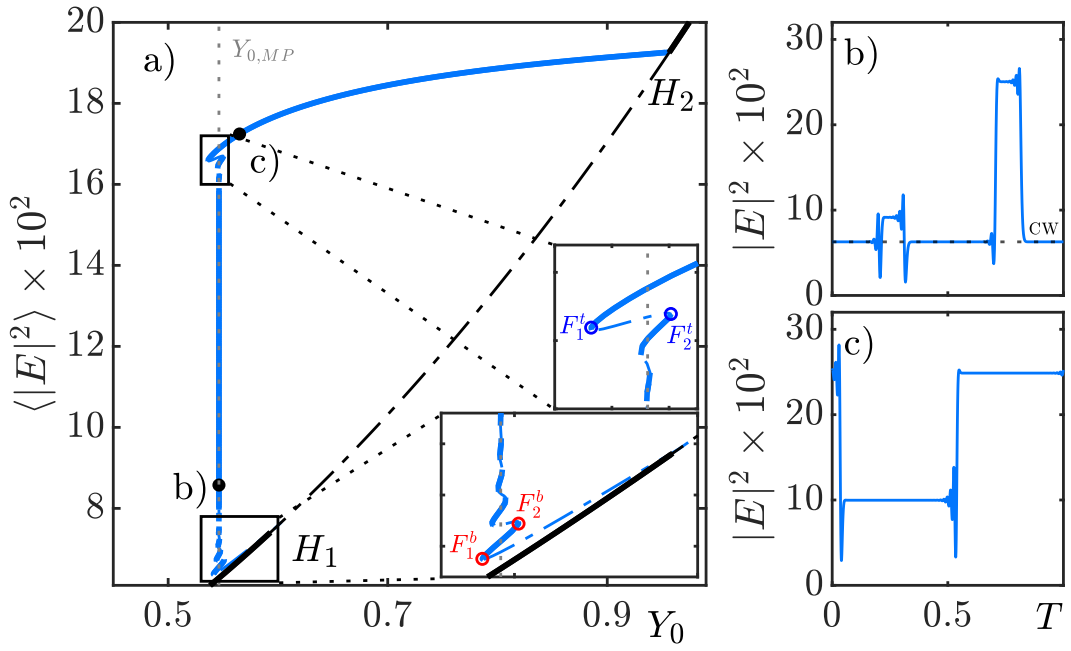

Figure 4.2: CW branch (solid black) losing stability (dash-dotted black) at H_1 in a subcritical Hopf bifurcation. The resulting SW branch (blue) experiences a series of saddle-node bifurcations building a collapsed snaking structure around a Maxwell line $Y_{0,MP} \approx 0.54625$. (b,c) Exemplary SW profiles marked in a). The SW solution possessing a complex shape with non-equidistant plateaus along the snaking region b), results in a SW with a 50% duty cycle c). Parameters: $(\delta, h, \eta, \varphi, \tau) = (0.2, 2, 0.9, \pi, 300)$.

H_1 became subcritical leading to a drastic change in the overall branch structure. At H_1 two pairs of unstable fronts emerge from the CW solution. Each of these pairs connects the stable CW state to one of the two emerging plateaus. Starting at the first fold F_1^b the opposed fronts for each pair move away from each other along a vertical Maxwell line [BK07] $Y_{0,\mathrm{MP}} \approx 0.54625$ where the velocity of opposing fronts is equal leading to arrested dynamics.
This results in profiles as the one shown in b) indicated by a black dot in a) with complex shaped solutions consisting of non-equidistant plateau regions. Due to the oscillatory tails induced by third-order dispersion, the fronts can also lock at several positions in the vicinity of the Maxwell line forming stable solutions at several preferred distances, especially in the snaking regions at both ends line where fronts are close to each other exerting a strong tail induced interaction. The top snaking then describes the situation

when the CW solution almost disappeared, and the fronts get into each other's potential again. Finally, the horizontal part of the branch after F_1^t contains a stable SW solution with a 50% duty cycle like the one shown in c). This solution consists of two plateaus connected by sharp transition layers each equipped with asymmetric oscillating tails.

4.2.3. Eigenvalues

Figure 4.3 shows the eigenvalue spectrum of the CW branch from Fig. 4.2 close to H_1 and H_2 in a) and b), respectively. The supercritical and subcritical cases do not differ in terms of eigenvalues such that it is not necessary to compare them. One can see the typical behavior at a Hopf bifurcation, where two complex conjugated eigenvalues cross the imaginary axis, leading to an emerging branch of stable periodic solutions. This process repeats for a whole cascade of frequencies. The resulting image shows the pseudo-continuous eigenvalue spectrum, discussed in earlier sections. Here, the CW solution shows an instability led by a branch with the longest finite wavelength $T \approx 2\tau$. In Fig. 4.4 one can see the first five periodic branches that become unstable, with the respective periods color coded. The n-th bifurcation belongs to a branch with a period of approximately $T = \frac{2\tau}{2n-1}$ in agreement with the results from other works [Fri+14].

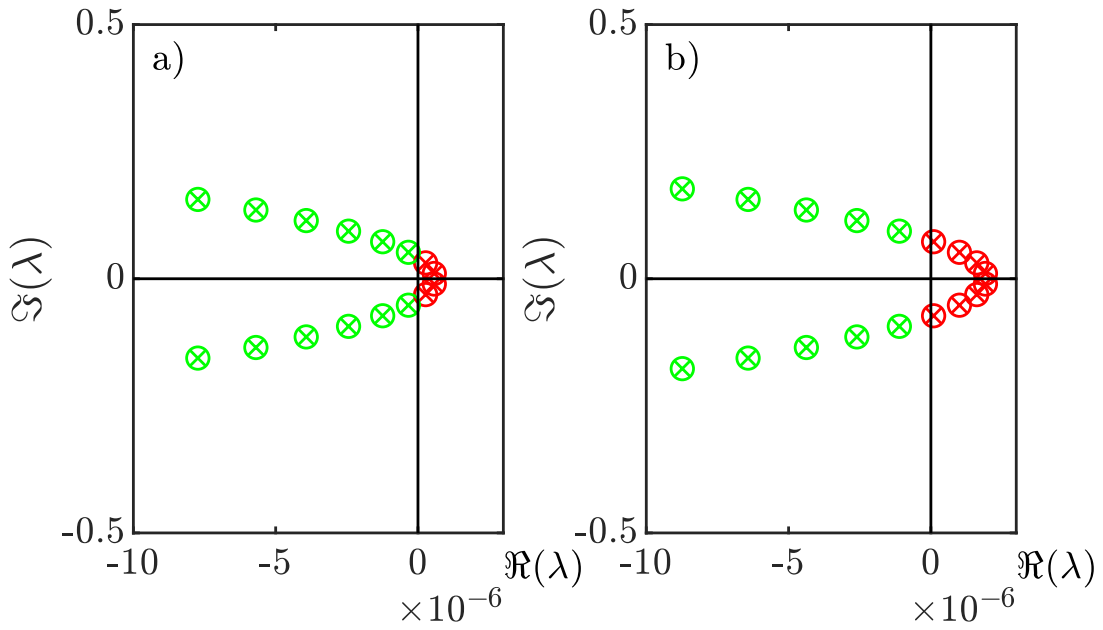

Figure 4.3: Eigenvalue spectrum of the CW branch from Fig. 4.2 at the two Hopf points H_1 and H_2 in a) and b), respectively. In terms of eigenvalues, the supercritical and subcritical case do not differ. Parameters: $(\delta, h, \eta, \varphi, \tau) = (0.2, 2, 0.9, \pi, 300)$.

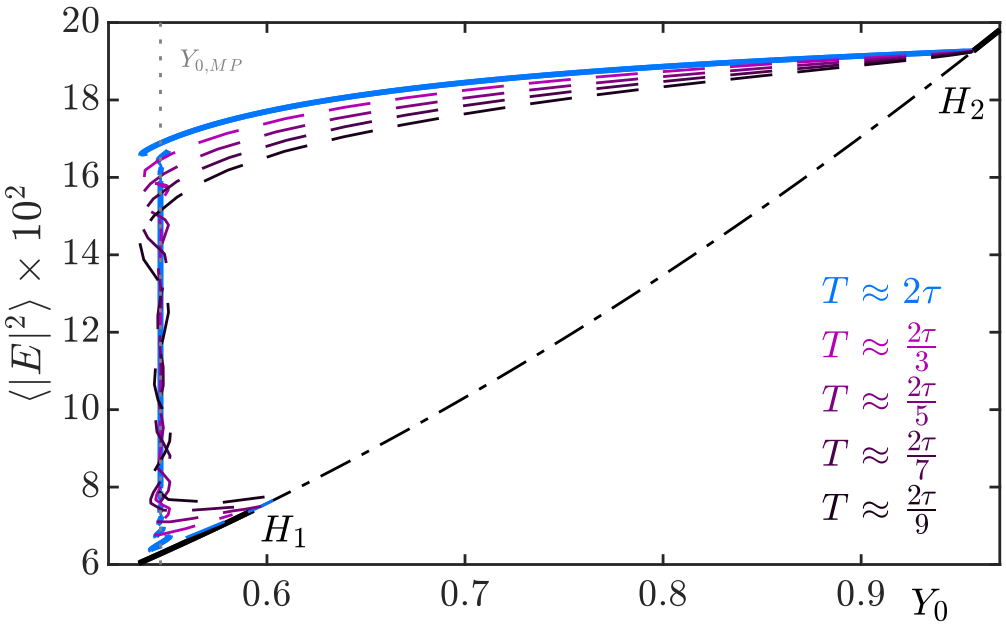

Figure 4.4: The first five periodic branches, that bifurcate around the upper supercritical Hopf point (H_2 in Fig. 4.2), with their respective periods in the bottom right corner. This corresponds to the cascade of Hopf bifurcations, that has been observed in Fig. 4.3. Parameters: $(\delta, h, \eta, \varphi, \tau) = (0.2, 2, 0.9, \pi, 300)$.

4.2.4. Period Doubling Route to Chaos

For even higher δ, the horizontal part of the SW branch loses stability over an increasingly large injection interval. After the bifurcation point, a cascade of Floquet multipliers leaves the unit circle at $\Re = -1$ and $\Im = 0$ indicating several period-doubling (PD) bifurcations. In contrast to a PD route to chaos consisting of consecutive PD bifurcations on the newly formed branches, this cascade of PD bifurcations appears on the initial branch. Accordingly the cascade of Floquet multipliers leaving the unit circle at $\Re = -1$ and $\Im = 0$ belongs to several consecutive onsets of PD routes to chaos. This is shown in Fig. 4.7 where several eigenvalues leave the unit circle in a cascade of PD bifurcations. a) and b) show the left and right PD bifurcation points, respectively.
Since it can become hard to do a numerical path continuation of a period-doubling route to chaos with increasingly long and complicated profiles, the behavior should be examined with direct numerical simulations. One starts with a known initial condition from the SW branch, close to the PD onset. Then, the injection is increased gradually, while each simulation leads to a new initial condition. This way, one can find a quasi-continuum of points that follow the stable attractor which connects to the branch. Since a PD route to chaos splits into an infinite number of possible solutions, many initial conditions have been started simultaneously with a small amount of noise to get the best possible impression of the system's behavior. Figure 4.5 shows the results for a detuning

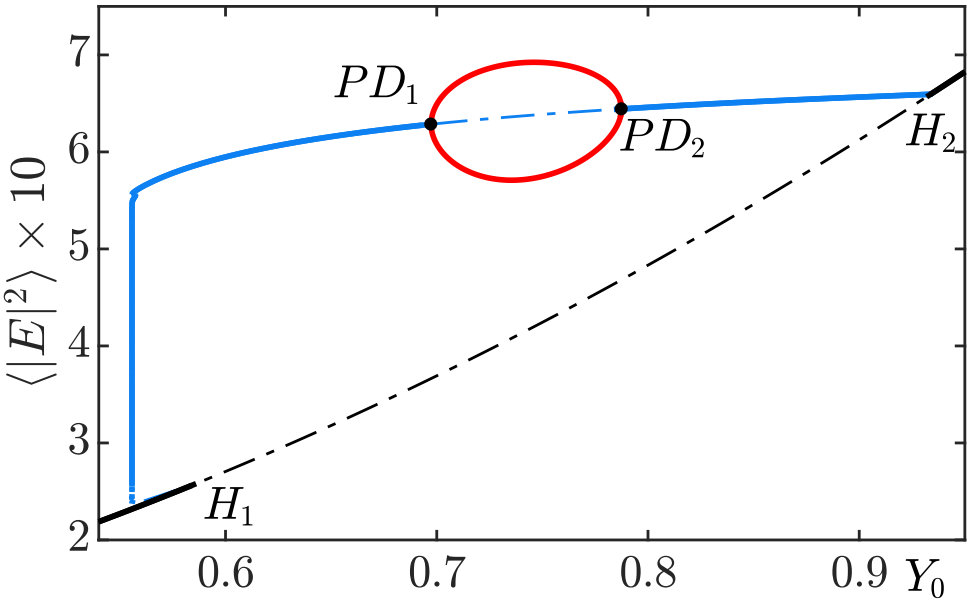

Figure 4.5: Bifurcation diagram, showing a subcritical square wave branch (blue), which bifurcates into a circle of period two solutions (red) at PD_1. The second bifurcation point PD_2 on the SW branch (blue) is too close to allow for higher period solutions or chaos. Parameters: $(\delta, h, \eta, \varphi, \tau) = (0.6872, 2, 0.682, \pi, 300)$.

slightly above the onset of the PD bifurcations. The period-two solution bifurcates from the main branch at PD_1, but before a further period doubling can occur, it closes back onto the horizontal part of the main branch in PD_2. The presented period-two branches are from another set of parameters with lower η, where the PD has been detected for

the first time, but it can be observed for $\eta = 0.9$ the same way.
At even higher values of δ, the unstable section increases, leading to full PD routes to chaos. This is apparent in Fig. 4.6. Noticeably the right PD route to chaos seems to bypass several PD bifurcations. When doing direct numerics, coming from higher injections, one will also find a period-doubling route to chaos, taking a different path into chaos through solutions with odd periods like 3τ and 5τ.

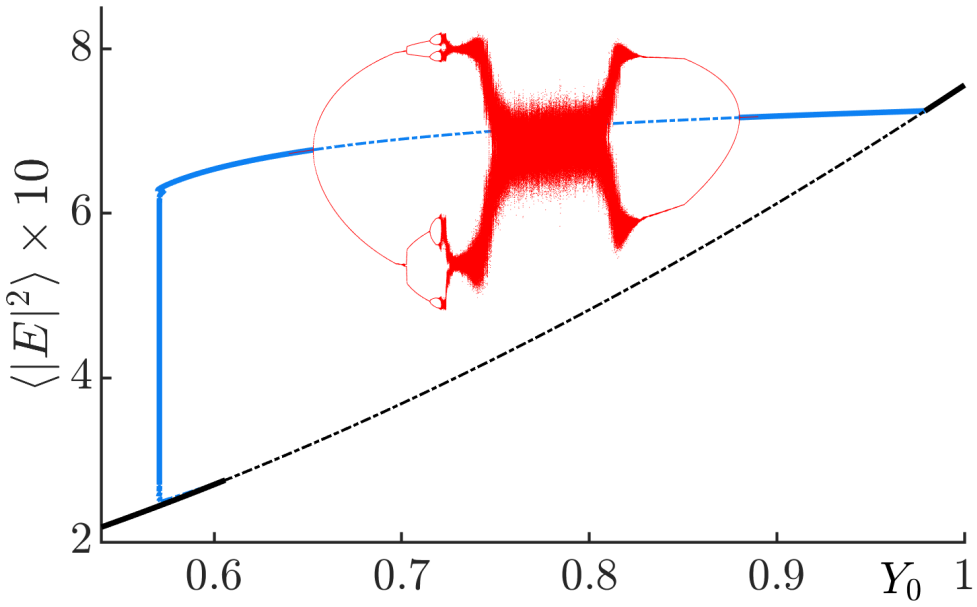

Figure 4.6: Bifurcation diagram, showing the same branch as in Fig. 4.5 for a slightly higher detuning δ. The PD points have further separated, leading to a full period doubling route to chaos. Parameters: $(\delta, h, \eta, \varphi, \tau) = (0.75, 2, 0.682, \pi, 300)$.

4.2.5. Period 3τ-solutions

The 3τ-periodic solutions presented in this section consist of three different plateau values of equal length of approximately τ. The triplet (p_1, p_2, p_3) of plateaus alternate in constant order, clearly driven by the switching mechanism which is typical for SWs. Hence, introducing plateau p_1 as initial condition would lead to an instant switch to p_2 as response, followed by a switch to p_3 after one round-trip of length τ. It is due to this, that these solutions will be called three-plateau SWs (SW_3s).
An exemplary branch of these SW_3 solutions is shown in Fig. 4.8. The two presented 3τ-periodic branches $b_1^{3\tau}$ and $b_2^{3\tau}$ are each closed, not connecting to any other branch. The zoom in Fig. 4.9 shows that the folds $F_1^{3\tau}$ of the branch $b_1^{3\tau}$ look like a continuation of the two major folds $F_2^{3\tau}$ of the branch $b_2^{3\tau}$ raising the impression that the snaking structures collided leading to the separation of the branches.

The profiles in Fig. 4.8 (b,c) match this observation. In c) three pulses equidistant pulses arise from the CW solution as it was the case for SW growth in case of a subcritical Hopf bifurcation. The SW_3 solution in b) results from fronts that have been locked in a stable configuration after ascending along the Maxwell line. Finally the PD points in Fig. 4.8 on $b_2^{3\tau}$ as well as in Fig. 4.9 on $b_1^{3\tau}$ have to be mentioned marking onsets of the

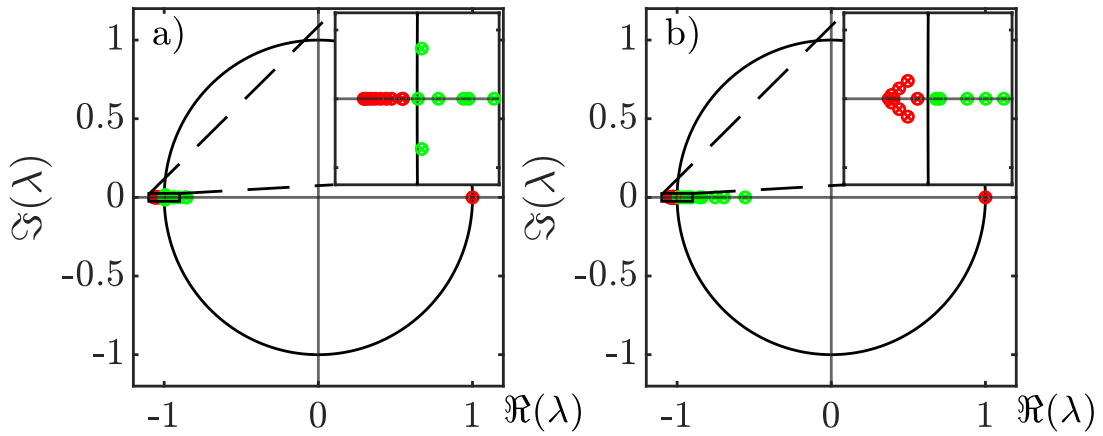

Figure 4.7: Eigenvalue spectrum at the left a) and right b) PD bifurcation points in Fig. 4.6, where a cascade of PD bifurcations sets in. Simultaneously several Hopf bifurcations can be observed. Parameters: $(\delta, h, \eta, \varphi, \tau) = (0.75, 2, 0.682, \pi, 300)$.

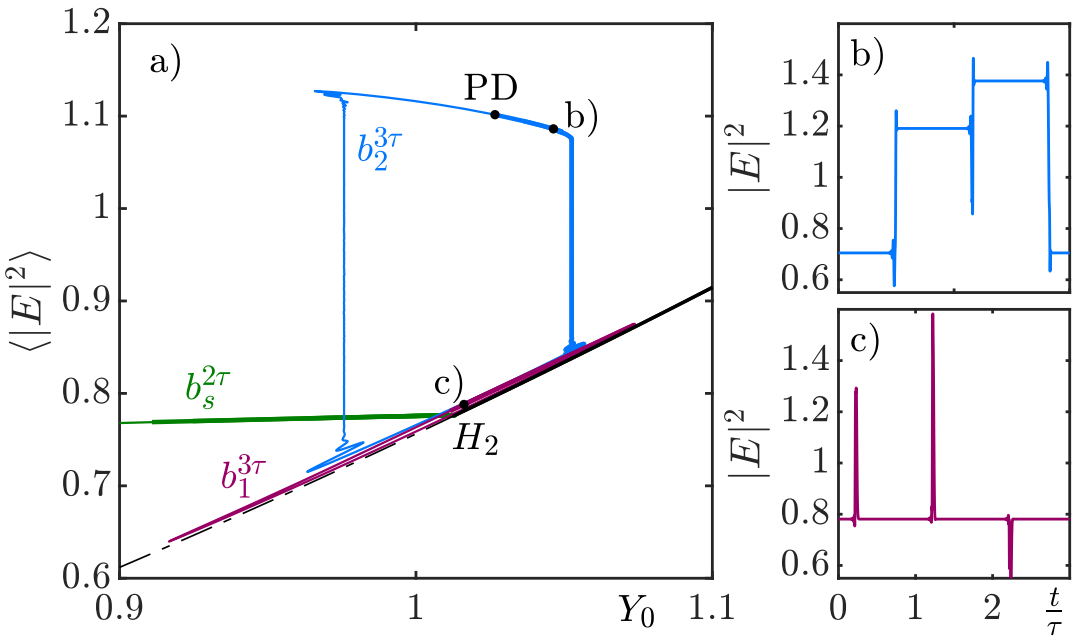

Figure 4.8: a): Branches featuring periodic solutions consisting of three plateaus each with a length of approximately τ. The respective branches $b_1^{3\tau}$ and $b_2^{3\tau}$ are detached to each other as well as the CW branch. $b_s^{2\tau}$ is the respective SW branch, reconnecting with the CW branch at the upper Hopf H_2. (b,c): one profile from the two 3τ-periodic branches each. The branches and respective profiles are colorized and labeled accordingly. b) shows that $b_2^{3\tau}$ is a branch of SW_3 solution, while c) only shows three pulses emerging from the CW separated by τ from each other. Parameters: $(\delta, h, \eta, \varphi, \tau) = (0.8, 2, 0.682, \pi, 300)$.

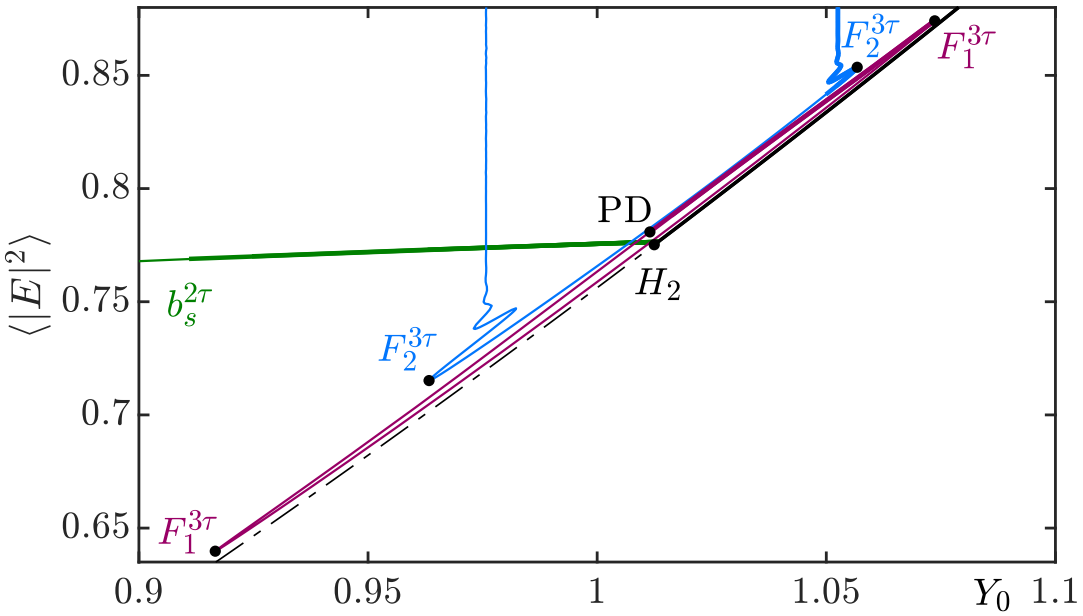

Figure 4.9: Zoom on the 3τ-periodic branches to illustrate the detached branch structure. The folds $F_1^{3\tau}$ and $F_2^{3\tau}$ are the major folds belonging to the branches $b_1^{3\tau}$ and $b_2^{3\tau}$ from Fig. 4.8, respectively. Also another PD bifurcation arises when the $F_1^{3\tau}$ branch loses stability. Parameters: $(\delta, h, \eta, \varphi, \tau) = (0.8, 2, 0.682, \pi, 300)$.

previously mentioned alternative PD route to chaos. Though existent, solutions with period 5τ or higher are out of the scope for this thesis.

4.3. Two-parameter Continuations

Two-parameter diagrams can help to get a better understanding of the system's behavior. They allow for the tracking of different bifurcation points throughout the parameter space. The important bifurcation points used for continuation are the PD onset, the major folds visible in Fig. 4.2, and finally the Hopf points H_1 and H_2. The two figures 4.10 and 4.11 show the (Y_0, δ)-plane for the two different values of η from before. While the structures seem to change in relative size and form, the essential structure of the two diagrams remains the same. The inset in Fig. 4.11 shows the folded structure of the before-mentioned period-doubling cascade. The folds are closer together here. One can also see that the two Hopf (H) points are connected arising pairwise in two notable points depending on the control variable. The Hopf point either arise in the minimum in δ or in the folding point $P_0 = (Y_0^c, \delta_c)$, if Y_0 is varied. Especially in Fig. 4.10, one can see the fundamental fold pairs emerging in P_0. This leads to the formation of the snaking structure, which has been observed for the subcritical case. So at P_0 the left Hopf bifurcation switches from supercritical to subcritical. Indeed, the colored areas emphasize three important sections. These are supercritical SW growth (red), subcritical SW growth (blue), and PD region (green).
For the lower η, the numerical path continuation could not recognize a fold in the δ vicinity of P_0 since the folding region became very flat for these δ values. Thus, the dotted points have been calculated manually. To mention is also the 3τ-periodic regime

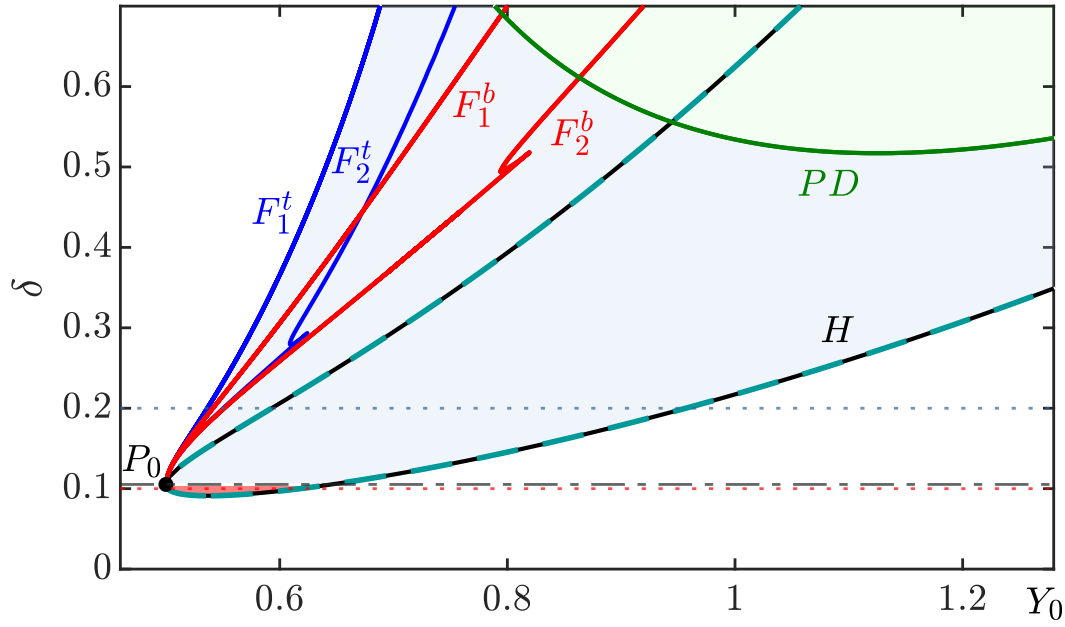

Figure 4.10: Bifurcation diagram of the (δ, Y_0) plane. It shows the continuations of the most important bifurcation points. These are the Hopf (H) bifurcations, where the SW branch arises from the CW solution, the onset of PD bifurcations, and the major folds marked in Fig. 4.2. The two dotted lines mark Fig. 4.1 ($\delta = 0.1$) and Fig. 4.2 ($\delta = 0.2$). The major supercritical, subcritical, and chaotic regimes are colorized as red, blue, and green, respectively. Parameters: $(h, \eta, \varphi, \tau) = (2, 0.9, \pi, 300)$.

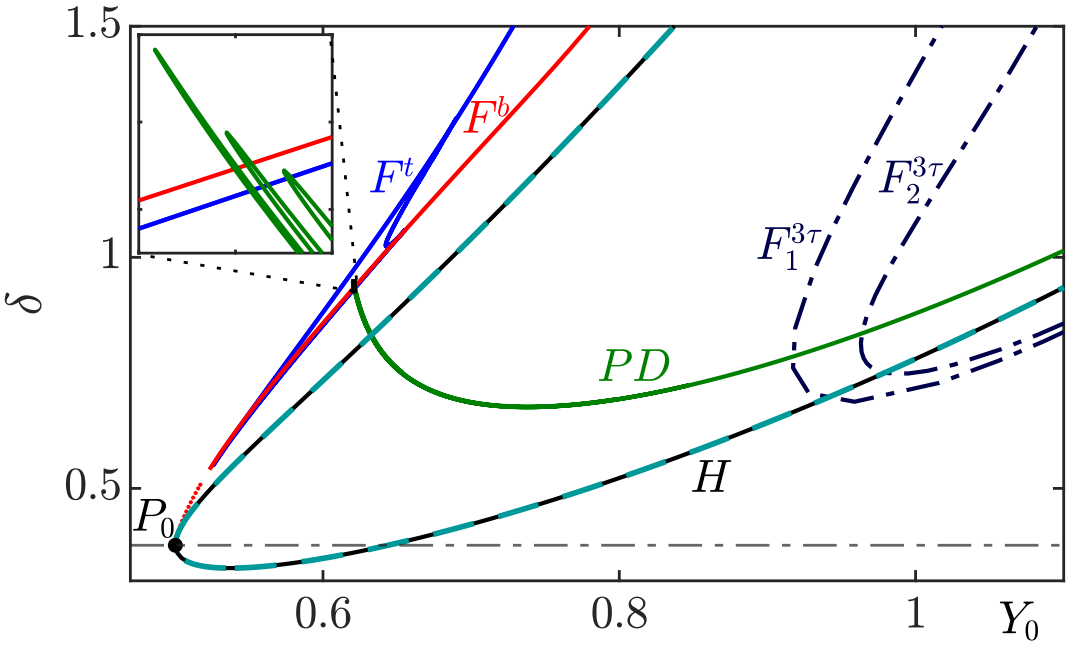

Figure 4.11: Bifurcation diagram where the folded structure of the PD branch is emphasized. Parameters: $(h, \eta, \varphi, \tau) = (2, 0.682, \pi, 300)$.

$F^{3\tau}$ where the major folds from before have been plotted with dash-dotted lines. From direct numerical simulation these three-plateau solutions can also be found in a vicinity of this regime in the (Y_0, δ) plane. However, these are slow transients, decaying to the SW or CW solution, depending on the regime one is on.
Finally, the hooks appearing on the fold branches have to be mentioned. They exist for both parameter sets, but seemingly move below the period doubling region for a higher η. In these regions, the Maxwell line splits into two parallel Maxwell lines, which leads to novel behavior. However, the study of this novel regime is out of the scope of this thesis.

To close this section, the behavior of the Hopf points for varying η and φ shall be investigated. Especially the second contemplation is significant in order to check if SWs are a unique feature for $\varphi = \pi$ or if they continue to exist in a vicinity of that value. By looking at Fig. 4.12 one can confirm that the SW branch exists for other values of φ. Nevertheless, the behavior, especially for lower values yet of φ, has to be explored in more detail.
Figure 4.13 shows, that minimum feedback ($\eta > 0$) is needed in order to find the SW branch. It also shows, that in the good cavity limit higher injections are needed, to get SWs.

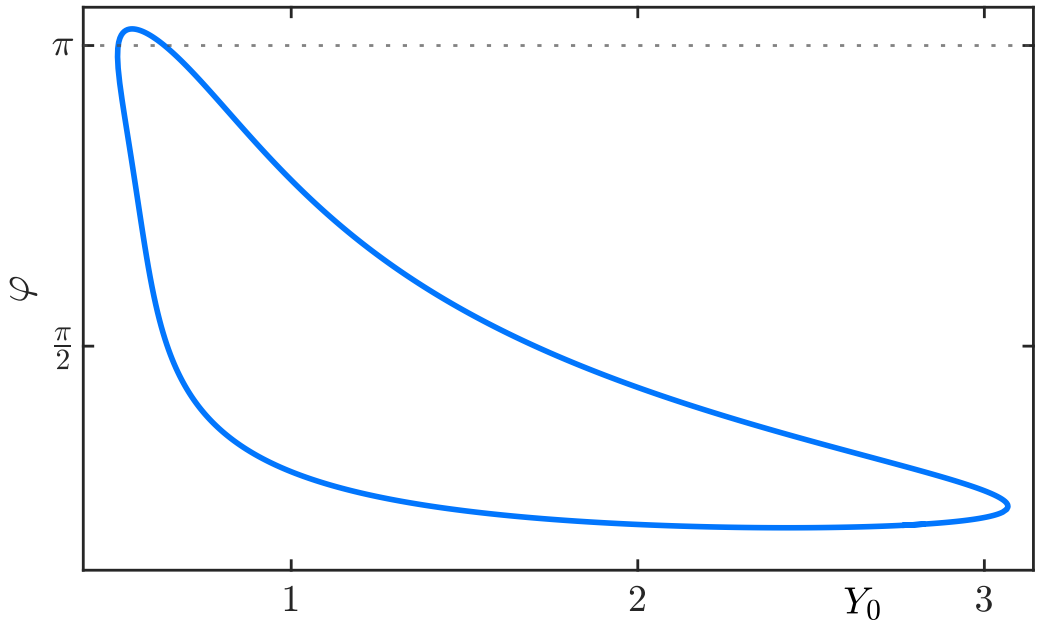

Figure 4.12: Bifurcation diagram of the Hopf points (c.f. H_1 and H_2 in Fig. 4.1) in the (φ, Y_0) plane. The value $\varphi = \pi$ has been marked by a dotted line. These results show that the square wave branches continue to exist in the vicinity of $\varphi = \pi$ and are not a unique phenomenon for this single value. To be sure a few profiles for other values of φ have been calculated as well. However, these are not included in this thesis. Parameters: $(\delta, h, \eta, \tau) = (0.37, 2, 0.682, 300)$.

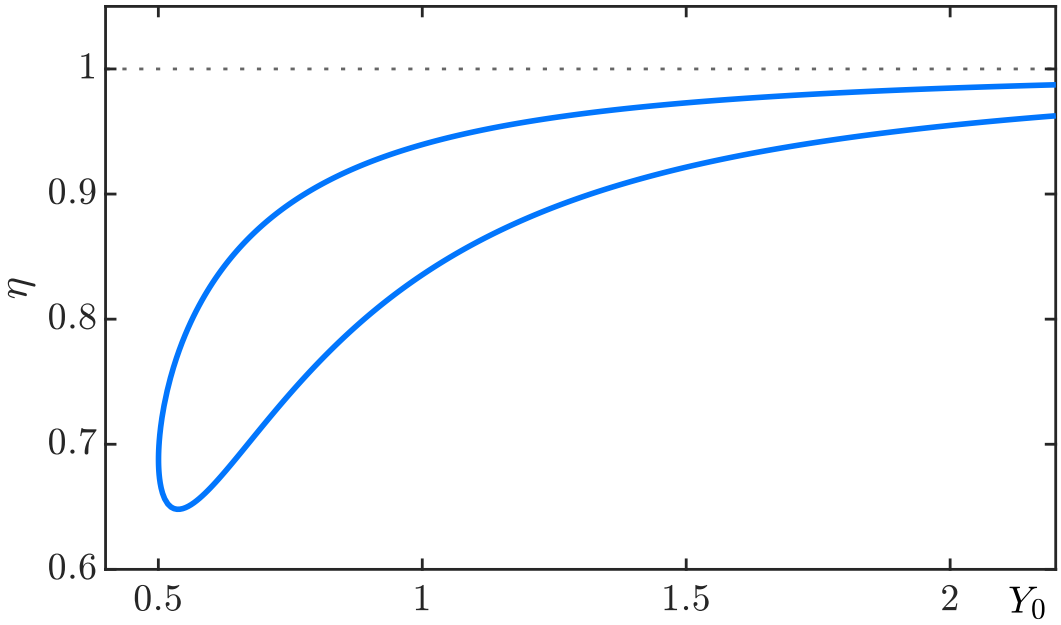

Figure 4.13: Two-parameter bifurcation diagram of the Hopf points in the (η, Y_0) plane. Since η is a reflection coefficient, the asymptotic behavior in the limit $\eta \to 1$ can be well understood. Higher injection values are needed to get SWs if η is raised towards this limit. Further, the branch shows that a minimum feedback ($\eta > 0$) is needed, in order to find the SW branch. Parameters: $(\delta, h, \varphi, \tau) = (0.37, 2, \pi, 300)$.

4.4. Plateau Analysis

In the following section an approach for describing SWs analytically is presented. This is based on the idea to consider the SW solution as a steady state of the system within a comoving frame, leading to $\dot{E}(t) = 0$. Furthermore one can assume a two-plateau approximation, where the simplified SW can be written as

$$(E, Y)(t) = \begin{cases} (E_1, Y_1) & \text{if } t \in [0, \tau[\\ (E_2, Y_2) & \text{if } t \in [\tau, 2\tau[\end{cases} \tag{4.3}$$

with two plateaus (E_1, Y_1) and (E_2, Y_2) of equal length τ. Inserting this into the system yields four equations, since $(E, Y)(t) = (E_1, Y_1)$ leads to $(E, Y)(t - \tau) = (E_2, Y_2)$ and vice versa:

$$0 = (i[|E_1|^2 - \delta] - 1)E_1 + hY_1 \tag{4.4}$$

$$0 = -\eta[E_2 - Y_2] + \sqrt{1 - \eta^2}Y_0 - Y_1 \tag{4.5}$$

$$0 = (i[|E_2|^2 - \delta] - 1)E_2 + hY_2 \tag{4.6}$$

$$0 = -\eta[E_1 - Y_1] + \sqrt{1 - \eta^2}Y_0 - Y_2 \tag{4.7}$$

Replacing Eqs. 4.4 and 4.6 as well as Eqs. 4.5 and 4.7 by their sum and difference and inserting the resulting equations for $Y_1 - Y_2$ and $Y_1 + Y_2$ into the other two, yields

$$0 = (i[|E_1|^2 - \delta] - 1)E_1 - (i[|E_2|^2 - \delta] - 1)E_2 + h[Y_1 - Y_2] \tag{4.8}$$

$$0 = (i[|E_1|^2 - \delta] - 1)E_1 + (i[|E_2|^2 - \delta] - 1)E_2 + h[Y_1 + Y_2] \tag{4.9}$$

$$Y_1 - Y_2 = \frac{\eta}{\eta + 1}[E_1 - E_2] \tag{4.10}$$

$$Y_1 + Y_2 = \frac{\eta}{\eta - 1}[E_1 + E_2] + 2\frac{\sqrt{1 - \eta^2}}{1 - \eta}Y_0. \tag{4.11}$$

Thus, one can eliminate Y_1 and Y_2 leading to a system of two algebraic equations

$$0 = i[|E_1|^2 - \delta]E_1 - i[|E_2|^2 - \delta]E_2 - k_+[E_1 - E_2] \tag{4.12}$$

$$0 = i[|E_1|^2 - \delta]E_1 + i[|E_2|^2 - \delta]E_2 - k_-[E_1 + E_2] + 2\gamma_0 Y_0, \tag{4.13}$$

using the simplifications $k_+ = \frac{1+\eta(1-h)}{1+\eta}$, $k_- = \frac{1-\eta(1-h)}{1-\eta}$, $\gamma_0 = h\frac{\sqrt{1-\eta^2}}{1-\eta} = h\sqrt{\frac{1+\eta}{1-\eta}}$. Since Y_1 and Y_2 are functions of the E_1 and E_2, fully determined through Eqs. 4.10 and 4.11, the full information is conserved.

4.4.1. Continuous Wave Branch

From here one can find an expression for the CW branch by simply setting $E_1 = E_2 = E_s$ and solving

$$0 = i[|E_s|^2 - \delta]E_s - k_+E_s + \gamma_0 Y_0, \tag{4.14}$$

which results from Eq. (4.13), since Eq. (4.12) becomes trivial. Inserting the intensity $I_s = |E_s|^2$ leads to

$$Y_0 = \frac{1}{h}\sqrt{\frac{1 - \eta}{1 + \eta}}\sqrt{\left(k_-^2 + [I_s - \delta]^2\right) I_s}, \tag{4.15}$$

which can also be recovered from the CW solution presented in Section 4.1 by [Sch21] for $\varphi = \pi$.

4.4.2. Square-wave Branch

In the subcritical case, the CW solution survives as a third plateau along the Maxwell line. Thus, an analytic calculation of the SW branch using the two-plateau assumption will not be able to describe the full SW branches in any parameter set. However, the horizontal part of the subcritical branches, as well as the whole supercritical branches, should fulfill the assumptions. To get to a SW solution Eq. (4.12) is rewritten. Taking the modulus square and inserting the respective plateau intensities leads to

$$\left([I_2-\delta]^2+k_+^2\right)I_2=\left([I_1-\delta]^2+k_+^2\right)I_1. \tag{4.16}$$

This equation is fulfilled trivially for $I_1=I_2$, which corresponds to the CW solution. To find another solution, one can use factorization since a solution of Eq. 4.16 is already known. Since Eq. 4.16 is of third order in intensity the remaining polynomial is of second order. Calculating

$$\begin{aligned}
0 &= k_+^2[I_1-I_2]+I_1[I_1-\delta]^2-I_2[I_2-\delta]^2 && (4.17)\\
&= k_+^2[I_1-I_2]+I_1(I_1^2-2\delta I_1+\delta^2)-I_2(I_2^2-2\delta I_2+\delta^2) && (4.18)\\
&= (k_+^2+\delta^2)[I_1-I_2]+I_1(I_1^2-2\delta I_1)-I_2(I_2^2-2\delta I_2) && (4.19)\\
&= (k_+^2+\delta^2)[I_1-I_2]+I_1^3-2\delta I_1^2-I_2^3+2\delta I_2^2+[2\delta I_1I_2-2\delta I_1I_2] && (4.20)\\
&= \left(k_+^2+\delta^2-2\delta(I_1+I_2)\right)[I_1-I_2]+I_1^3-I_2^3+[I_1^2I_2-I_1^2I_2+I_1I_2^2-I_1I_2^2] && (4.21)\\
&= (k_+^2+\delta^2+I_1^2+I_2^2+I_1I_2-2\delta(I_1+I_2))[I_1-I_2] && (4.22)\\
&= \left[I_1^2+I_1(I_2-2\delta)+I_2^2-2\delta I_2+k_+^2+\delta^2\right][I_1-I_2], && (4.23)
\end{aligned}$$

where at the blue terms the square is completed, leads to the other solutions as a second order polynomial $I_1(I_2)$ or $I_2(I_1)$, which solves to

$$I_{1,2}=\frac{1}{2}\left(2\delta-I_{2,1}\pm\sqrt{4\delta I_{2,1}-3I_{2,1}^2-4k_+^2}\right). \tag{4.24}$$

Now it is possible to calculate one plateau value I_i as function of the other one. By rewriting Eq. (4.12) as

$$E_2=\frac{k_+-i(I_1-\delta)}{k_+-i(I_2-\delta)}E_1, \tag{4.25}$$

another variable can be eliminated from the system. However, one should note, that Eq. (4.24) yields two solutions for I_1 and I_2 each, since Eq. (4.24) does not depend on the injection Y_0. An inserted value $I_1=I$ could be the lower plateau for one value of Y_0 and the higher plateau for another. Thus the notation

$$I_\pm=\frac{1}{2}\left(2\delta-I\pm\sqrt{4\delta I-3I^2-4k_+^2}\right) \tag{4.26}$$

is preferred. To get the injection dependence one can use Eq. (4.13) with Eq. (4.25) and take the modulus square again, yielding

$$Y_0(I_1,I_2)=\frac{1}{2k_0}\sqrt{\left|k_--i\left[I_1-\delta\right]+\left[k_--i[I_2-\delta]\right]\frac{k_+-i[I_1-\delta]}{k_+-i[I_2-\delta]}\right|^2I_1}. \tag{4.27}$$

Plotting the plateau values $(I,I_\pm)$ over $Y_0(I,I_\pm)$ results in the branch as shown in Fig. 4.14. The dotted lines illustrate how one inserted intensity I can belong to two different SWs at different injection values, which correspond to the two solutions of the quadratic equation $I_-(I)$ and $I_+(I)$.

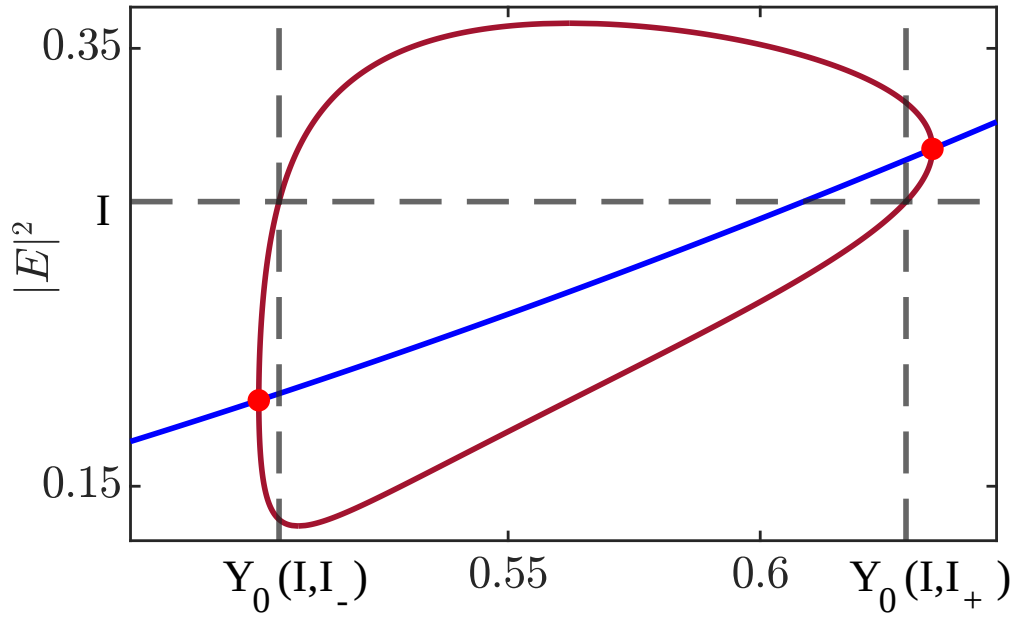

Figure 4.14: The blue line shows the analytic results for the CW branch, while the red lines are the solutions for the SW plateaus belonging to a supercritical SW branch. The intensity value I is a plateau value of two square-waves occuring for different injections $Y_0(I, I_-)$ and $Y_0(I, I_+)$. The found quadratic equation yields $I_\pm = f(I)$ since it does not depend on Y_0. If one then inserts I with one of its partners into the equation for Y_0, the respective injection value is found .

4.4.3. Calculating Bifurcation Points

Figure 4.14 also includes two red points, which mark the Hopf bifurcation points. The discussion from the last section gives a simple condition for a bifurcation point: The intensity values I_H of the bifurcation points are the only values where one solution of the quadratic equation is I_H itself. They are not to be confused with the extremal values of the branches, which correspond to the points where the square root disappears. Hence one can write a condition for the extremal values I_E as

$$I_+(I_E) = I_-(I_E) \neq I_E, \tag{4.28}$$

which is equivalent to a vanishing radicant. But more importantly the bifurcation points can be rewritten as the two solutions of the equation $I_\pm(I_H) = I_H$, which have the simple form

$$I_{H_{1,2}} = \frac{2}{3}\delta \pm \frac{1}{3}\sqrt{\delta^2 - 3k_+^2}. \tag{4.29}$$

The injection value of the Hopf points can then be found by inserting I_H into the SW solution Eq. 4.15.

4.4.4. Comparing Numerical and Analytical Results

To close this chapter on the analytical description of SWs in a KGTI system, a few analytically calculated branches shall be presented and compared to their numerical counterparts from earlier sections. In Fig. 4.15, one can see the supercritical branch from Fig. 4.1 in plateau representation. This means that the upper and lower part of the bubble belong to the same solution describing the upper and lower plateau value, respectively. Blue lines belong to numerical results, while red lines come from the derived equations. One can see that the two approaches result in a excellent agreement. Interestingly, even close to the bifurcation point, the two-plateau approximation seems to hold, which can be seen in b).
In Fig. 4.16 the branch from Fig. 4.2 can be seen. Here, there appears to be more disagreement between numerical and analytical results, especially around the Maxwell line. This was to be expected since the profiles respective do not fulfill a two-plateau approximation, as visible in b). However, on the horizontal part of the branch, after F_1^t, the analytical prediction approaches the numerical results, as shown in c). Another interesting result is the correct analytical prediction of the Hopf points, especially the one lower in injection since it is in the region where the periodic branch itself is not described correctly.
Due to this result, it seems like an obvious next step to compare the analytical and numerical predictions for the Hopf points over a larger domain of parameters. This has already been done in figs. 4.10 and 4.11, where the black-turquois striped line consists of the numerical (black) and analytical (turquoise) results for the Hopf points. Thus, it can be concluded that an appropriate analytical description for SWs in the KGTI system has been derived successfully. A promising next step would be a plateau analysis based on a three-plateau approximation to describe the behavior of SW_3 solutions. Thinking ahead, an n-plateau analysis could be interesting for future investigations. This is however out of the scope of this thesis.

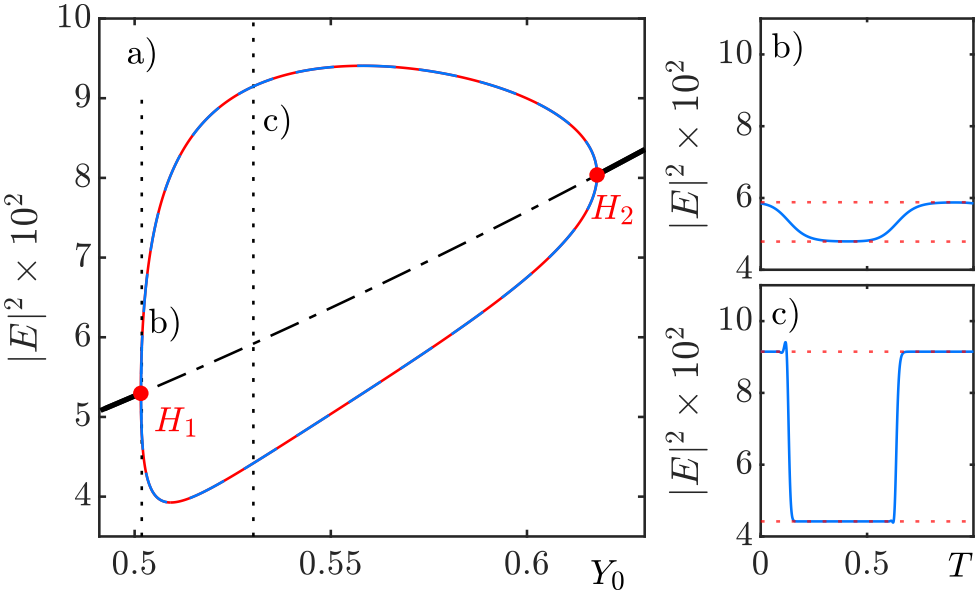

Figure 4.15: Comparison of the results from numerical path continuation (blue) with the analytical approximation (red) for the supercritical SW branch from Fig. 4.1. One can see the two plateau values emerging from the CW solution at the Hopf points H_1 and H_2 in a supercritical pitchfork bifurcation. The dotted lines mark the injection values for which profiles have been plotted in (b,c). Parameters: $(\delta, h, \eta, \varphi, \tau) = (0.1, 2, 0.9, \pi, 300)$.

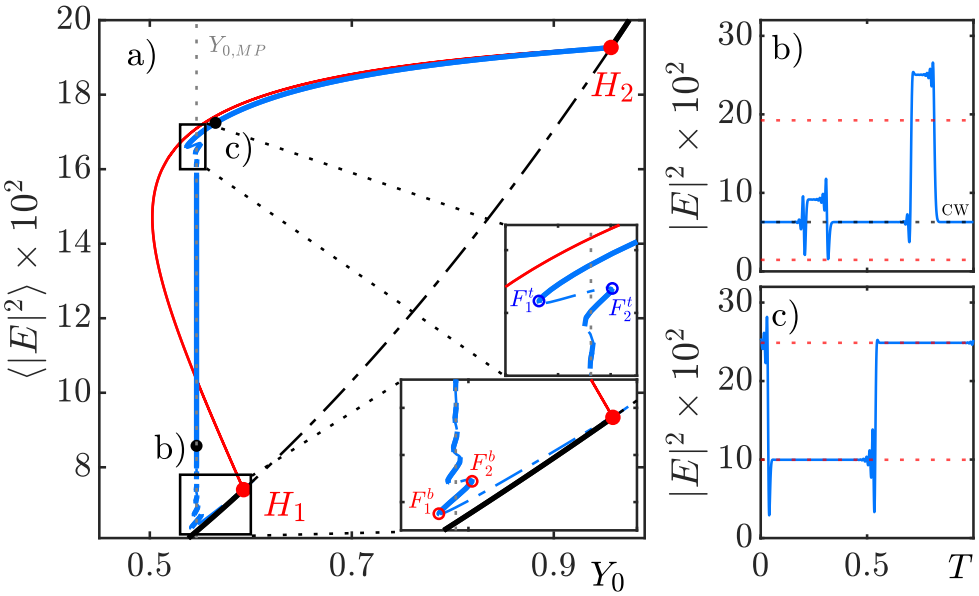

Figure 4.16: Comparison of the results from numerical path continuation (blue) with the analytical approximation (red) for the subcritical SW branch from Fig. 4.2. The analytical prediction deviates from the branch close to the subcritical Hopf bifurcation at H_1 since the profiles in that vicinity do not fulfill the two plateau approximations, as indicated in b). c) shows a stable square wave with plateau values well predicted by the analytical results. The bifurcation point H_1 is also predicted correctly. Parameters: $(\delta, h, \eta, \varphi, \tau) = (0.2, 2, 0.9, \pi, 300)$.

4.5. Evolution of Temporal Localized States on Square-waves

The presence of the oscillatory tails of SWs opens up the possibility to build more complex patterns. As already discussed, the antiperiodicity in the square wave regime inverts the whole solution after each roundtrip. Nevertheless, not every possible configuration of fronts and pulses is stable.
Figure 4.17 is a schematic example of such an initial condition where an analytically calculated plateau value hosts two regimes of different width of the respective partner plateau value. The results are presented in a quasi-space-time representation, as introduced in Section 2, where the full timetrace has been cut into sections of length $\sigma = 2\tau + \epsilon$, with ϵ being a small correction to compensate drift. This can be done since the long-delay limit is considered leading to a separation of timescales: The dynamics within each period evolve on the scale σ, while the dynamics between the periods evolve in θ direction. σ can be compared to a quasi-spatial variable where the SW turns from a periodic solution in the purely temporal dynamics into a steady state within the new quasi-spatial variable. This steady state can then host other waveforms such as temporal localized states that act as a perturbation of the steady state. Hence, one can observe the temporal evolution of this perturbations that live on the SW where temporal evolution means the evolution in direction of the slow timescale θ.
The resulting dynamics can be described using concepts from spatially extended sys-

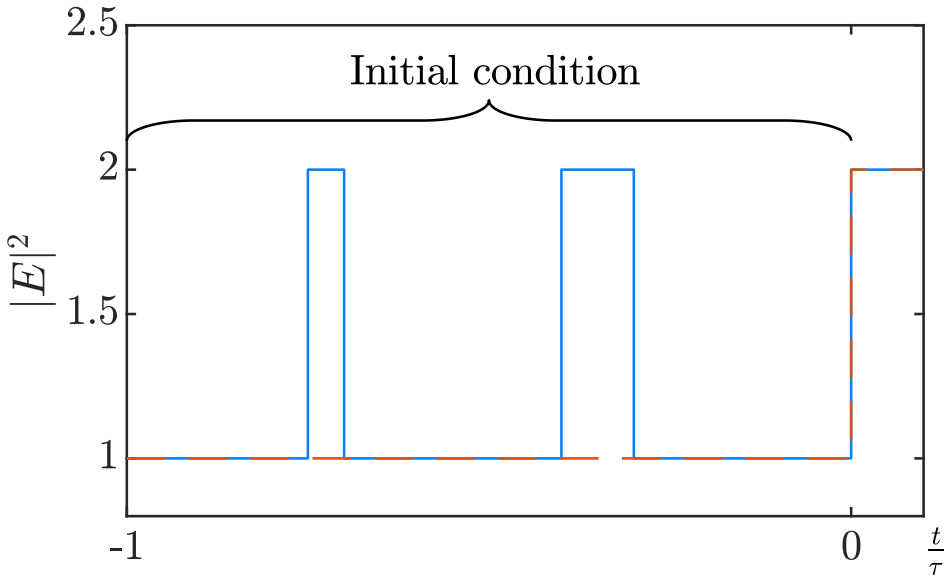

Figure 4.17: Initial condition of length τ consisting of a SW plateau (red) with two intersections of the respective other plateau (blue). Only the interval $t \in [-1, 0]$ has to be given as initial condition for numerical integration. Due to the antiperiodic behavior in the square wave regime, the whole initial condition is expected to be switched around after each roundtrip τ. The plateaus can be taken from the analytical calculations

tems, such as coarsening. Coarsening describes a process in conserved dynamics governed by diffusion. Consider two substances in a vessel which are conserved in their volume since they cannot escape. Mixing them, e.g. by shaking the vessel, increases the gradient between these substances while a well-separated state minimizes it. Diffusive terms strive towards such a phase-separation and punish gradients with an energy penalty.

Due to conservation, the substances cannot disappear but coarsen towards long-finite-wavelength patterns or full phase-separation. Since each plateau occurs equally in our SWs due to the antiperiodicity, the plateau values describe a conserved quantity.
Written pulses on SWs correspond to a mixed configuration of the plateau values, which is out of equilibrium. The system strives towards a fully state-separated square wave. If fronts possess tails, their interaction can create metastable states, where the tail acts as a potential barrier preventing coarsening. In this case, sufficiently big noise could push the fronts over these barriers.

4.5.1. Subcritical without Noise

It is convenient to start in the subcritical case since it generally features more tail due to the strong snaking structure. The parameter set has been taken from the branch in Fig. 4.16. Figure 4.18 and Fig. 4.19 show the time evolution of a thick pulse with width $w = \frac{\tau}{10}$ and a thin pulse with width $w = \frac{\tau}{30}$. By comparing the two figures, the noticeable difference is in the drift speed of the pulses. The two pulses seem to experience different drifting speeds due to their different width.
When the thinner pulse in Fig. 4.19 comes close to another front, the tail-induced potential and the resulting preferred distances can be seen in the pulse's irregular faltering motion. Also the asymmetric tail itself can be seen as stripes above each front. It is impossible to say if the thicker pulse is stationary or drifting on a very slow time scale. In any case, the behavior of Fig. 4.19 shows, how fronts can interact and that certain bound states are probably stable. To further investigate this question, one can induce noise.

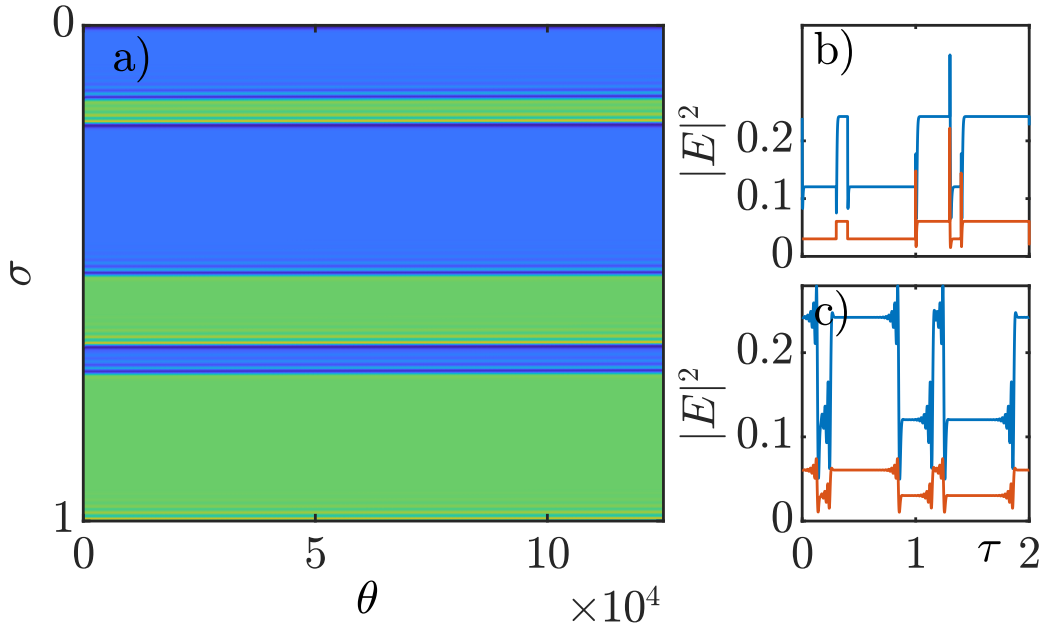

Figure 4.18: Space-time diagram showing the dynamics of a thicker peak with width $w = \frac{\tau}{10}$ and without noise in the subcritical regime. One can see the asymmetric tail as weaker stripes above each front. The pulse appears to be stationary, at least on this time scale. b) The simulation's solution of length 2τ after one roundtrip. c) The final 2τ solution. (b,c) will show these two for all of the following space-time diagrams.

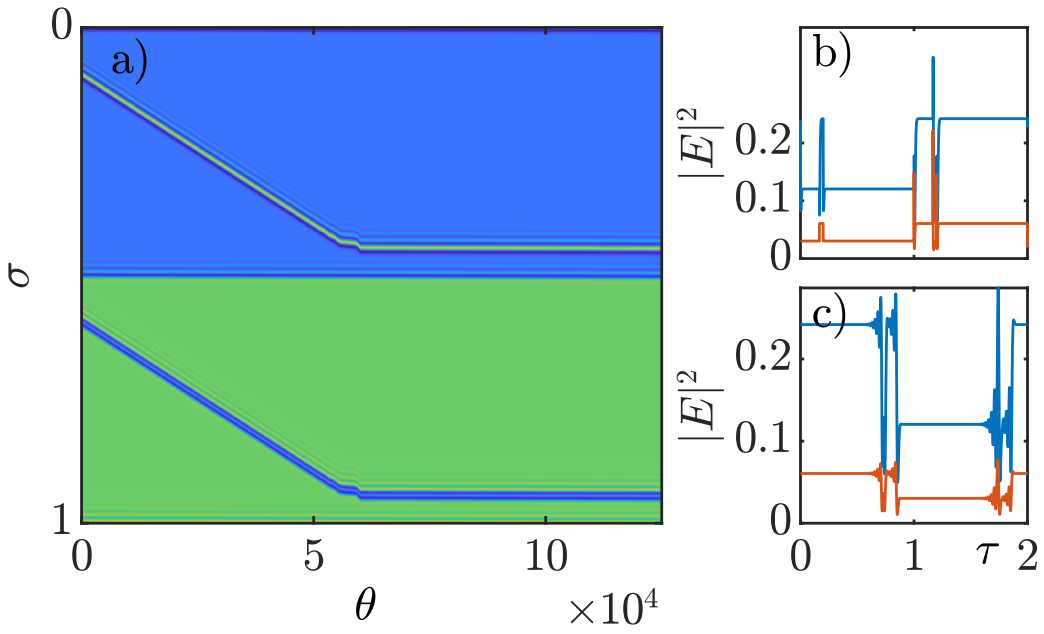

Figure 4.19: Space-time diagram showing the dynamics of a thinner peak with width $w = \frac{\tau}{30}$ and without noise in a subcritical regime. The pulse drifts towards the next front, where the tail induced potential leads to a irregular faltering motion and ultimately to a favorable configuration of the pulses.

4.5.2. Subcritical with Noise

The introduction of additive Gaussian white noise allows investigating the stability of the found states against small perturbations. In Fig. 4.20 and Fig. 4.21, one can see the time evolution of the same two initial conditions as before, but this time they get perturbed. In (b,c) a good impression of the noise's order of magnitude is given. It is not strong enough to surpass any fronts but in a similar order of magnitude as the tail, which should weaken the interaction. By comparing the two figures, one can see that the thicker pulse's fronts separate and drift around independently since their interaction is too weak, while the fronts of the thinner pulse stay bound. Nevertheless, the fronts are an insurmountable potential barrier for each other preventing full coarsening. Although the noise can be increased in amplitude until the bound states break down, these results demonstrate certain structural stability of the written pulses.

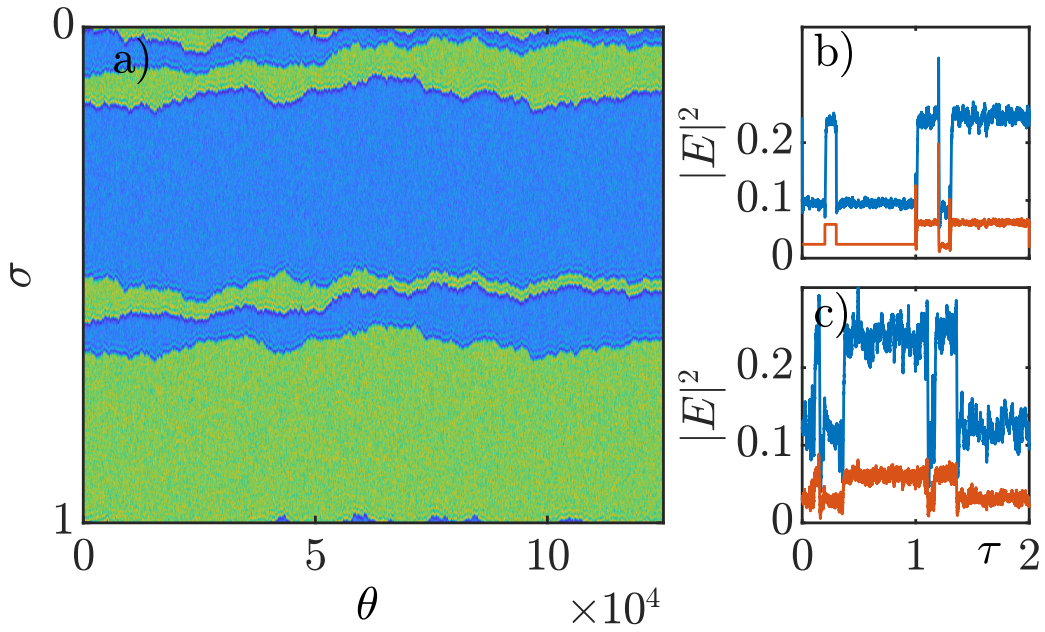

Figure 4.20: Dynamics of a thicker peak with $w = \frac{\tau}{10}$ in the subcritical regime, where Gaussian white-noise with amplitude 0.008 has been introduced. Further separated fronts that are more weakly bound tend to drift around. When two fronts get close enough, they tend to form bound states and drift together.

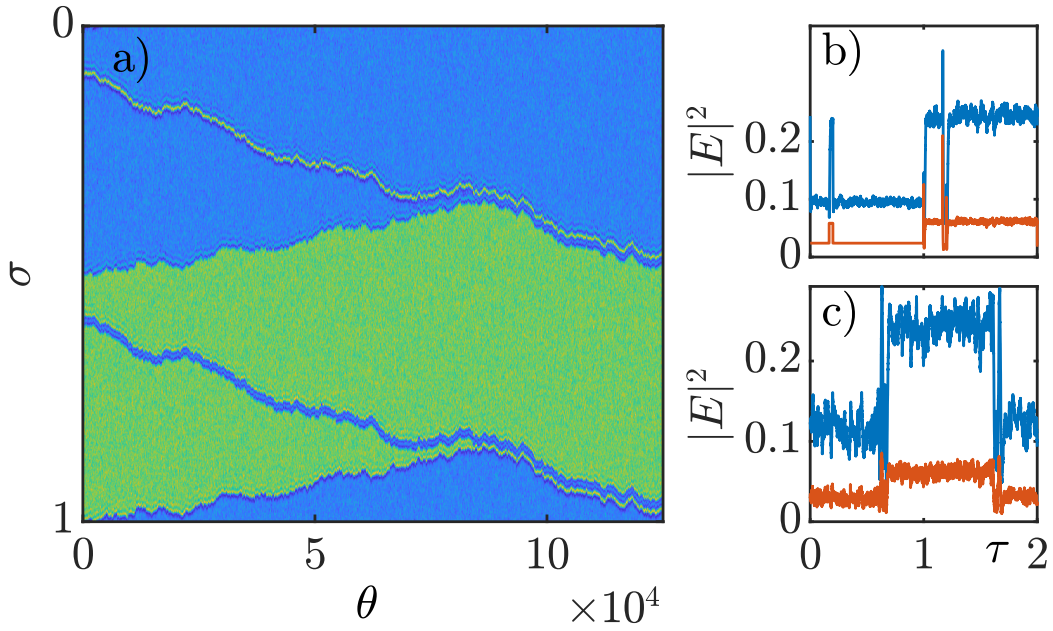

Figure 4.21: Dynamics of a thinner peak with $w = \frac{\tau}{30}$ in the subcritical regime, where Gaussian white-noise with amplitude 0.008 has been introduced. The noise is neither strong enough to break apart the bound state of the two fronts, nor to let them annihilate, which would lead to full coarsening.

4.5.3. Supercritical without Noise

Now the supercritical case shall be investigated, naturally showing less tail. Following the argumentation from the last sections, bound states with written pulses should be less stable. Fig. 4.22 shows the same pulse of width $w = \frac{\tau}{10}$, which first shrinks in width and then drifts upwards and collides with the next front. This looks like an elastic collision, where the joined fronts drift slower due to their increased mass.
All in all, the plot suggests that the supercritical case shows a single stable distance of fronts in agreement with the observation observation that the profile in Fig. 4.1 shows little tail consisting of only a single notable peak. The observation is supported by Fig. 4.23, with the thin pulse, which was stable for the subcritical case. Here, however, the fronts collapse since they are too close together, resulting in full coarsening.

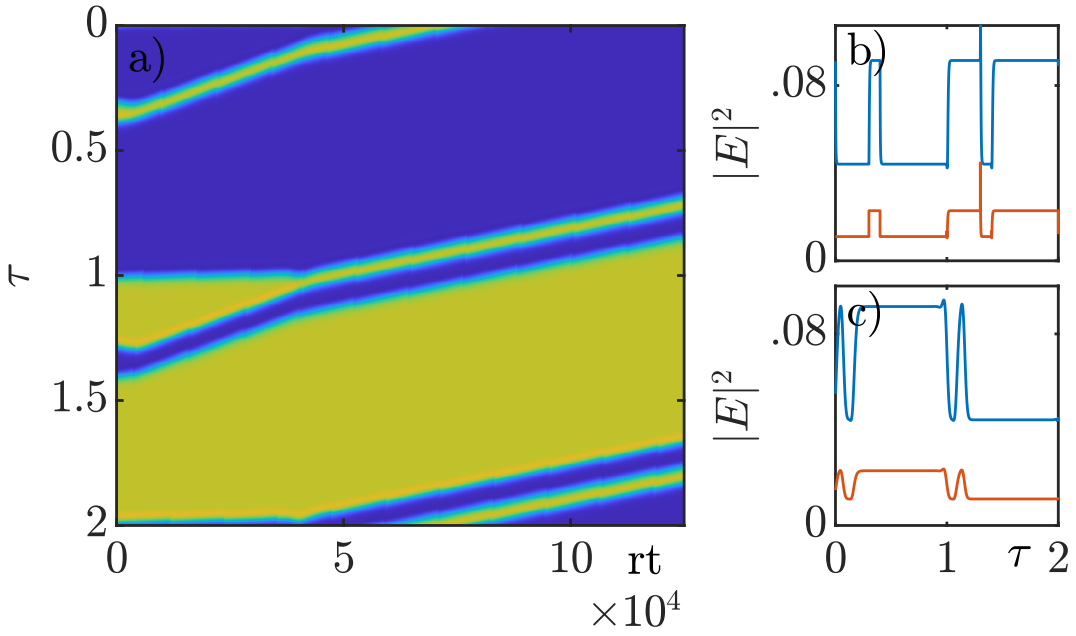

Figure 4.22: Dynamics of the thicker pulse $w = \frac{\tau}{10}$ in the supercritical regime, without noise. Within the first roundtrips, the pulse becomes thinner, entering an assumable more favorable configuration. It then drifts towards the next front. In the following collision it transfers a part of it's momentum onto the front.

4.5.4. Supercritical with Noise

Finally, the supercritical case with noise, seen in Fig. 4.24, has to be considered. For this figure, weaker noise has been used, than in the subcritical case, because otherwise, the system would show an almost instant full coarsening. In this way, however, the interaction can still be observed when fronts move together for some time, but ultimately the system still coarsens. The behavior of fronts and pulses in the super- and subcritical case with and without noise has been analyzed successfully. Especially in the subcritical case, the bound states of fronts showed a certain robustness against perturbations due to the tail-induced interaction.

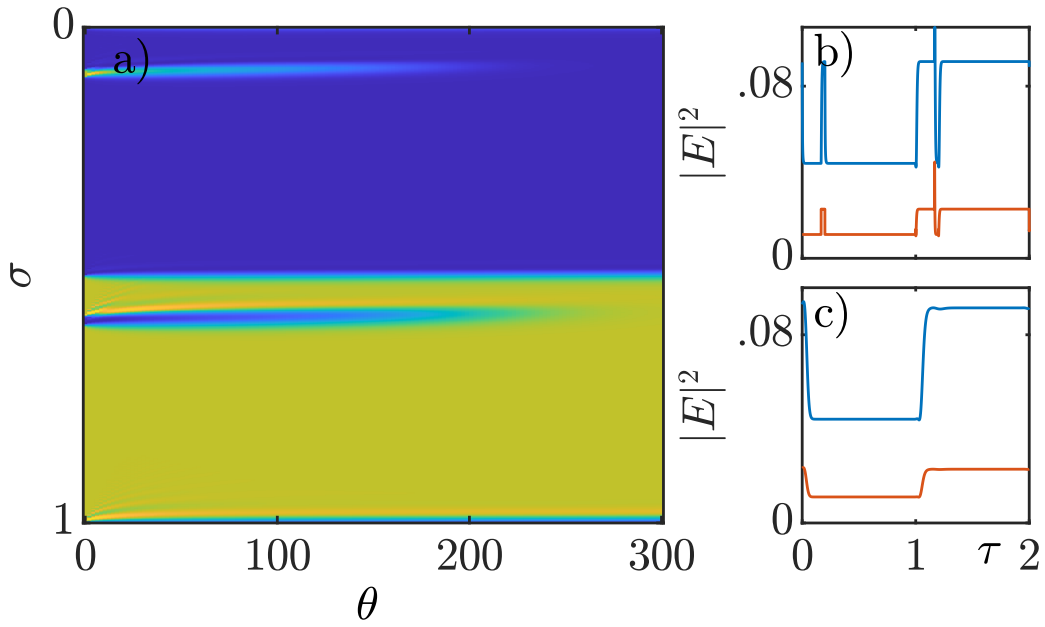

Figure 4.23: The thinner pulse with width $w = \frac{\tau}{30}$ collapses in the supercritical regime after only a few roundtrips, which leads to full coarsening.

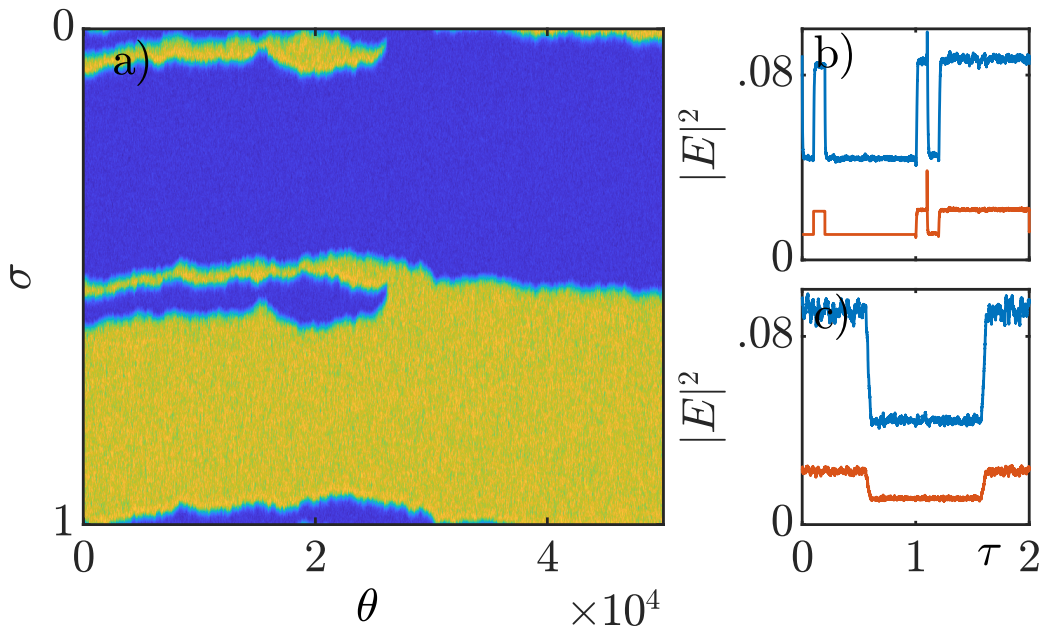

Figure 4.24: Dynamics of the stable pulse with width $w = \frac{\tau}{10}$ in the supercritical regime with Gaussian white-noise with amplitude 0.001. Due to the weak tail induced interactions the fronts annihilate at some point, when they come too close to each other.

5. Pulsating Dynamics in an Injected Quantum Well Gires-Tournois Interferometer

In this section a new system will be introduced consisting of a Fabry-Perot microcavity, as before, with a quantum well instead of a Kerr medium. Hence, this system will be called a quantum well Gires-Tournois interferometer (QGTI). Except for the nonlinearity, the setup stays the same. For its description the already mentioned quantum well susceptibility [Bal98] is used, which reads

$$\chi(u, D) = \frac{1}{\pi} \left[\ln(u + i - b) - 2 \ln(u + i - D) + \ln(u + i) - \ln(b) \right]. \tag{5.1}$$

The susceptibility describes the medium's response if incoming light with frequency ω hits the medium. In general, susceptibility describes a receptivity, here the ability to absorb photons via excitation. Thus, the response depends on the time-dependent carrier density. If, e.g., all carriers are excited, no light can be absorbed. The new variable $D = \frac{\mathcal{N}}{\mathcal{N}_t}$ is the carrier density, normalized with respect to the transparency level at the band gap. So $D = 0$ would describe an empty conduction band, $D = 0.3$ would describe a small inversion, and $D = 1$ describes transparency at the bandgap $u = 0$. u is the frequency ω, corrected by the band gap frequency ω_G as $u = \frac{\omega - \omega_G}{\gamma_\perp}$, where $\gamma_\perp$ is the intraband polarization dephasing rate. b is the top-band frequency ω_T, corrected the same way as u to $b = \frac{\omega_T - \omega_G}{\gamma_\perp}$. Normally the band gap ω_G is assumed to be small compared to ω_T.
The imaginary part of χ describes the absorption, while the real part describes a phase shift, hence a refraction index. Here small values of D corresponding to a vanishing carrier density are considered. A negative u (frequency smaller than the band gap) corresponds to almost no absorption and the imaginary part is zero. For a positive u, however, the absorption goes towards one. The gain is defined as the negative imaginary part, so the negative absorption. The real- and imaginary part of the susceptibility for $D = 0$ and $D = 0.3$ can be seen in Fig. 5.1 The resulting system is

$$\dot{E}(t) = \left[if\chi - 1 - i\delta \right] E(t) + hY(t), \tag{5.2}$$

$$\dot{D}(t) = \gamma \left[-D(t) + \Im(\chi)|E|^2 \right], \tag{5.3}$$

$$Y(t) = \eta e^{i\varphi} \left[E(t - \tau) - Y(t - \tau) \right] + Y_0 \sqrt{1 - \eta^2}, \tag{5.4}$$

which is a DAE system. The resulting new first order differential equation for D is a transcendental equation, due to D appearing in the susceptibility χ.
In order to compare the new system with the KGTI system the system will be treated in long-delay limit. Here a problem arises with the delay and the scaled carrier lifetime γ. Despite the missleading name, γ can be considered a decay frequency since small values of γ correspond to long living excitations. For small values, such as $\gamma \approx 10^{-3}$, a new large decay time scale is introduced, which is proportional to γ^{-1}. Thus, even larger delays have to be chosen in order to fulfill $\gamma\tau \gg 1$ and stay in the long-delay limit, which, however, may cause numerical inconveniences.

5.1. Comparing the System to the KGTI

The analysis of the QGTI system is started by looking for pulses, since they can be easily recognized by the bistable CW region. To find pulses by using results from the KGTI system it seems reasonable to find approximations in which the systems agree and choose

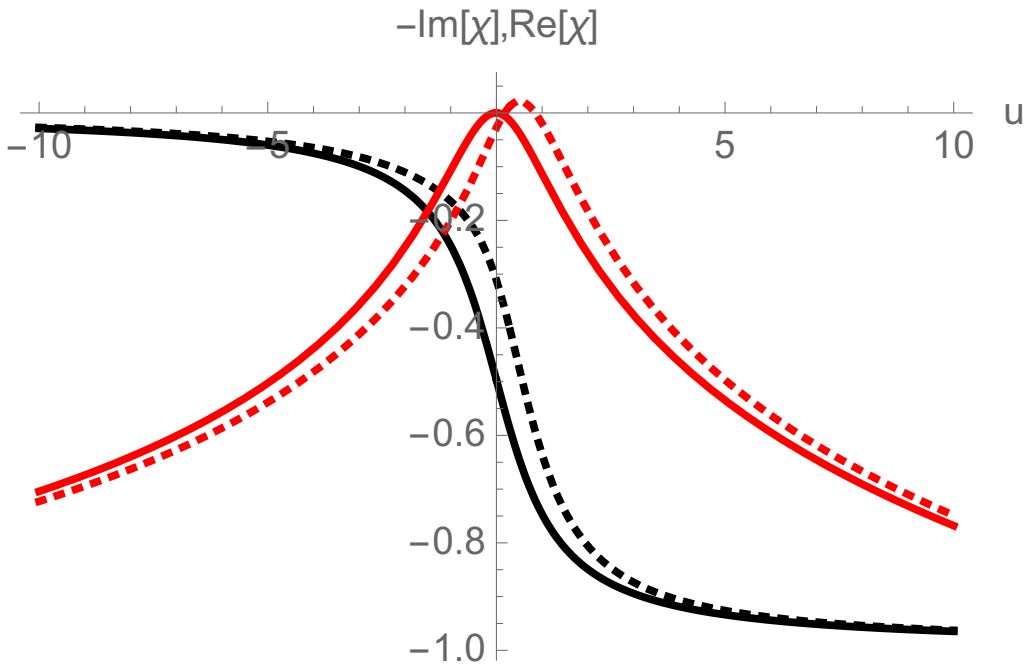

Figure 5.1: The real (red) and negative imaginary (black) part of the susceptibility $\chi(u, D)$, for $D = 0$ (full line) and $D = 0.3$ (dotted lines) with $b = 100$. .

the parameter according to possible shifts or rescalings. In a perfect scenario it would be possible to find a transformation between the two systems. Hence, this section aims at transforming the QGTI system into the KGTI system. For the KGTI the nonlinearity contains only the Kerr effect arising from the second order of the refractive index. As mentioned before the refractive index results from $\Re(\chi(u, D))$. Since $\Re(\chi(u, D))$ is large for large negative u while the absorption from the imaginary part is small as shown in Fig. 5.1 $u \ll 0$ appears to be a good choice for a parameter regime where the novel system might approach the KGTI. $b \gg 0$ corresponds to a large band which can be used since it simplifies the equations while not influencing the results in a relevant way. Since we are in a regime of small absorption $\chi(u, D)$ is approximated with a Taylor expansion for small D where the quadratic term from the refractive index $|E|^2$ and thus Kerr effect is dominant. $b \gg 0$ and $u \ll 0$ are used as well, where the latter assumption allows for a Taylor expansion of $\ln(1 + \frac{i}{u})$ around $\frac{i}{u} = x = 0$. Then, terms of order $\frac{1}{u^2}$ are dropped leading to the simplified susceptibility

$$\chi = \frac{-1}{\pi}\left[\ln(-u) + \frac{i - 2D}{u}\right]. \tag{5.5}$$

There will be no further approximations for the moment. So a solution for this simplified susceptibility should also exist for the full QGTI system within the proper parameter regions. Inserting this simplified susceptibility into the system equations (5.2) - (5.4) for

the QGTI system, yields

$$\dot{E} = \left[-i\frac{2f}{-u\pi}D - 1 - \frac{f}{-u\pi} - i\left(\delta + \frac{f}{\pi}ln(-u)\right)\right]E + hY, \tag{5.6}$$

$$\dot{D} = \gamma\left(-D + \frac{1}{-u\pi}|E|^2\right), \tag{5.7}$$

$$Y = \eta e^{i\varphi}\left[E(t-\tau) - Y(t-\tau)\right] + Y_0\sqrt{1-|\eta|^2}, \tag{5.8}$$

which will be labeled the approximated QGTI (aQGTI) for reasons of distinction. Now, the second equation, Eq. (5.7) can be multiplied by $\frac{2f}{-u\pi}$, revealing the natural rescalings

$$\tilde{D} = \frac{2f}{-u\pi}D, \tag{5.9}$$

$$\tilde{E} = \frac{\sqrt{2f}}{-u\pi}E. \tag{5.10}$$

The other equations can be multiplied by $\frac{\sqrt{2f}}{-u\pi}$, revealing the same scaling for Y_0 and Y. This unravels a shift in the injection regimes, where bistability can be expected. For δ as well the shift

$$\tilde{\delta} = \delta + \frac{f}{\pi}ln(-u) \tag{5.11}$$

can be found, defining an approximated and rescaled model for the QGTI (arQGTI) system as

$$\dot{\tilde{E}} = \left[-i\tilde{D} - 1 + \frac{f}{u\pi} - i\tilde{\delta}\right]\tilde{E} + h\tilde{Y}, \tag{5.12}$$

$$\dot{\tilde{D}} = \gamma\left(-\tilde{D} + |\tilde{E}|^2\right), \tag{5.13}$$

$$\tilde{Y} = \eta e^{i\varphi}\left[\tilde{E}(t-\tau) - \tilde{Y}(t-\tau)\right] + \tilde{Y}_0\sqrt{1-|\eta|^2}. \tag{5.14}$$

Within an adiabatic elimination of the $\dot{D}$ equation this system is similar to our KGTI system. It is to mention, that a CW state generally fulfills $\dot{D} = 0$. The only difference is the linear $\frac{f}{u\pi}\tilde{E}$ term, as well as the negative sign in front of $-\tilde{D}$. Since the first goal is a search for bistable regimes the CW solution has to be calculated with $\dot{E} = \dot{Y} = 0$, leading to

$$|\tilde{E}|^2 = \left|\frac{hY_0}{-i\tilde{D} - 1 - \alpha_i - i\tilde{\delta} + \frac{h\eta e^{i\varphi}}{1-\eta e^{i\varphi}}}\right|^2 \left|\frac{\sqrt{1-|\eta|^2|}}{1+\eta e^{i\varphi}}\right|^2, \tag{5.15}$$

$$\tilde{D} = |\tilde{E}|^2. \tag{5.16}$$

The switched sign of the $i\tilde{D}$ can be compensated by a negative δ, since the squared absolute value does only depend on the magnitude and not the sign of the imaginary part, and

$$-i\tilde{D} - i(-\tilde{\delta}) = (i\tilde{D} - i\tilde{\delta})^*. \tag{5.17}$$

Thus, a KGTI detuning $\tilde{\delta}_{\mathrm{KGTI}} = -\tilde{\delta}$ will transform to

$$\delta = -\tilde{\delta}_{\mathrm{KGTI}} - \frac{f}{\pi}\ln(-u). \tag{5.18}$$

Now these results can be applied by shifting a parameter set that is known for bistability in the KGTI, using the derived transformations. The example presented here is $\tilde{\delta}_{\mathrm{KGTI}} = 1.5$, $h = 2$, $\varphi = 0$ and $\eta = 0.5$, though a slightly higher $\eta = 0.9$ will be used. Pulses appear for these parameters at an injection of $0 < Y_0 < 2$. Up to this point the derivation does not restrict the choice of f, u, and b to fulfill the approximations that connect the two systems except for $u \ll -1$ and large b. However, for a large negative $u \ll -1$ or a very small f

$$D = \frac{-u\pi}{\sqrt{2f\tilde{D}}} \gg \tilde{D} \tag{5.19}$$

is found, which might cause problems since a used Taylor expansion demands small values of D for the arQGTI model to be valid. From a physical perspective large negative u and small positive f are preferred. However, to fulfill both approximations while still maintaining reasonable parameter regimes, a compromise has to be accepted. Here $u = -20$ and $f = 10$ will be used, leading to

$$D = 14.0496\tilde{D}, \tag{5.20}$$

which corresponds to a relatively large u while keeping a relatively small D. For bistable regimes in the KGTI at $0 < \tilde{Y_0} < 2$ the expected regime for bistability in the arQGTI is $0 < Y_0 \approx< 30$. Finally $\tilde{\delta}_{\mathrm{KGTI}} = 1.5$ corresponds to $\delta = -11.0357$. This parameter set is expected to show bistability in the QGTI system. The two remaining parameters γ and τ do not influence the form of the continuous wave state. They can be chosen later to form the periodic solutions.

5.1.1. Results

For the derived set of parameters, bistability is found in the expected range of injections Y_0. To ultimately get towards periodic solutions τ and γ have to be chosen wisely. For computation reasons, one can start with $\gamma = \frac{1}{10}$. To stay within the long-delay limit, which has already been $\tau = \mathcal{O}(10^2)$ before, the delay will be increased by one order of magnitude indicating $\tau = 1000$ as a reasonable choice.

The resulting bifurcation diagram can be seen in Fig. 5.2, where the bistable CW branch is shown, with two periodic solutions. The branch in red is the branch of pulses with a period of $T \approx \tau$, while the green branch has a period of $T \approx \frac{1}{8}\tau$. In the upper part of the inset, one can also see a section of stable pulses, which however lose stability between the folds due to a Torus bifurcation, that can be seen in Fig. 5.4, where a) and b) show the eigenvalues of a point right before and after the solution becomes stable.
In the lower saddle-node bifurcation SN_1 on the CW branch, one can observe another interesting behavior, where the short-wavelength solution becomes unstable first in H_1 while the real eigenvalue, resembling the saddle-node bifurcation, is the last to pass the imaginary axis. In the space-time picture this behavior can be identified with a Type-I instability in the Cross-Hohenberg classification [CH93], describing the pattern formation arising at a Turing bifurcation which can also be seen from the eigenvalue behavior in Fig. 5.5 a).
Meanwhile, at SN_2, the CW branch loses stability first in a saddle-node bifurcation, followed by the Hopf bifurcation that belongs to the branch with the longest finite period $T \approx \tau$. The affiliated eigenvalue structure can be seen in Fig. 5.5 b). Here the seemingly obvious correspondence to a Type-III instability fails, since the leading zero eigenvalue due to the SN bifurcation will not lead to constant growth. The eigenvalue

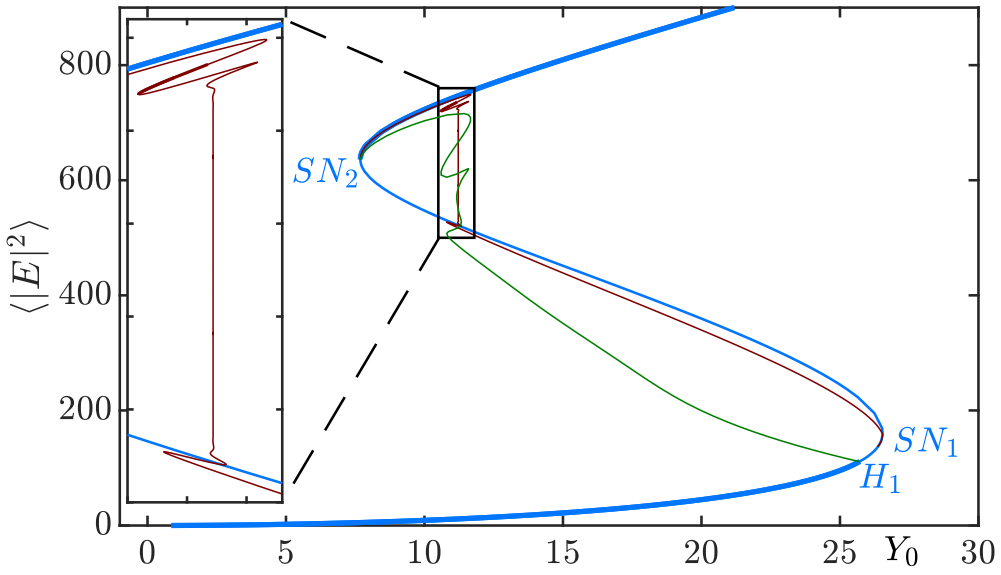

Figure 5.2: A bistable CW branch, featuring two branches of periodic solutions, with period $T \approx \tau$ (red) and $T \approx \frac{1}{8}\tau$ (green). The short wavelength instability H_1 happens before the lower saddle-node bifurcation SN_1, while the branch with the longest wavelength $T \approx \tau$ bifurcates at SN_1. Meanwhile, at SN_2, the long-finite-wavelength solution becomes unstable first. Parameters: $(\delta, h, \eta, \varphi, \tau, u, f, b, \gamma) = (-11.0357, 2, 0.9, 0, 1000, -20, 10, 1000, 0.1)$.

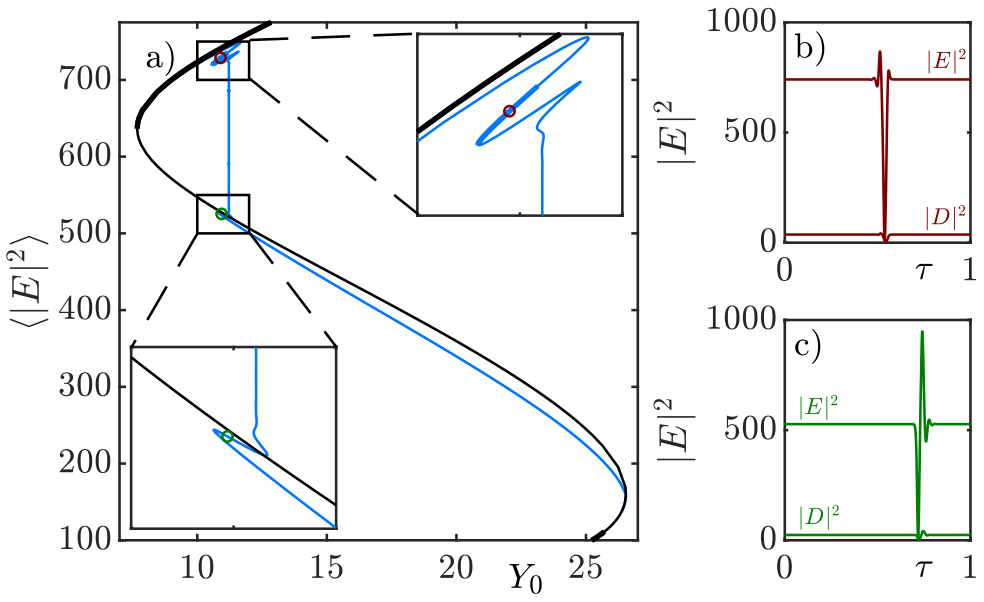

Figure 5.3: The $T \approx \tau$ branch from Fig. 5.2, with two profiles. b) shows a profile from the stable dark pulses in the upper snaking. Besides the squared electric field $|E|^2$ the carrier density D has been plotted here, to demonstrate that it is small compared to E. c) shows an unstable mixed state between a bright and dark pulse that appears in the lower snaking but is unstable. Parameters: $(\delta, h, \eta, \varphi, \tau, u, f, b, \gamma) = (-11.0357, 2, 0.9, 0, 1000, -20, 10, 1000, 0.1)$.

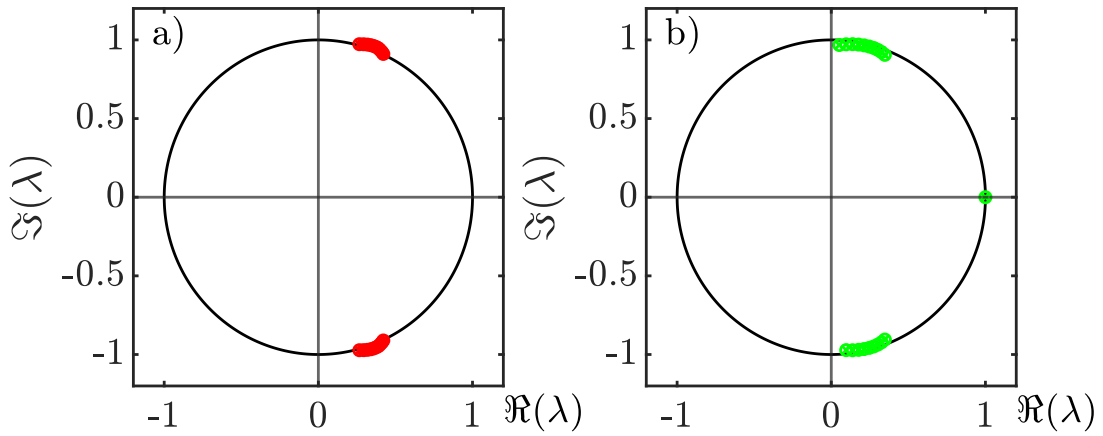

Figure 5.4: Eigenvalue behavior at the point where the dark pulse regime loses stability. The eigenvalues show a cascade of Torus bifurcations. The trivial eigenvalue $\lambda = 1$ cannot be seen in a) because only the first eigenvalues are shown. Parameters: $(\delta, h, \eta, \varphi, \tau, u, f, b, \gamma) = (-11.0357, 2, 0.9, 0, 1000, -20, 10, 1000, 0.1)$.

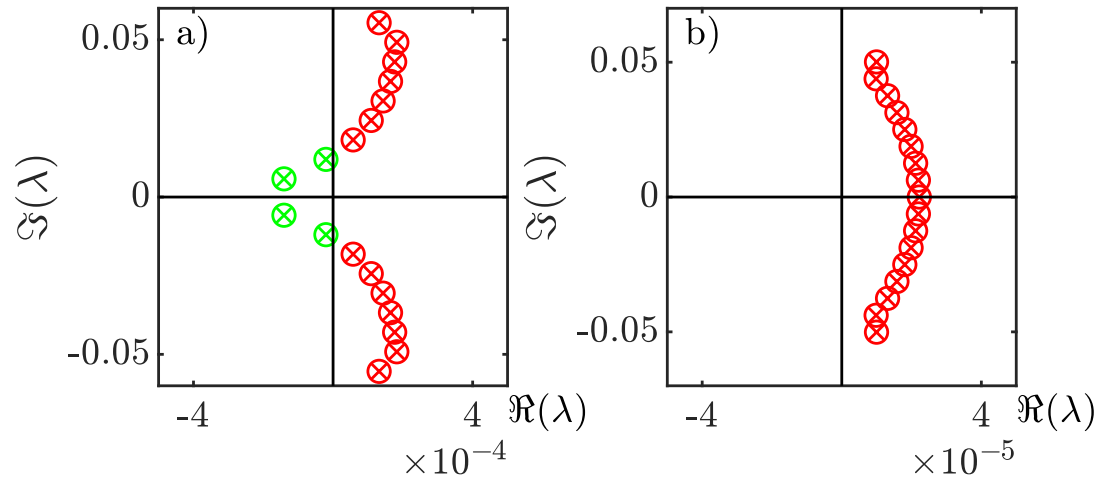

Figure 5.5: The eigenvalue behavior at the SN bifurcations of the CW branch in Fig. 5.2. a) shows the short-wave instability at the lower SN bifurcation while b) shows a long-finite-wavelength instability at the upper SN bifurcation. $(\delta, h, \eta, \varphi, \tau, u, f, b, \gamma) = (-11.0357, 2, 0.9, 0, 1000, -20, 10, 1000, 0.1)$.

structure is rather a long-finite-wavelength instability similar to the behavior found for SWs. However, the SWs did not show the real eigenvalue becoming unstable since the bifurcations did not occur at a SN bifurcation. In Fig. 5.3 one can see a few profiles from the periodic branch with $T \approx 1000$. The profile in b) comes from the stable region within the upper snaking, which shows a dark pulse with an asymmetric tail. The profile in c) shows a mixture of a dark and bright pulse, which also is not stable.

Finally, Fig. 5.6 shows a two-parameter continuation of the two major top folds, which

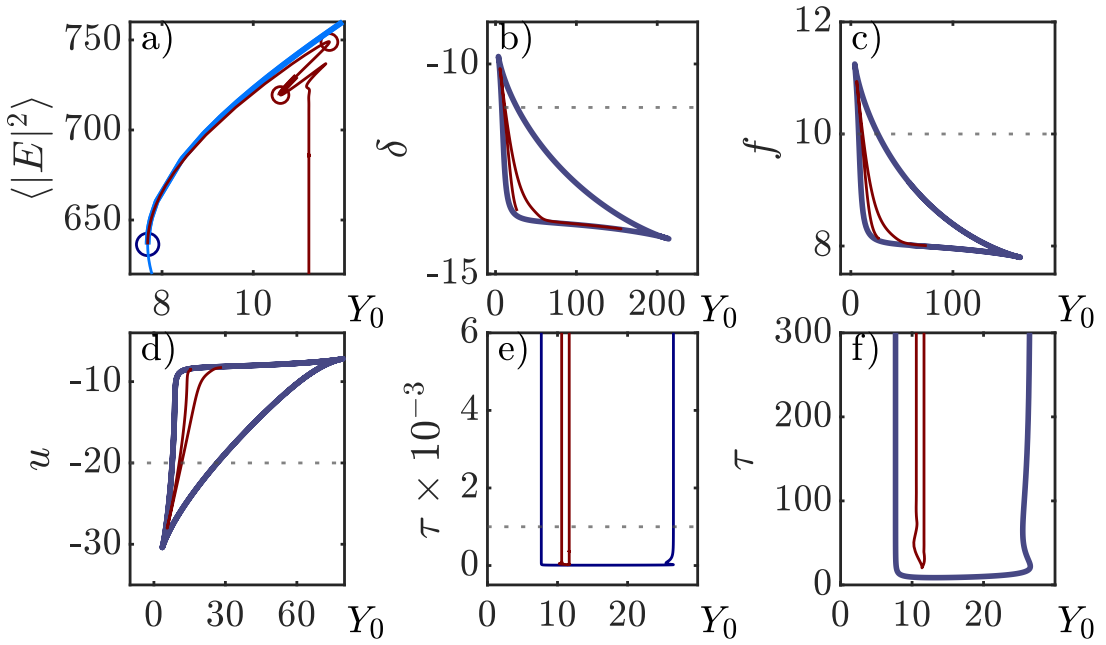

Figure 5.6: Two-parameter diagram of the two major folds in the dark pulse regime (red) and the Hopf bifurcations (blue) of the parameter set $(\delta, h, \eta, \varphi, \tau, u, f, b, \gamma) = (-11.0357, 2, 0.9, 0, 1000, -20, 10, 1000, 0.1)$, as shown in a). The starting parameter values are marked by the dotted lines. (e,f) to suggest, that long-delay limit is conserved. In b), e) and f) one can see that there is neither a regime where the regime of periodic solutions becomes larger, nor where it is more centered relative to the bistability.

feature stable pulses, and the Hopf bifurcations. Both are marked and color coded in a). The Hopf branches (blue) frame the region of bistability, that contain periodic solutions. Interestingly, b)-d) show that in most variables there is no way to increase the domain of periodic solutions, without increasing the bistable regime. (e,f) seem to indicate, that long-delay limit is contained, at least with regard to folding points positions that are approximately stationary down to low delays such as $\tau = 100$.

5.1.2. Looking at lower Delays

The general structure of periodic branches and locations of bifurcation points is robust against delay variations in long-delay limit. To further investigate this, lower delay values can be investigated explicitly. The CW solution cannot change its form, since it does not depend on τ, but bifurcation points on the CW branch can shift. This can be observed in Fig. 5.7, where the CW branch loses stability in a new bifurcation point B_n. Also, the periodic solution loses its stability everywhere, which shows that $\tau = 700$

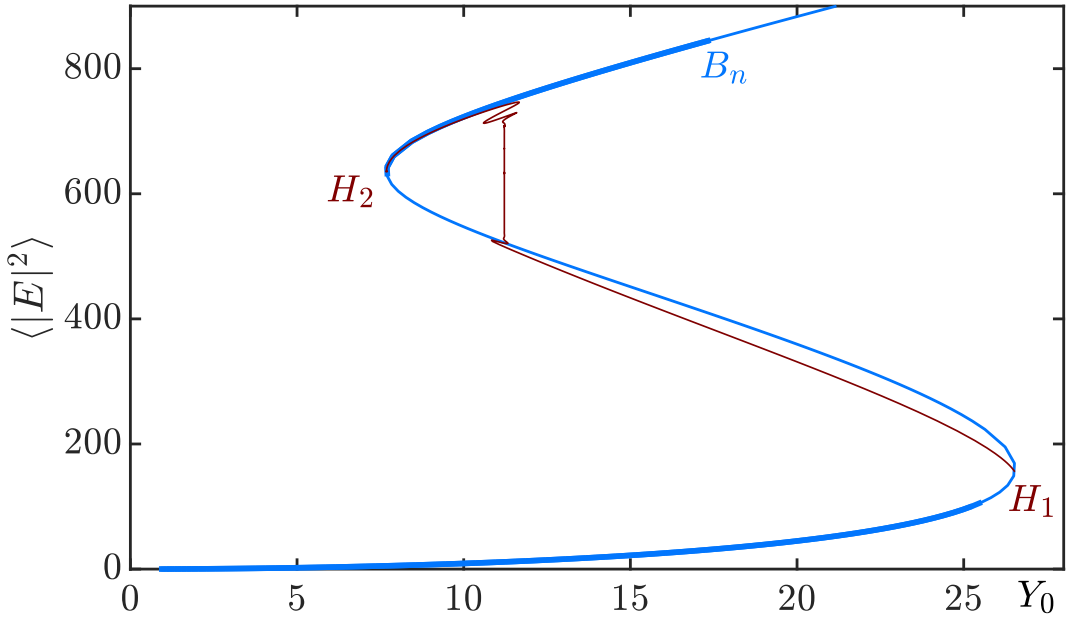

Figure 5.7: Only the delay has been decreased, leading to a new bifurcation point B_n, where the CW branch loses stability. Also, the periodic branch is unstable everywhere. Parameters: $(\delta, h, \eta, \varphi, \tau, u, f, b, \gamma) = (-11.0357, 2, 0.9, 0, 700, -20, 10, 1000, 0.1)$.

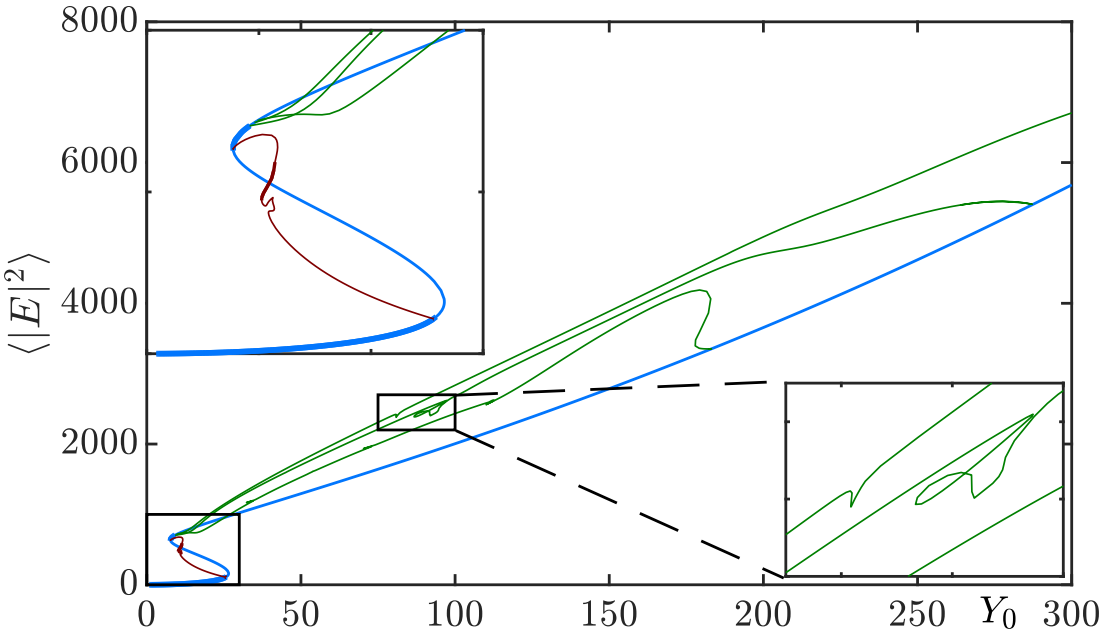

Figure 5.8: A very low delay leads to well separated eigenvalues, which allows to have a good look on the new instability B_n of the CW branch. The branches (green) emerge in a low-wavelength instability, similar to Fig. 5.5 a). They reconnect to the CW branch in an order, similar to the one in b). Parameters: $(\delta, h, \eta, \varphi, \tau, u, f, b, \gamma) = (-11.0357, 2, 0.9, 0, 50, -20, 10, 1000, 0.1)$.

is not in the long-delay limit for this set of parameters, although the folding points do not change their position as it has been shown in Fig. 5.6.
Figure 5.8 shows a bifurcation diagram for an even lower delay of $\tau = 50$. Here, the eigenvalues are well separated, allowing for a numerical path continuation of the solutions arising at the newly found bifurcations which led to the branches shown in (green). The eigenvalue behavior is similar to the one observed in the QGTI's bistable regimes, where branches with medium wavelength solutions arise first. When they bifurcate back on the CW branch, they reorder by wavelength. However, the bifurcation points are separated due to the long delay. Although there are more interesting observations to be made, this is not the main topic of this thesis so it will be dropped here.

5.2. Parameter Set for a Normal Form Limit

As mentioned in section 4, a normal form has been derived for the KGTI in a good cavity limit [SGJ22] corresponding to small cavity losses. To compare the systems, this thesis intends to derive a normal form in the same limit with $h = 2$ and $\eta \to 1$ presuming the necessity of existence of stable periodic solutions in that regime in the QGTI. Accepting the limitations in the possibility to approximate the new system with the KGTI which would have led to a very similar normal form in the according regimes of the new parameters u, f, γ and b the following section will discuss new promising choices of these parameters. A parameter set where bistability can be found is
$(\delta, h, \eta, \varphi, \gamma, f, u, b, \tau) = (-0.01, 2, 0.98, 0, 0.1, 1, 0.65, 1000, 1000)$. This set will be the starting point for optimizations regarding nice periodic solutions in the vicinity of a good cavity limit that could serve as expansion point for a normal form. The main difference to the last section is the choice of a small $u(\omega)$ which corresponds to an injection frequency ω that is close to the band gap. Figure 5.1 predicts a strong nonlinear response of the medium leading to the occurrence of a decent absorption (imaginary part) and refractive index (real part) likewise.

The chosen parameter set leads to a branch, which can be seen in Fig. 5.9. The two profiles demonstrate that this branch possesses stable bright and stable dark pulses, whereby the regime of dark pulses is shifted to lower injections and not centered around the Maxwell line. To improve understanding of the behavior of solutions in this parameter regime a two-parameter continuation is carried out whose results are presented in Fig. 5.10.
As before in two-parameter diagrams, the dotted grey lines mark the starting parameter set from Fig. 5.9. This time, the major folds of the stable bright and dark pulses have been looked at. The resulting branches are plotted in a bright purple and dark red, respectively, while the SN bifurcations limiting the bistable regime are plotted in dark-blue for reference. The panels b), d), and e) demonstrate a very interesting switching dynamic, where the choice of the respective parameters δ, u and φ determines the occurrence of dark pulses, bright pulses, or both. The regimes of pulsed periodic solutions, however, are small in the overlapping domain.
The two parameters f and η influence the behavior in a different way: An increase of the parameter increases the size of bistability and the regime of periodic solutions. In order to get a small f, one would have to increase η as compensation.
Finally, a continuation in γ has been included. The dotted grey line is in a region where the regimes of dark and bright pulses are separated. A choice of $\gamma = 1$ already leads to a regime where bright and dark pulses extend over larger injection regimes. These results can now be used to optimize the bifurcation diagram by setting $\gamma = 1$ and decreasing f. The latter leads to a smaller regime of periodic solutions, which can be counteracted

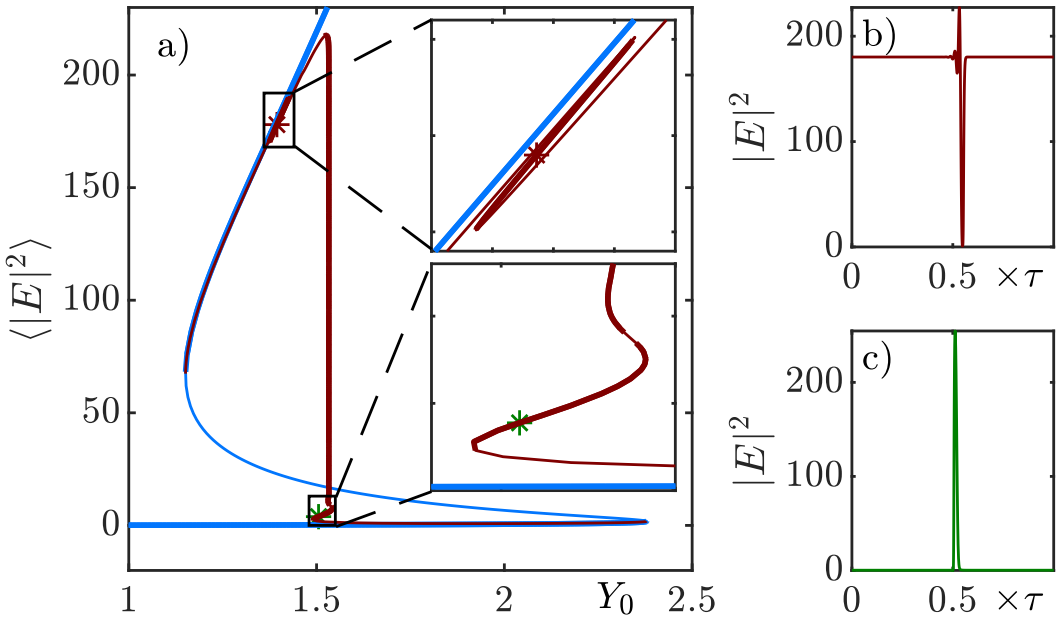

Figure 5.9: A periodic branch for the new parameter set with a small positive value of u. The branch features stable dark and bright pulses, which can be seen in b) and c), respectively. Parameters: $(\delta, h, \eta, \varphi, \gamma, f, u, b, \tau) = (-0.01, 2, 0.98, 0, 0.1, 1, 0.65, 1000, 1000)$.

by increasing η. Due to the increase in γ one can decrease τ as well to accelerate the numerical calculations.
Fig. 5.11 compares the behavior of the major folds limiting the range of stable light pulses in a two-parameter continuation of τ and γ, each over the injection, where one can see that a change of τ would not have the same influence on the dynamics as a change in γ, within this range of parameters.
The parameter set $\Omega_0 = (\delta, h, \eta, \varphi, \gamma, f, u, b, \tau) = (0.015, 2, 0.99, 0, 1, 0.2, 0.65, 1000, 250)$ leads to the bifurcation diagram that can be seen in Fig. 5.12. It features stable dark and bright pulses over an extended injection range. In a later section a normal form derivation in the vicinity of these solutions will be presented which is the reason why this point in the parameter space will be labeled Ω_0.

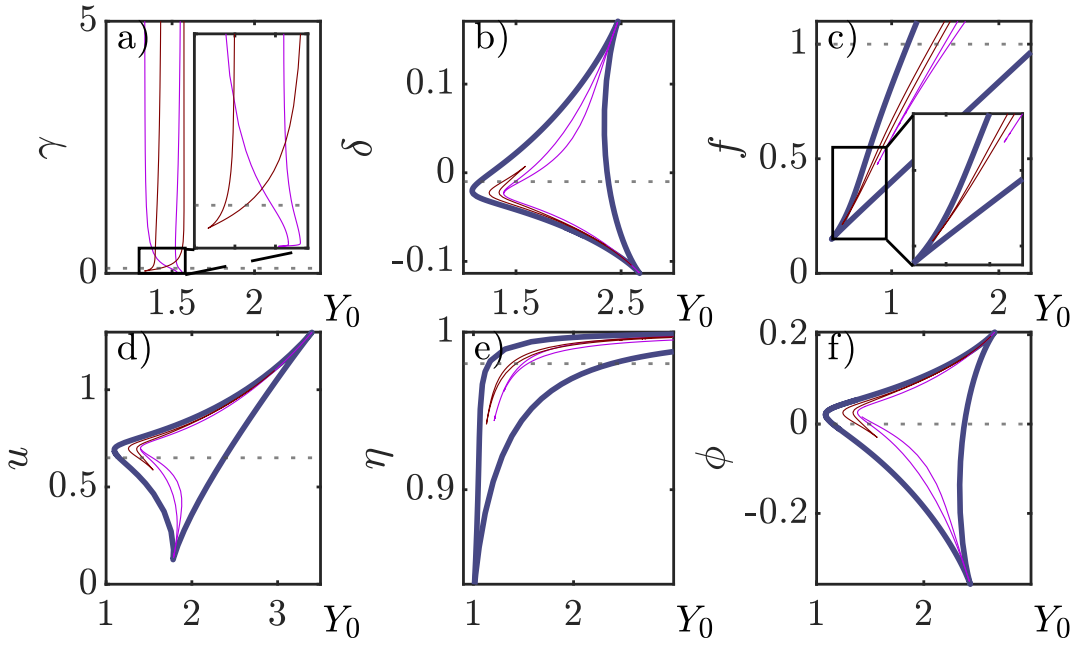

Figure 5.10: Two-parameter diagram for the parameter set $(\delta, h, \eta, \varphi, \gamma, f, u, b, \tau) = (-0.01, 2, 0.98, 0, 0.1, 1, 0.65, 1000, 1000)$ from Fig. 5.9. One can see the dark pulse (dark red) and bright pulse (bright purple) regimes, framed by the bistability (dark blue). a) demonstrates how the choice of γ influences the dynamics. b), d), and e) emphasize that the bright and dark pulse regimes are shifted relative to each other, with a small overlap section within the largest bistability regime. Increasing f and η both increase the bistability and pulse regimes .

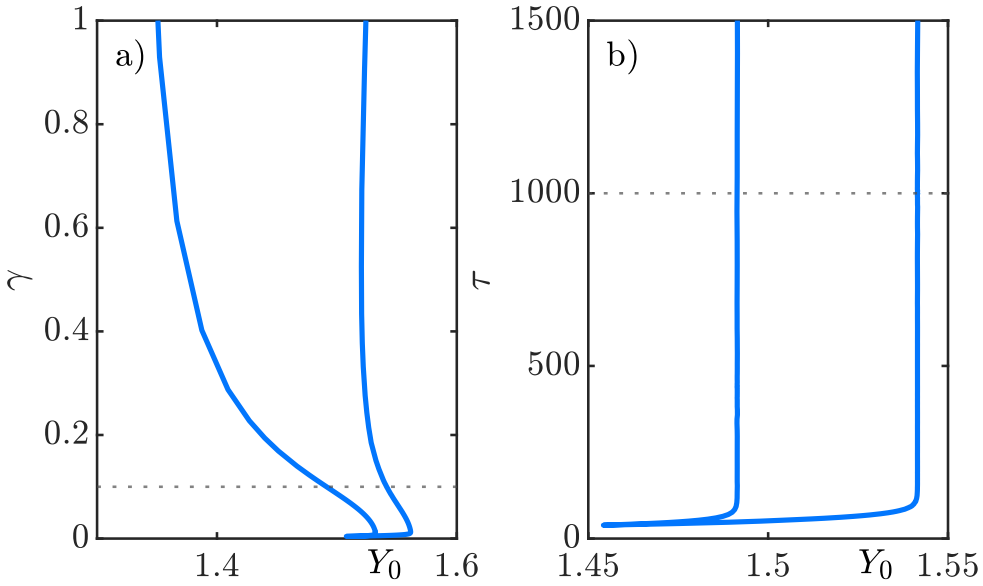

Figure 5.11: Comparing the two-parameter continuation for the bright-pulse regime of the (γ, Y_0) and (τ, Y_0) plane in a) and b), respectively, for the parameter set $(\delta, h, \eta, \varphi, \gamma, f, u, b, \tau) = (-0.01, 2, 0.98, 0, 0.1, 1, 0.65, 1000, 1000)$. One can see how even small changes of γ have a significant influence on the fold positions, while they seem to be robust against changes of τ in this regime.

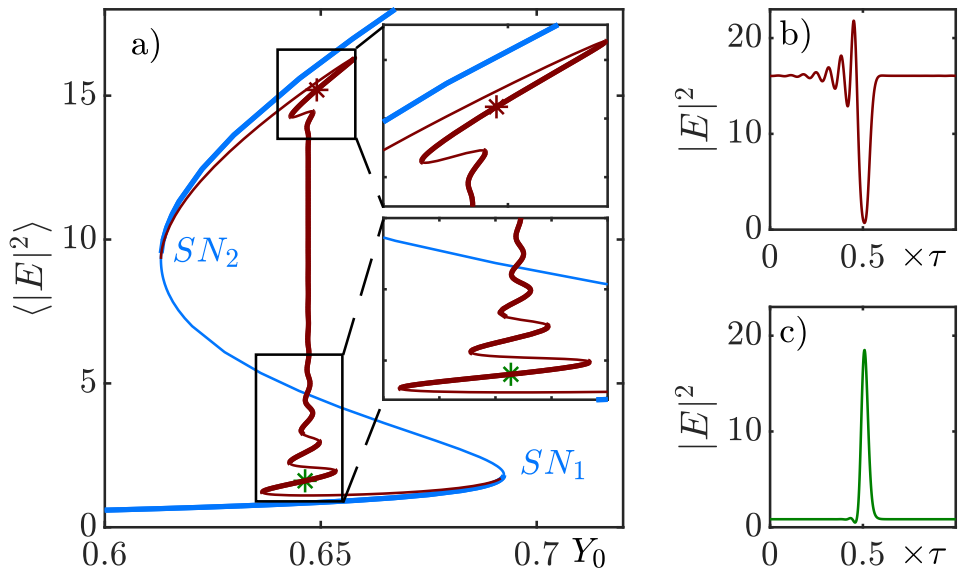

Figure 5.12: A branch featuring stable bright and dark pulses, with an increased value of γ and a reduced delay τ, as well as some slight parameter adjustments. The periodic branch is more symmetric and also the first periodic branch, bifurcating in the Hopf cascade at SN_1 and SN_2. The set of parameters $(\delta, h, \eta, \varphi, \gamma, f, u, b, \tau) = (0.015, 2, 0.99, 0, 1, 0.2, 0.65, 1000, 250)$ will be important for the next section and will be called Ω_0..

5.3. Square-waves in the QGTI

Empirically, SWs have often been found in similar regimes as the regular periodic solutions. The important difference is the phase φ, which needs to adjusted in order to get antiresonant feedback. Indeed, by setting $\varphi = \pi$, one can find SWs, as shown in Fig. 5.13.

The branch is similar in its appearance to the subcritical SW branches found in the

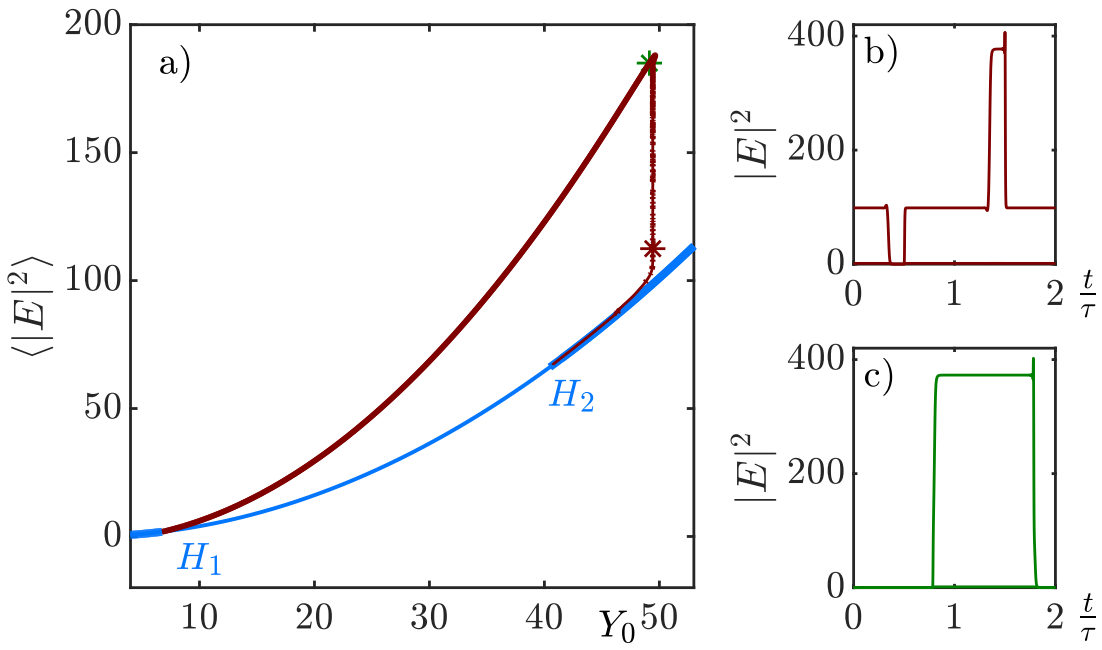

Figure 5.13: SWs, emerging in a supercritical Hopf bifurcation at H_1 and a subcritical Hopf bifurcation at H_2. Such a branch will be referred to as a subcritical SW branch of the QGTI. b) shows a solution with three plateaus at the Maxwell line, while c) shows a stable SW with 50% duty cycle. $(\delta, h, \eta, \varphi, \gamma, f, u, b, \tau) = (-0.01, 2, 0.98, \pi, 0.1, 1, 0.65, 1000, 1000)$.

KGTI. It features stable SWs with sharp transition layers on the back of the branch, as shown in c), and a behavior similar to the KGTI's along the Maxwell line is visible in b). However, the subcritical Hopf bifurcation is now the Hopf bifurcation H_2 at higher injections, so the branch seems to be flipped around. Also, the whole branch extends over a huge region of injection values. So a natural next step is to look at the two parameters that mainly control the width and injection domain of periodic branches, which are f and η. The resulting two-parameter diagrams, which show the positions of the Hopf bifurcation points H_1 and H_2, can be seen in Fig. 5.14.

Reducing either η or f decreases the width of the SW branch and shifts it to lower injection values. Especially the reduction of η can shift the whole branch below $Y_0 = 10$. However, the two parameters are not independent in a way that reducing the one limits the options of reducing the other. In both two-parameter diagrams, one can also see a folding point that reminds of the point P_0 found in Section 4.3, which marked the transition between subcritical and supercritical SWs.

Figure 5.15 shows this transition in η at the point $P_0 = (Y_0^c, \eta^c) = (3.300, 0.865)$. The folding point labeled P_0 in Fig. 5.14 appears on the part of the branch that describes the position of the Hopf bifurcation H_1 while the transition from subcritical to supercritical

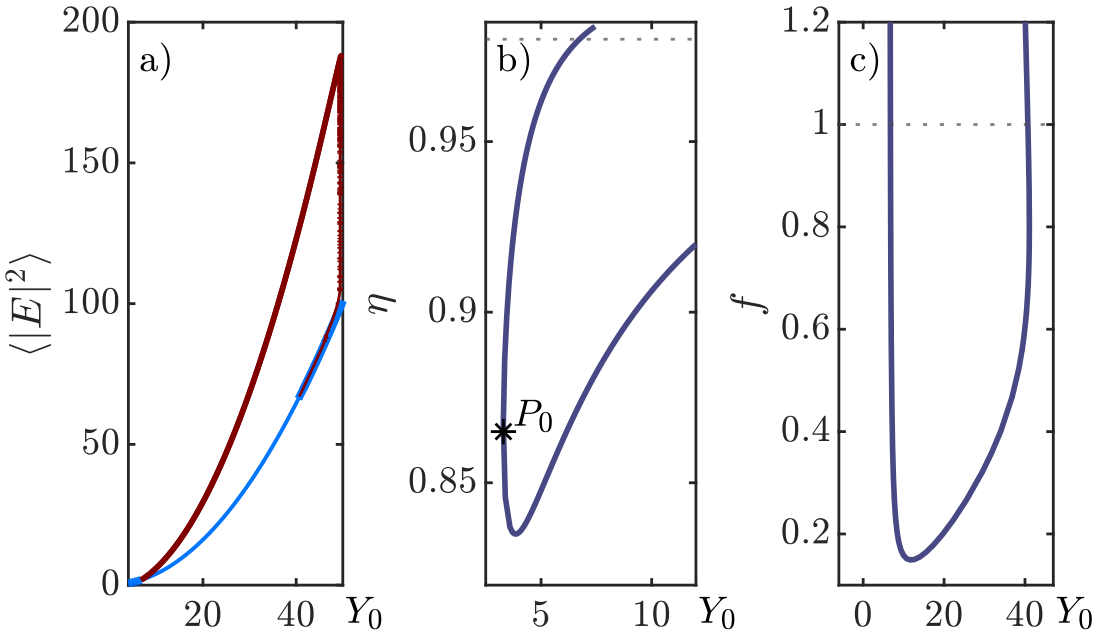

Figure 5.14: Two-parameter continuation of the Hopf points, belonging to the subcritical SW branch from a). b) shows the (η, Y_0) plane, featuring a folding point P_0. c) shows the (f, Y_0) plane. Both diagrams indicate that SWs exist at lower injections if η or f are decreased. Parameters: $(\delta, h, \eta, \varphi, \gamma, f, u, b, \tau) = (-0.01, 2, 0.98, \pi, 0.1, 1, 0.65, 1000, 1000)$.

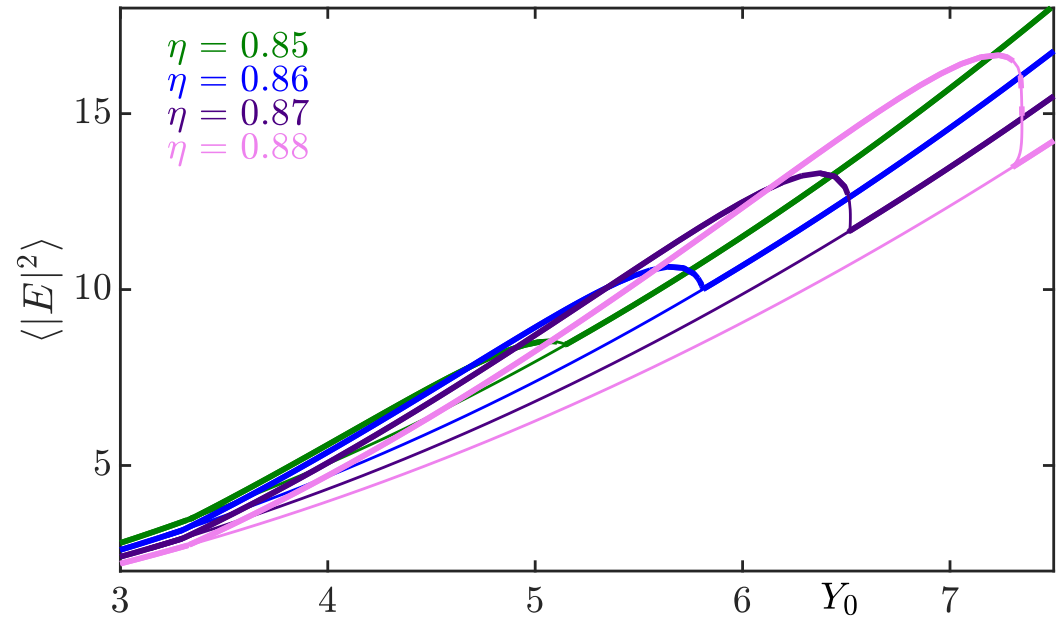

Figure 5.15: Several SW branches, showing the transition from subcritical to supercritical case around the folding point P_0 from Fig. 5.14. Parameters: $(\delta, h, \varphi, \gamma, f, u, b, \tau) = (-0.01, 2, \pi, 0.1, 1, 0.65, 1000, 1000)$.

takes place at the other Hopf H_2. The exemplary bifurcation diagram for $\eta = 0.86$ is shown in Fig. 5.16, where c) displays the same type of SW growth observed in the KGTI. The branch is fully stable showing sinus-alike periodic solution in the vicinity of its onset in panel c) that transform into fully developed SWs with sharp transition layers as shown in panel b).
Finally, Fig. 5.17 shows the associated two-parameter diagram of the Hopf points, where the grey lines mark the starting parameter set. In f and η a similar behavior is observed as for the subcritical case. Increasing these parameters leads to a growing regime of SWs, though this does not say anything about their stabiliy. The other parameters define limited regimes, where SWs exist. Here, especially the behavior in δ differs from the behavior observed for the KGTI in Section 4.3, where the two-parameter continuations of he Hopf bifurcations in the (Y_0, δ) plane looked similar to the Hopf branches for η and f that are observed in Fig. 5.17. However, one has to keep in mind that the relations derived in Section 5.1 for the transformation between the systems show an f dependence in the transformation of δ.

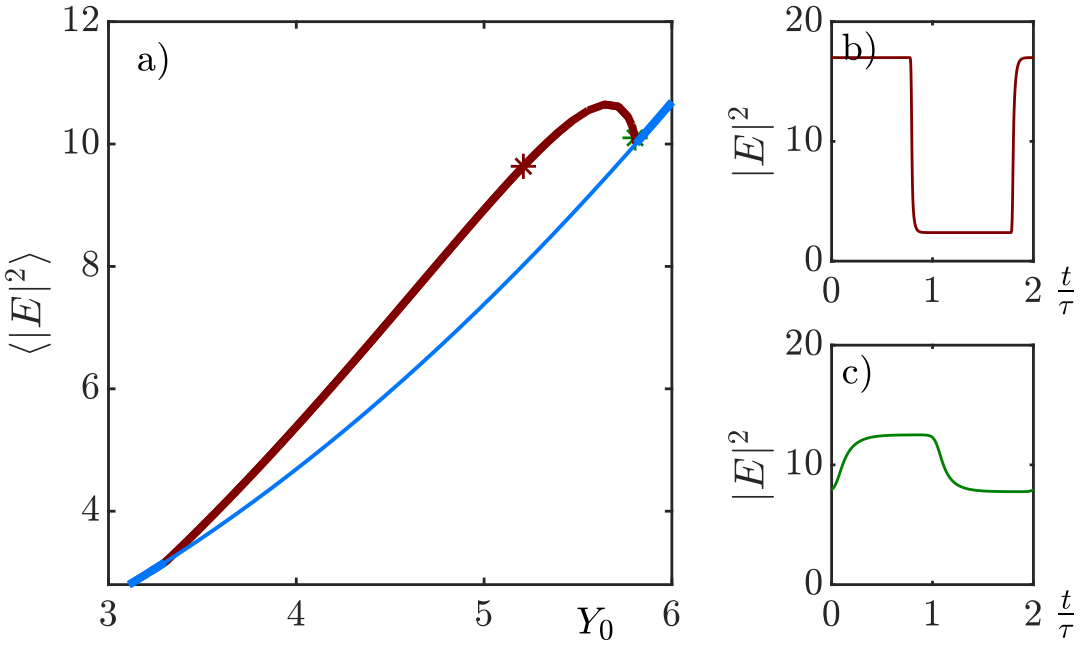

Figure 5.16: An exemplary branch for the supercritical regime, close to the transition at P_0. The two profiles in b) and c) show a stable as well as a just emerging SW, respectively. Parameters: $(\delta, h, \eta, \varphi, \gamma, f, u, b, \tau) = (-0.01, 2, 0.86, \pi, 0.1, 1, 0.65, 1000, 1000)$.

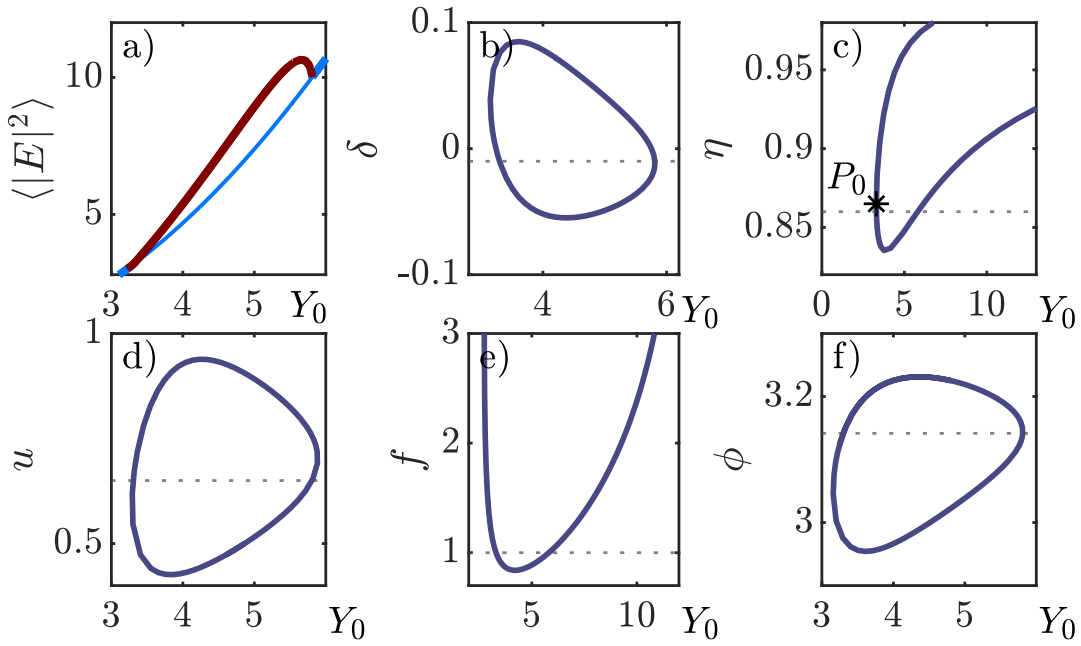

Figure 5.17: Two-parameter continuation of the Hopf points, where the SW branch from Fig. 5.16 emerges. Parameters: $(\delta, h, \eta, \varphi, \gamma, f, u, b, \tau) = (-0.01, 2, 0.86, \pi, 0.1, 1, 0.65, 1000, 1000)$.

6. Deriving a Normal Form in a Good Cavity Limit

6.1. Normal Form Settings

In the last section, dark and bright temporal localized states (TLSs) have been found in a good cavity limit represented by choosing $\eta \to 1$ and $h = 2$, especially in the vicinity of the point Ω_0 in parameter space that was introduced in Section 5.2. The high η leads to very small external cavity losses, hence a strong feedback. This represents a good expansion point for a weakly nonlinear analysis leading to a normal form which is done in this section for the QGTI system and can be compared to the one derived in [SGJ22] for the KGTI in the same limit. The resulting system of partial differential equations (PDEs) can help to get a better understanding on how the parameters influence the dynamics of TLSs in the QGTI. The system reads

$$\dot{E}(t) = [if\chi - 1 - i\delta]\, E(t) + hY(t), \tag{6.1}$$

$$\dot{D}(t) = \gamma \left[-D(t) + \Im(\chi)|E|^2\right], \tag{6.2}$$

$$Y(t) = \eta e^{i\varphi} \left[E(t-\tau) - Y(t-\tau)\right] + Y_0\sqrt{1-\eta^2}. \tag{6.3}$$

with

$$\chi(u, D) = \frac{1}{\pi}\left(\ln(u + i - b) - 2\ln(u + i - D) + \ln(u + i) - \ln(b)\right). \tag{6.4}$$

From now on $\varphi = 0$ will be used. Going from a DAE to a neutral delay differential equation (NDDE) allows to eliminate $Y(t)$. This can be achieved by adding Eq. (6.1) at time t onto itself at time $t - \tau$, multiplied by η. One can then recognize and insert Eq. (6.3), which eliminates $Y(t)$ and leads to

$$\begin{aligned}\left(\dot{E}(t) + \eta\dot{E}(t-\tau)\right) =& [if\chi(D(t)) - 1 - i\delta]\, E(t) + \eta\, [if\chi(D(t-1)) - 1 - i\delta]\, E(t-\tau) \\ &+ h\eta E(t-\tau) + hY_0\sqrt{(1-\eta^2)}.\end{aligned} \tag{6.5}$$

6.1.1. Time Scaling

First, the system is rescaled with $t \to \frac{t}{\tau}$ and $\frac{1}{\tau} = \epsilon$, yielding

$$\begin{aligned}\epsilon\left(\dot{E}(t) + \eta\dot{E}(t-1)\right) =& [if\chi(D(t)) - 1 - i\delta]\, E(t) + \eta\, [if\chi(D(t-1)) - 1 - i\delta]\, E(t-1) \\ &+ h\eta E(t-1) + hY_0\sqrt{(1-\eta^2)},\end{aligned} \tag{6.6}$$

$$\epsilon\dot{D} = \gamma\left[-D(t) + \Im(\chi(D))|E|^2\right]. \tag{6.7}$$

It now has a period of $T \approx 1$ defining the fastest timescale t_0. To avoid drift, the period T or equivalently the frequency ω can be expanded allowing for higher order corrections. This leads to a stretch in t_0:

$$t_0 = \omega t, \tag{6.8}$$

$$t_1 = 0, \tag{6.9}$$

$$t_2 = \epsilon^2 t, \tag{6.10}$$

$$t_3 = \epsilon^3 t. \tag{6.11}$$

6.1.2. Parameter Expansions

In the following, the parameters will be expanded based on the knowledge about the system as well as some practical thoughts:

$$Y_0 = \epsilon\gamma_1 + \epsilon^2\gamma_2 + \epsilon^3\gamma_3, \tag{6.12}$$

$$\eta = 1 + \eta^2\eta_2. \tag{6.13}$$

As mentioned before, the normal form is derived in a good cavity limit by choosing $\eta \to 1$ and $h = 2$ eliminating h from the equation. Furthermore, choosing Y_0 being $\mathcal{O}(\epsilon)$ combined with the choice of η leads to an injection that comes in at $\mathcal{O}(\epsilon^2)$. The detuning δ will not be expanded, nevertheless δ will be assumed to be small at some point of the derivation. The parameters u and b only appear within χ, hence they will not be considered for the moment. Finally, the major parameter to be discussed is f determining the strength of the nonlinearity.

6.1.3. Nonlinearity

In general the nonlinearity should enter at $\mathcal{O}(\epsilon^3)$ limiting nonlinear effects. The most obvious path is the choice $f = \mathcal{O}(\epsilon^3)$. In that case however, it appears to be hard to access the nonlinearity itself from the argument of χ. Another way is to choose f in a lower order such as $f \to \epsilon^2 f$ and rescale the field, as the following example will demonstrate. Consider $E \to \epsilon^{\frac{1}{2}}\mathcal{E}$, $Y \to \epsilon^{\frac{1}{2}}\mathcal{Y}$ and $Y_0 \to \epsilon^{\frac{1}{2}}\mathcal{Y}_0$. This leads to:

$$\epsilon\dot{D}(t) = \gamma\left[-D(t) + \epsilon\Im(\chi(D))|\mathcal{E}|^2\right]. \tag{6.14}$$

Now $D \to \epsilon\mathcal{D}$ is an obvious consequence to be able to divide each term by ϵ yielding

$$\epsilon\dot{\mathcal{D}}(t) = \gamma\left[-\mathcal{D}(t) + \Im(\chi(\epsilon\mathcal{D}))|\mathcal{E}|^2\right], \tag{6.15}$$

as well as $\chi(\epsilon\mathcal{D})$ in general. For Eq. (6.6) one finds

$$\begin{aligned}\epsilon^{\frac{1}{2}}\epsilon\left(\dot{\mathcal{E}}(t) + \eta\dot{\mathcal{E}}(t-1)\right) =& \epsilon^{\frac{1}{2}}\left[i\epsilon^2 f\chi(\epsilon\mathcal{D}) - 1 - i\delta\right]\mathcal{E}(t) \\ &+ \epsilon^{\frac{1}{2}}\eta\left[i\epsilon^2 f\chi(\epsilon\mathcal{D}(t-1)) - 1 - i\delta\right]\mathcal{E}(t-1) \\ &+ \epsilon^{\frac{1}{2}}h\eta\mathcal{E}(t-1) + \epsilon^{\frac{1}{2}}h\mathcal{Y}_0\sqrt{(}1-\eta^2).\end{aligned} \tag{6.16}$$

Here $\epsilon^{\frac{1}{2}}$ can be taken away from each term to reproduce the old equation only differing in the argument of χ. To write the susceptibility as a polynomial in ϵ, a Taylor expansion can be included for small ϵ, leading to:

$$\chi(\epsilon\mathcal{D}) = \chi(0) + \epsilon\chi'(0)\mathcal{D} + \mathcal{O}(\epsilon^2). \tag{6.17}$$

Note that the higher order terms will not occur in the final equation if only a total order of $\mathcal{O}(\epsilon^3)$ is considered. The terms $\chi(0)$ and $\chi'(0)$ are the complex terms

$$\chi(0) = \frac{1}{\pi}\ln\left(\frac{u+i-b}{(u+i)b}\right) = \frac{1}{\pi}\ln\left(\frac{1}{b} - \frac{1}{u+i}\right) \approx \frac{1}{\pi}\ln\left(\frac{-1}{u+i}\right) = -\frac{1}{\pi}\ln(-u-i), \tag{6.18}$$

$$\chi'(0) = \frac{1}{\pi}\frac{2}{u+i-0} = \frac{1}{\pi}\frac{2(u-i)}{u^2+1}, \tag{6.19}$$

which do not depend on the fields. Here, $b \gg 1$ has been used. This approximation is optional and can be omitted easily, if needed, since the susceptibility will be inserted in the final equation. The imaginary part of $\chi(0)$ can be isolated using the Arg function:

$$
\begin{aligned}
-\ln(-u-i) &= -\ln|u+i| - i\mathrm{Arg}(-u-i) && (6.20)\\
&= -\ln\sqrt{u^2+1} + i\left[\frac{\pi}{2} + \arctan(u)\right]. && (6.21)
\end{aligned}
$$

This leads to

$$
\begin{aligned}
\chi(0) &= -\frac{1}{\pi}\ln\sqrt{u^2+1} + i\left[\frac{1}{2} + \frac{1}{\pi}\arctan(u)\right] = R_0 + iI_0, && (6.22)\\
\chi'(0) &= \frac{2}{\pi}\frac{u-i}{u^2+1} = R_1 + iI_1, && (6.23)
\end{aligned}
$$

which yields an approximated susceptibility

$$
\chi(\epsilon\mathcal{D}) = R_0 + iI_0 + \epsilon(R_1 + iI_1)\mathcal{D} + \mathcal{O}(\epsilon^2), \tag{6.24}
$$

with the nonlinear term in $\mathcal{O}(\epsilon^3)$. Inserting these results one finds for $\dot{\mathcal{D}}$

$$
\begin{aligned}
\epsilon\dot{\mathcal{D}}(t) &= \gamma\left[-\mathcal{D}(t) + \Im(\chi(\epsilon\mathcal{D}))|\mathcal{E}|^2\right] && (6.25)\\
&= \gamma\left[-\mathcal{D}(t) + (I_0 + \epsilon I_1\mathcal{D}(t))|\mathcal{E}(t)|^2\right]. && (6.26)
\end{aligned}
$$

6.2. Derivation

6.2.1. Time Derivative and Drift Operator

Now the corresponding time derivative operator is:

$$
\partial_t = \omega\partial_0 + \epsilon^2\partial_2 + \epsilon^3\partial_3. \tag{6.27}
$$

To equalize the drift the expression $\omega = 1 + \epsilon\omega_1 + \epsilon^2\omega_2 + \epsilon^2\omega_3$ can be used which leads to:

$$
\begin{aligned}
\partial_t &= \partial_0 + \epsilon\omega_1\partial_0 + \epsilon^2(\omega_2\partial_+\partial_2) + \epsilon^3(\omega_3\partial_0 + \partial_3) + \mathcal{O}(\epsilon^4) && (6.28)\\
&= \mathcal{T}_0 + \epsilon\mathcal{T}_1 + \epsilon^2\mathcal{T}_2 + \epsilon^3\mathcal{T}_3. && (6.29)
\end{aligned}
$$

The field has to be written with respect to the new time scale. Thus, $\mathcal{E}(t) = \mathcal{E}(t_0, t_2, t_3)$, but also $\mathcal{E}(t-1) = \mathcal{E}(t_0 - \omega, t_2 - \epsilon^2, t_3 - \epsilon^3)$ has to be used. In order to sort the system by orders of ϵ an expansion for small ϵ can be used to rewrite the time-delayed field

$$
\begin{aligned}
\mathcal{E}(t_0 - \omega, t_2 - \epsilon^2, t_3 - \epsilon^3) =& \mathcal{E}(t_0 - 1 - \epsilon\omega_1 - \epsilon^2\omega_2 - \epsilon^3\omega_3, t_2 - \epsilon^2, t_3 - \epsilon^3) && (6.30)\\
=& \mathcal{E}(t_0 - 1, t_2, t_3) + \epsilon(-\omega_1\partial_0)\mathcal{E}(t_0 - 1, t_2, t_3)\\
&+ \epsilon^2\left(\frac{\omega_1^2\partial_0^2}{2} - \omega_2\partial_0 - \partial_2\right)\mathcal{E}(t_0 - 1, t_2, t_3) && (6.31)\\
&+ \epsilon^3\left(\frac{-\omega_1^3\partial_0^3}{6} + \omega_1\omega_2\partial_0^2 + \omega_1\partial_0\partial_2 - \omega_3\partial_0 - \partial_3\right)\mathcal{E}(t_0 - 1, t_2, t_3)
\end{aligned}
$$

The found prefactors correspond to the shift operator $\mathcal{S}$ fulfilling

$$
\begin{aligned}
\mathcal{E}(t_0 - \omega, t_2 - \epsilon^2, t_3 - \epsilon^3) &= \mathcal{S}\mathcal{E}(t_0 - 1) && (6.32)\\
&= \left(1 + \epsilon\mathcal{S}_1 + \epsilon^2\mathcal{S}_2 + \epsilon^3\mathcal{S}_3\right)\mathcal{E}(t_0 - 1), && (6.33)
\end{aligned}
$$

with the reduced notation $\mathcal{E}(t_0-1,t_2,t_3)=\mathcal{E}(t_0-1)$.
Using the operators introduced above all definitions can be inserted into Eq. (6.16) and Eq. (6.26). Additionally, the fields are expanded in a power series as $\mathcal{E}=\mathcal{E}_0+\epsilon\mathcal{E}_1+\epsilon^2\mathcal{E}_2+\epsilon^3\mathcal{E}_3+\mathcal{O}(\epsilon^4)$. Afterwards the resulting expressions will be sorted in orders of ϵ which will be considered separately. For a full derivation, see sections B.2 and B.3. Only main results from each order will be presented here.

6.2.2. Solving by Orders

Starting with the lowest order $\mathcal{O}(\epsilon^0)$ one obtains

$$\mathcal{E}_0(t_0)-\mathcal{E}_0(t_0-1)=0, \tag{6.34}$$

describing a simple periodic solution.
Using this, from $\mathcal{O}(\epsilon^1)$

$$\mathcal{E}_1(t_0)-\mathcal{E}_1(t_0-1)=\left(-\omega_1-\frac{2}{\delta^2+1}\right)\partial_0\mathcal{E}_0(t_0), \tag{6.35}$$

is found. This equation describes a periodic solution with a periodicity disturbed by a drift term elucidating the meaning of the expansion in ω as compensation for potential drift. Without the first order term $\omega_1\partial_0\mathcal{E}_0(t_0)$ a nonvanishing drift of $\mathcal{E}_0$ on the time scale t_0 is observed. The drift is compensated through the result for the small frequency correction $\epsilon\omega_1$ by choosing

$$\omega_1=\frac{-2}{1+\delta^2}. \tag{6.36}$$

For $\mathcal{O}(\epsilon^2)$, the lower orders will be used once again leading to $\omega_2=\omega_1^3$. Furthermore, the solvability condition

$$\partial_2\mathcal{E}_0=\left[-i\delta\frac{\omega_1^2}{2}\partial_0^2-L_2\right]\mathcal{E}_0+\Gamma_2, \tag{6.37}$$

is found with

$$L_2=\frac{2(fI_0-ifR_0)}{(1+i\delta)^2}-(\eta_2+i\theta_2), \tag{6.38}$$

$$\Gamma_2=\gamma_1\frac{2\sqrt{-2\eta_2}}{1+i\delta}. \tag{6.39}$$

The operator L_2 contains the first term from the expansion of the susceptibility, but the nonlinearity itself does not enter until $\mathcal{O}(\epsilon^3)$. Here, $\omega_3=\omega_1^3$ is found. The final solvability condition for the third order containing all simplifications, has the form

$$\begin{aligned}\partial_3\mathcal{E}_0+\partial_2\mathcal{E}_1=&-i\frac{3\delta}{2}\omega_1^3\partial_0^2\mathcal{E}_0+\frac{1-3\delta^2}{12}\omega_1^3\partial_0^3\mathcal{E}_0\\&+[\mathcal{N}\mathcal{D}-\omega_1L_2]\mathcal{E}_0+\left[-i\delta\frac{\omega_1^2}{2}\partial_0^2-L_2\right]\mathcal{E}_1+\Gamma_3+\omega_1\Gamma_2,\end{aligned} \tag{6.40}$$

with

$$L_2 = \frac{2(fI_0 - ifR_0)}{(1+i\delta)^2} - (\eta_2 + i\theta_2), \tag{6.41}$$

$$\Gamma_2 = \gamma_1 \frac{2\sqrt{-2\eta_2}}{1+i\delta}, \tag{6.42}$$

$$\Gamma_3 = \gamma_2 \frac{2\sqrt{-2\eta_2}}{1+i\delta}, \tag{6.43}$$

$$\mathcal{N} = \frac{2f(iR_1 - I_1)}{1+i\delta}. \tag{6.44}$$

Equation (6.2) of the $\mathcal{D}$ field that has been rewritten to

$$\epsilon\dot{\mathcal{D}}(t) = \gamma\left[-\mathcal{D}(t) + (I_0 + \epsilon I_1 \mathcal{D}(t))|\mathcal{E}(t)|^2\right], \tag{6.45}$$

has to be discussed as well. Inserting the time derivative operator as well as the nonlinearity leads to

$$\left(\epsilon\partial_0 + \epsilon^2\omega_1\partial_0 + \epsilon^3(\omega_2\partial_0 + \partial_2)\right)\dot{D}(t) = \gamma\left[-D(t) + (I_0 + \epsilon I_1 D(t))|E(t)|^2\right]. \tag{6.46}$$

6.3. Assembling the Full Partial Differential Equation System

Finally the PDE shall be deduced from the previous results. Therefor, an effective time scale

$$\partial_\theta = \epsilon^2\partial_2 + \epsilon^3\partial_3 \tag{6.47}$$

is introduced. The results are now included by using $\mathcal{E} = \mathcal{E}_0 + \epsilon\mathcal{E}_1$, where higher orders of the field fall into $\mathcal{O}(\epsilon^4)$ due to the definition of the time scale. This leads to:

$$\begin{aligned}\partial_\theta\mathcal{E} =& \epsilon^2\left(\left[-i\delta\frac{\omega_1^2}{2}\partial_0^2 - L_2\right]\mathcal{E} + (\gamma_1 + \epsilon\gamma_2)\frac{2\sqrt{-2\eta_2}}{1+i\delta}\right) \\ &+ \epsilon^3\left(\frac{1-3\delta^2}{12}\omega_1^3\partial_0^3\mathcal{E} + [\mathcal{N}\mathcal{D} - \omega_1 L_2]\mathcal{E} + \omega_1\gamma_1\frac{2\sqrt{-2\eta_2}}{1+i\delta}\right).\end{aligned} \tag{6.48}$$

Next, space can be rescaled as $\epsilon|\omega_1|\partial_0 \to \partial_\sigma$, where the absolute value leads to a switch in sign of the third order dispersion:

$$\begin{aligned}\partial_\theta\mathcal{E} =& \left[\frac{-i\delta}{2}\partial_\sigma^2 - \epsilon^2(-\eta_2 + 2W_1 - i\theta_2)\right]\mathcal{E} + h\mathcal{Y}_0\frac{\sqrt{1-\eta^2}}{1+i\delta} - \frac{1-3\delta^2}{12}\partial_\sigma^3\mathcal{E} \\ &+ \epsilon^3\left[\frac{2f(iR_1 - I_1)}{1+i\delta}\mathcal{D} - \omega_1(-\eta_2 + 2W_1 - i\theta_2)\right]\mathcal{E} + \epsilon\omega_1 h\mathcal{Y}_0\frac{\sqrt{1-\eta^2}}{1+i\delta} + \mathcal{O}(\epsilon^4).\end{aligned} \tag{6.49}$$

Applying the parameter expansions yields $\epsilon^2(\eta_2 + i\theta) + \mathcal{O}(\epsilon^4) = \eta e^{i\theta} - 1$. Also, $\epsilon^2 f \to f$ is reset and small terms containing $\epsilon\omega_1$ are removed, yielding

$$\begin{aligned}\partial_\theta\mathcal{E} =& \left[\frac{-i\delta}{2}\partial_\sigma^2 - 2f\frac{I_0 - iR_0}{(1+i\delta)^2} - 1 + \eta e^{i\theta}\right]\mathcal{E} + h\mathcal{Y}_0\frac{\sqrt{1-\eta^2}}{1+i\delta} \\ &- \frac{1-3\delta^2}{12}\partial_\sigma^3\mathcal{E} + \epsilon\frac{2f(iR_1 - I_1)}{1+i\delta}\mathcal{D}\mathcal{E} + \mathcal{O}(\epsilon^4).\end{aligned} \tag{6.50}$$

One can progress by multiplying both sides of the equation by $\epsilon^{\frac{1}{2}}$ and inverting the field's scaling with $\mathcal{E}\epsilon^{\frac{1}{2}} \to E$, $\mathcal{Y}_0\epsilon^{\frac{1}{2}} \to Y_0$ and $\mathcal{D}\epsilon \to D$, which results in

$$\begin{aligned}\partial_\theta E =& \frac{-i\delta}{2}\partial_\sigma^2 E - \frac{1-3\delta^2}{12}\partial_\sigma^3 E + \frac{2f(iR_1 - I_1)}{1+i\delta}DE \\ &+ \left[-2f\frac{I_0 - iR_0}{(1+i\delta)^2} - 1 + \eta e^{-i2\arctan(\delta)}\right]E + hY_0\frac{\sqrt{1-\eta^2}}{1+i\delta}.\end{aligned} \tag{6.51}$$

Here, the original fields from Eqs. (6.1) - (6.4) are recovered. This is necessary to compare the derived PDE with the underlying DAE system.
After expanding the exponential function for small values of δ only the coefficients R_0, I_0, R_1, and I_1 remain. Hence, the approximation for the susceptibility shall be finally inserted leading to

$$\begin{aligned}\partial_\theta E =& \frac{-i\delta}{2}\partial_\sigma^2 E - \frac{1-3\delta^2}{12}\partial_\sigma^3 E + \frac{4f}{\pi}\frac{(1+iu)(1-i\delta)}{(1+u^2)(1+\delta^2)}DE \\ &+ \left[-\frac{2f}{\pi}(1-i\delta)^2\frac{i\ln\sqrt{u^2+1} + \frac{\pi}{2} + \arctan(u)}{(1+\delta^2)^2} - 1 + \eta - i2\eta\arctan(\delta)\right]E \\ &+ hY_0\frac{\sqrt{1-\eta^2}}{1+i\delta},\end{aligned} \tag{6.52}$$

which is this section's final PDE for E. The second equation

$$(\epsilon\partial_0 + \epsilon^2\omega_1\partial_0 + \epsilon^3(\omega_2\partial_0 + \partial_2))\mathcal{D}(t) = \gamma\left[-\mathcal{D}(t) + (I_0 + \epsilon I_1\mathcal{D}(t))|\mathcal{E}(t)|^2\right] \tag{6.53}$$

will be simplified using $\epsilon|\omega_1|\partial_0 = \partial_\sigma$ as well as $\epsilon^2\partial_2 + \omega^3\partial_3 = \partial_\theta$. However, one needs to keep in mind that the fields involved still have to be rescaled. Thus, $\mathcal{E}\epsilon^{\frac{1}{2}} \to E$ and $\mathcal{D}\epsilon \to D$ are applied. This leads to

$$\left(\frac{1}{-\omega_1}\partial_\sigma - \epsilon(\partial_\sigma + \partial_\theta) + \epsilon^3\omega_2\partial_0 + \omega^4\omega_3\partial_0\right)\frac{1}{\epsilon}D = \gamma\left[\frac{-1}{\epsilon}D + (I_0 + I_1\frac{\epsilon}{\epsilon}D)\frac{1}{\epsilon}|E|^2\right], \tag{6.54}$$

which is equivalent to

$$\left(\frac{1}{-\omega_1}\partial_\sigma - \epsilon\partial_\sigma + \epsilon\partial_\theta - \epsilon^2\omega_1\partial_\sigma - \epsilon^3\omega_1^2\partial_\sigma\right)\frac{1}{\epsilon}D = \frac{\gamma}{\epsilon}\left[-D + (I_0 + I_1D)|E|^2\right]. \tag{6.55}$$

Here, the relations $\omega_2 = \omega_1^2$ and $\omega_3 = \omega_1^3$ have been used to rewrite all derivative operators with the new scales σ and θ. Now each side is multiplied by ϵ. In a first attempt the lowest order can be used to describe the dynamics of D as

$$\partial_\sigma D = -\omega_1\gamma\left[-D + (I_0 + I_1D)|E|^2\right]. \tag{6.56}$$

However, interpreting σ as a quasi-spatial variable and θ as the time variable this is not a differential equation in time σ. Indeed this section leads to a PDE in $E(t)$ with a constraint for the field $D(t)$. The resulting system is

$$\begin{aligned}\partial_\theta E =& \frac{-i\delta}{2}\partial_\sigma^2 E - \frac{1-3\delta^2}{12}\partial_\sigma^3 E + \frac{4f}{\pi}\frac{(1+iu)(1-i\delta)}{(1+u^2)(1+\delta^2)}DE \\ &+ \left[-\frac{2f}{\pi}(1-i\delta)^2\frac{i\ln\sqrt{u^2+1}+\frac{\pi}{2}+\arctan(u)}{(1+\delta^2)^2} - 1 + \eta - i2\eta\arctan(\delta)\right]E \\ &+ hY_0\frac{\sqrt{1-\eta^2}}{1+i\delta}, \end{aligned} \tag{6.57}$$

$$0 = -\partial_\sigma D + \frac{\gamma}{1+\delta^2}\left[-2D + \left(1 + \frac{2}{\pi}\arctan(u) - \frac{4}{\pi}\frac{1}{u^2+1}D\right)|E|^2\right]. \tag{6.58}$$

The equations are finally simplified to

$$\partial_\theta E = \left(id_2\partial_\sigma^2 + d_3\partial_\sigma^3 + \mathcal{L}\right)E + \mathcal{N}DE + hY_0\frac{\sqrt{1-\eta^2}}{1+i\delta}, \tag{6.59}$$

$$0 = \left(\zeta_3\partial_\sigma - 2 - \zeta_2|E|^2\right)D + \zeta_1|E|^2, \tag{6.60}$$

with

$$d_2 = -\frac{\delta}{2}, \tag{6.61}$$

$$d_3 = \frac{3\delta^2-1}{12}, \tag{6.62}$$

$$\mathcal{L} = -\frac{2f}{\pi}(1-i\delta)^2\frac{i\ln\sqrt{u^2+1}+\frac{\pi}{2}+\arctan(u)}{(1+\delta^2)^2} - 1 + \eta - i2\eta\arctan(\delta), \tag{6.63}$$

$$\mathcal{N} = \frac{4f}{\pi}\frac{(1+iu)(1-i\delta)}{(1+u^2)(1+\delta^2)}, \tag{6.64}$$

$$\zeta_1 = \left(1 + \frac{2}{\pi}\arctan(u)\right), \tag{6.65}$$

$$\zeta_2 = \frac{4}{\pi}\frac{1}{u^2+1}, \tag{6.66}$$

$$\zeta_3 = -\frac{1+\delta^2}{\gamma}. \tag{6.67}$$

6.4. Calculating the Continuous Wave Solution

For the CW solution the fields are constant on both scales leading to

$$0 = \mathcal{L}E + \mathcal{N}DE + hY_0\frac{\sqrt{1-\eta^2}}{1+i\delta}, \tag{6.68}$$

$$0 = \left(-2 - \zeta_2|E|^2\right)D + \zeta_1|E|^2. \tag{6.69}$$

The latter equation describes a relation $D(|E|^2)$ that can be inserted into the former equation to find a CW solution $Y_0(E)$. For plotting purposes the electric field will be rewritten with intensities $I = |E|^2$:

$$Y_0^2 = \frac{1+\delta^2}{h^2(1-\eta^2)}|\mathcal{L} + \mathcal{N}D(I)|^2 I, \tag{6.70}$$

$$D(I) = \frac{\zeta_1 I}{2+\zeta_2 I}. \tag{6.71}$$

The resulting CW states are shown in Fig. 6.1 where the two CW branches NF_{Ω_0} and $\mathrm{NF}_{\tilde{\Omega}}$ have been calculated analytically from Eqs. (6.70) - (6.71). They are compared to the CW branch PC_{Ω_0} from the point Ω_0 in parameter space which was a result of Section 5.2 for the DAE system Eqs. (6.1) - (6.4). The branch was shown before in Fig. 5.12 and has been calculated using numerical path continuation. This particular branch is chosen here since the respective parameter set Ω_0 was used as an example for bright and dark TLS regimes in a good cavity limit.
One can see that NF_{Ω_0} diverges from PC_{Ω_0} showing no bistable regime at all. However, for slight parameter adjustments, namely a detuning value of $\delta = 0.044$, $u = 0.52$ and $\gamma = 10$, a bistable regime establishes for the PDE almost identical to the results from numerical path continuation. The corresponding new set of parameters will be called $\tilde{\Omega}$. From the two-parameter diagram in Fig. 5.10 b) one can see that the existence of a bistable regime has a limited detuning range in the DAE system as well. This indicates a small shift in parameters between PDE and DAE results.

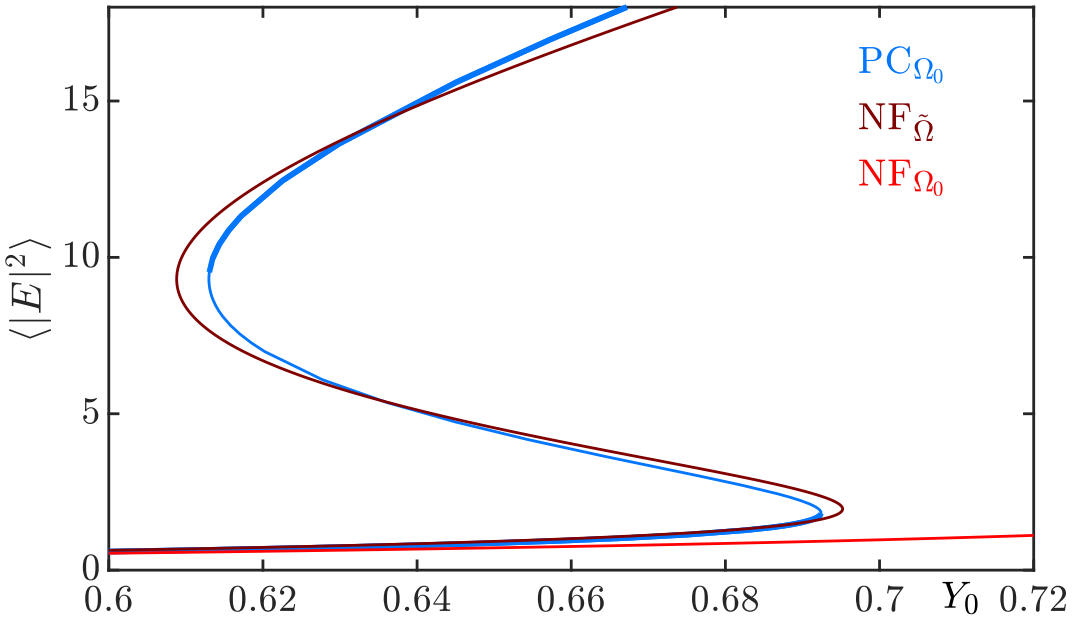

Figure 6.1: Comparing the CW solution gained from the Normal form (NF) with the solution from numerical path continuation (PC) for the parameter set Ω_0 shown in Fig. 5.12. The bistable region for the respective CW branch features dark and bright TLS regimes in extended regions around a vertical Maxwell line. The respective parameters for Ω_0 are $(\delta, h, \eta, \varphi, \gamma, f, u, b, \tau) = (0.015, 2, 0.99, 0, 1, 0.2, 0.65, 1000, 250)$. To obtain the bistable branch $\mathrm{NF}_{\tilde{\Omega}}$ the parameters have been slightly adjusted to the new parameter set $\tilde{\Omega}$ with the differences $u = 0.52$, $\delta = 0.044$ and $\gamma = 10$.

6.5. Periodic Solutions

The next natural step is to investigate the PDE system derived in this section in more detail looking for TLS and comparing it with the underlying DAE system for the QGTI. This is achieved by implementing the PDE system Eqs. (6.59) and (6.60) and performing direct numerical simulations. If the approximations and assumptions throughout the derivation are reasonable for the QGTI system in a good cavity limit it should be possible to establish stable TLS for a good choice of parameters and initial conditions that are similar to those observed in the DAE system Eqs. (6.1) - (6.4). Since Fig. 6.1 indicates

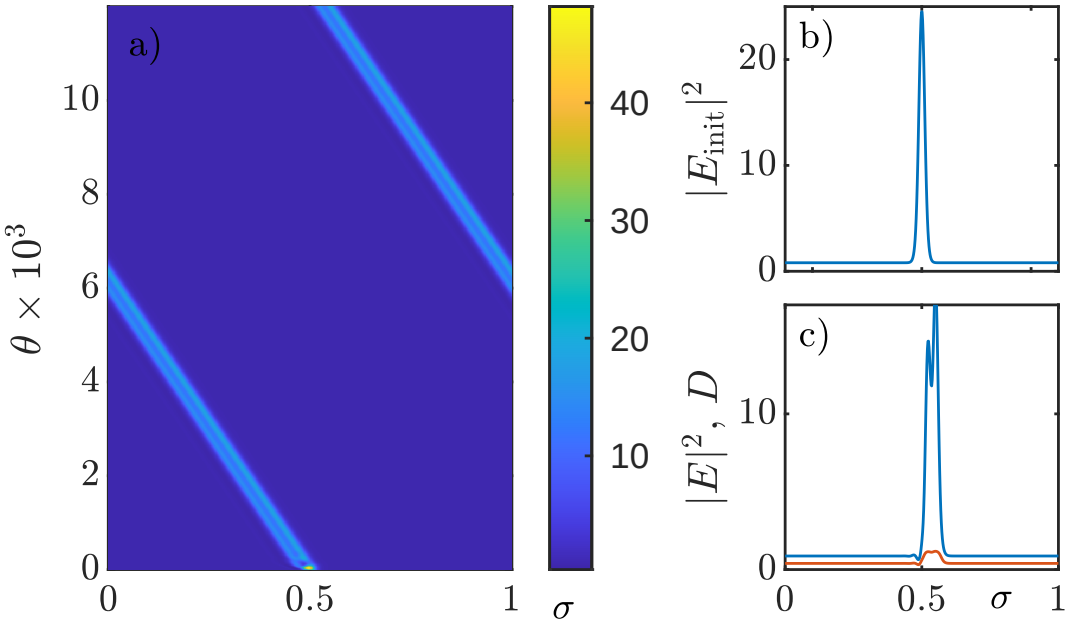

Figure 6.2: a): Time evolution of a bright TLS for the QGTI PDE occurring for the parameter set $\tilde{\Omega}$ at injection $Y_0 = 0.6437$. The simulation shows 12000 roundtrips indicating that the appearing TLS is a stable solution. b): Initial condition taken from the periodic branch for the respective DAE system at Ω_0 found in Section 5.2. c): The bright TLS at the end of the time simulation is locked at second locking distance, indicated by the single convolution of an oscillatory tail in the peak. The profile for D (orange) is shown as well.

a bistable regime for the PDE system in the parameter set $\tilde{\Omega}$ that is almost identical to the bistable regime occurring in the DAE system for Ω_0, points from the periodic the respective periodic branch found for Ω_0 in Section 5.2 will be used as initial conditions. The numerical simulation is done using a split-step based pseudo-spectral method for the evolution of E in θ direction. The dynamics of D are evaluated in σ direction using an implicit Euler scheme for each roundtrip. Results are plotted in the quasi-space-time representation where θ is the time direction and σ the new spatial variable with periodic boundary conditions.

Figure 6.2 a) shows the time evolution of a bright TLS that stabilizes within the bistable CW regime visible for the branch $\text{NF}_{\tilde{\Omega}}$ from Fig. 6.1. The respective initial condition shown in b) is a bright TLS taken from periodic solutions found for Ω_0. In panel c) the profile of the resulting TLS is shown which seems to be invariant over the whole time simulation. However, the fronts lock at the second locking distance which can be seen

from the single convolution of a tail in the peak. This is also visible in panel a) where the lightblue line resembling the TLS shows a darker line in the middle. Indeed, it does not seem to be possible to lock fronts in the closest locking distance for bright pulses in the DAE system. This is different for dark TLSs as shown in Fig. 6.3. In a) one can observe

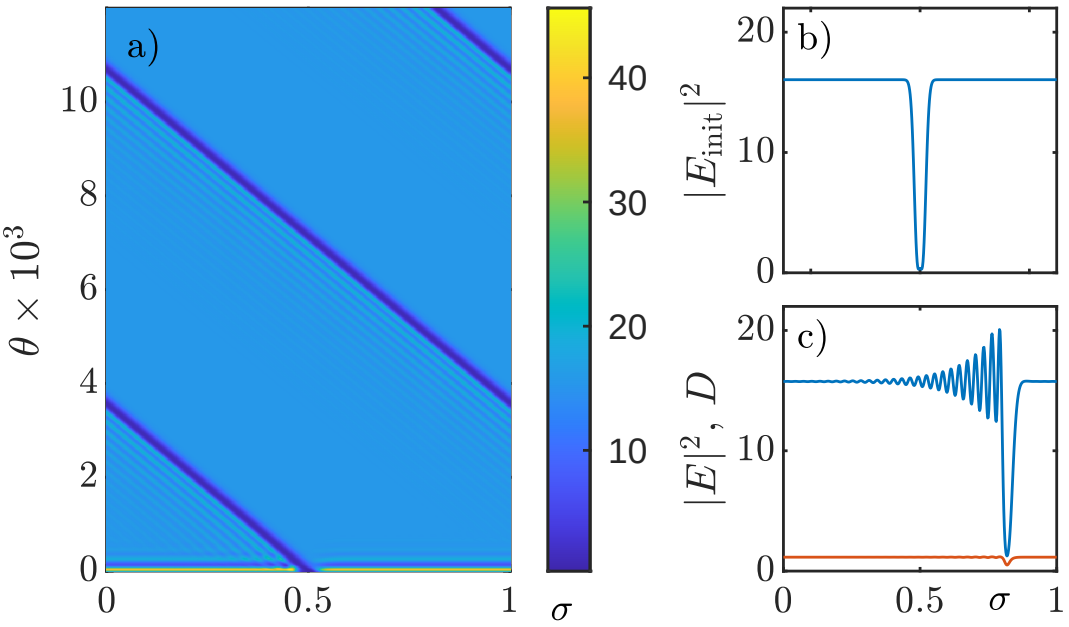

Figure 6.3: a): Time evolution of a dark TLS for the QGTI PDE occurring for the parameter set $\tilde{\Omega}$ at injection $Y_0 = 0.6491$. The simulation shows 12000 roundtrips indicating that the appearing TLS is a stable solution. b): Initial condition taken from the periodic branch for the respective DAE system at Ω_0. c): The dark TLS at the end of the time simulation shows a strong asymmetric oscillating tail as it also was the case for the dark pulse obtained from Ω_0 for the DAE system which is shown in Fig. 5.12. The profile for D (orange) is shown as well.

the time evolution of a seemingly stable dark TLS. The initial condition visible in b) is a single dark TLS that evolves into a dark TLS with strong asymmetric oscillatory tail as seen in c). The oscillatory tail can also be recognized in a) by the accompanying stripes that fade away with increasing distance.

Finally, Fig. 6.4 shows the time evolution of an initial bright TLS for an increased injection value. Apparently, appearing fronts show different drifting speeds due to the injection value being higher than the Maxwell line and snaking region that is expected to occur in the PDE system as well. In a) one can observe a resulting increase of the higher plateau value regime (light blue) until the lower plateau value (dark blue) regime is fully consumed. This results in a CW solution as shown in c). Comparing the profiles of the stable TLS from the PDE with DAE results it is noticable that the initial condition which is a TLS, where the fronts are locked in closest locking distance evolves into a TLS where the fronts are further separated. Figure 6.5 shows that TLSs of this type are stable the DAE system as well. However, they occur not on the lowest region of stable TLSs, but at the one above indicating that the snaking structure for the PDE is missing the lowest regime. Also, the dark TLSs from the PDE seems to have more oscillatory tail than its counterpart from the DAE system. However, the tendency of dark TLSs

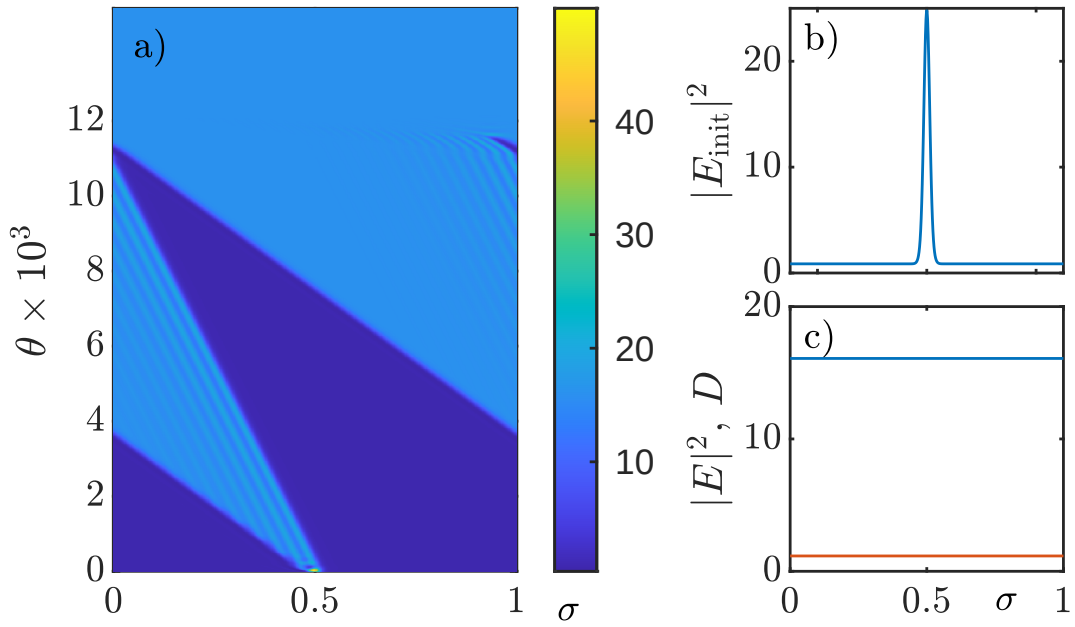

Figure 6.4: a): Time evolution of a bright TLS for the QGTI PDE occurring for the parameter set $\tilde{\Omega}$ at injection $Y_0 = 0.6524$. Apparently, appearing fronts show different drifting speeds due to the injection value being higher than the Maxwell line and snaking region. This leads to an increase of the higher plateau value (light blue) until the lower plateau value (dark blue) is fully consumed. b) Initial bright TLS. c): Steady state solution at the end of the time simulation. The profile for D (orange) is shown as well.

to feature more oscillatory tail than bright TLSs in this parameter regimes is preserved from the DAE to the PDE.
Finally, one should discuss the the sets of parameters Ω_0 and $\tilde{\Omega}$. While the differences in u and δ can be explained by a small parameter shift between the PDE and DAE system the value of γ grows from $\gamma_{\Omega_0} = 1$ to $\gamma_{\tilde{\Omega}} = 10$ by an order of magnitude. The parameter γ, called the scaled carrier lifetime, plays an important role as it defines a time scale for the DAE system. As shown in Fig. 5.10 a) values below $\gamma \approx 1$ strongly influence the branch structure of the periodic branches. So it is possible that the PDE system does not describe the DAE system for lower values of γ. This could be investigated in more detail using numerical path continuation for the PDE system in future works.
All in all these results demonstrate that the PDE system derived within this section is a promising candidate for a adequate description of the dynamics of TLS occurring in the DAE system for the QGTI in a good cavity limit.

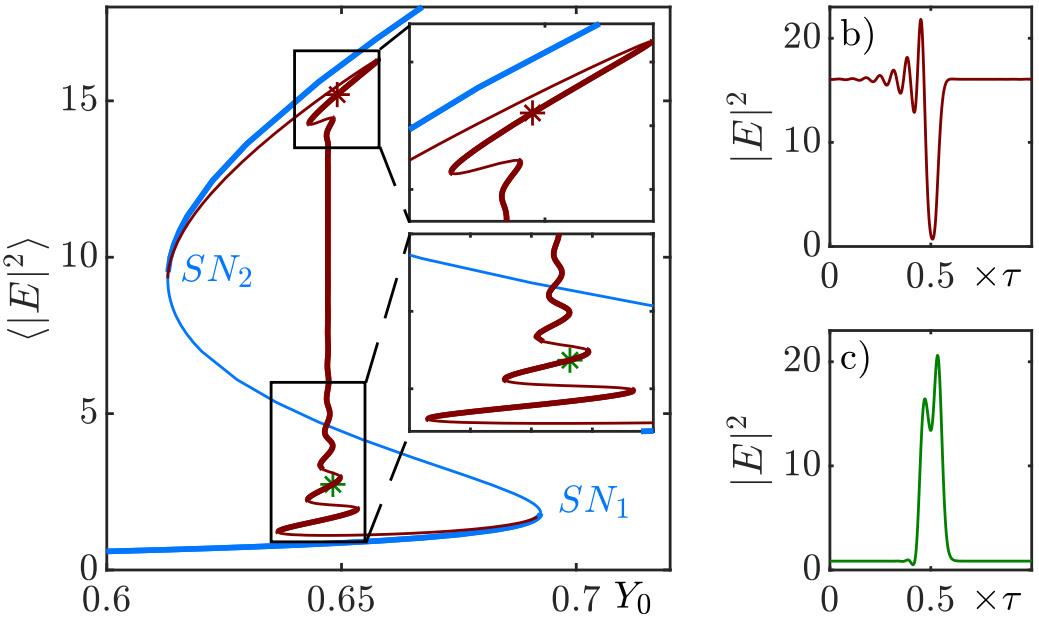

Figure 6.5: The branch already shown in Fig. 5.12 branch featuring stable bright and dark pulses. However, a stable bright TLS from the second lowest regime of stable periodic solution has been chosen in c) showing a split peak as the solutions observed for the PDE system. Parameters: $(\delta, h, \eta, \varphi, \gamma, f, u, b, \tau) = (0.015, 2, 0.99, 0, 1, 0.2, 0.65, 1000, 250)$.

7. Summary and Outlook

In this thesis, SWs and pulsating dynamics in time-delayed active micro-cavities have been investigated using the example of a dispersive microcavity with Kerr nonlinearity as well as with a quantum well. The system has been described using a DAE model with a single delay describing the round-trip duration for the external cavity acting as feedback loop.
The first part of this thesis consisted of a bifurcation analysis for recently found SW regimes in the KGTI. Therefor a MATLAB implementation for the system was used allowing for a numerical path-continuation additionally utilizing the DDE-BIFTOOL package. Amongst the most important results is the distinction of two qualitatively different types of SW emergence. Firstly, SWs can emerge in a supercritical Hopf bifurcation, leading to a plainly shaped bridge of stable SWs that arise from a sinus-alike solution in the vicinity of their onset. Secondly, SWs can emerge in a subcritical Hopf bifurcation where two pairs of unstable fronts arise from the stable CW solution connecting it to the later plateau values. The opposing fronts for each pair then gradually separate along a vertical Maxwell line interacting through their oscillatory tails. This leads to a multitude of preferred distances and hence stable configurations. The branch resembles these configurations in a collapsed snaking structure around the Maxwell line. In both cases the fully developed SWs consist of two plateaus with sharp transition layers and a 50% limit cycle.
For certain parameter sets chaotic regimes have been observed arising on the SW branches in a PD route to chaos. These were investigated using direct numerical simulation that allow to illustrate the higher period solutions. Also, another type of SWs consisting of three plateaus of equal length could be observed and described.
Furthermore an analytical description of SWs has been provided to further investigate and potentially support these observation. On this occasion an equation for the SW branches as well as the bifurcation points where they arise from the CW branch has been derived successfully.
The analytical description was mainly based on a so-called two-plateau approximation that assumes simple SW solutions consisting only of two plateaus of equal length. While this approximation proofs to be successful in the description of SW regimes featuring solutions with a 50% limit cycle the analytically calculated branches fail to depict the Maxwell line and snaking parts of the SW branches from numerical continuation. This can be explained with the profiles along the Maxwell line which generally consist of three plateaus of unequal length and hence do not fulfill the underlying approximation. However the bifurcation points have been predicted in accordance with the numerical continuation.
The observation of SWs equipped with strong oscillatory tails motivated an attempt to write fronts and pulses onto stable SWs to investigate the stability of more complex bound states. Throughout the corresponding section the role of the tail-induced potential for the formation of bound states has been observed and discussed in detail. Especially in the subcritical case the tail-induced locking of fronts showed to form bound states on the plateaus that can be robust against noise, while in the supercritical case initial conditions result in full coarsening at some point under the influence of noise.
Note that some of the results presented in this part have also been published recently [Koc+22].
In the second major part of this thesis a bifurcation analysis has been done for the QGTI system which is similar to the KGTI, however containing a quantum well acting as nonlinearity. The first investigations aimed at finding bistable regimes with periodic

pulsed solutions. An attempt to connect the two systems using adequate approximations led to first results for periodic pulsed solutions in a bistable CW regime. In a second attempt bright and dark pulses have been found in a weakly dissipative regime which is also called the good cavity limit due to the high reflection coefficient η minimizing the overall cavity losses. In a similar regime, only varying the phase to $\varphi = \pi$, SWs occur in the QGTI. A bifurcation analysis revealed the same transition from a subcritical to a supercritical case. However, the branches are mirrored in a way that the subcritical Hopf bifurcation and hence the snaking region appear at the Hopf bifurcation that is located higher in injection. Finally, the mentioned good cavity limit has been investigated for the KGTI in recent publications, particularly it represents a good expansion point for a weakly nonlinear analysis leading to a normal form. Accordingly, in the final section a normal form has been derived for the QGTI in the same parameter regime which aims at extending the understanding of the system and its relation to the KGTI. The resulting PDE system was able to reproduce bistable continuous wave regimes as well as bright and dark pulses in only slightly shifted parameter regimes relative to the DAE results. Features such as the stronger oscillatory tail in dark compared to bright pulses have been successfully reproduced.

All in all this thesis was able to discuss and outline some of the rich behavior that can be found in active micro-cavities. Different types of SWs and pulsed solutions have been found and described systematically providing bifurcation analyses as well as analytical investigations. Nevertheless this topic still has a lot to offer for future investigations of which a few examples shall now be introduced.

While SWs have been found in multistable regimes, especially around the Maxwell line in the subcritical regime, they mostly arise even from constant initial conditions when the CW state becomes unstable. This makes them easily accessible for direct numerical simulations, but also for potential experimental realizations which could be useful for future research. Furthermore, the bifurcation analyses for the KGTI can be extended, e.g. for other values of the phase φ where this thesis already demonstrated that SWs can exist. This could be combined with an extended research on multi-plateau SWs such as the three-plateau SW_3 solutions introduced earlier. One could investigate their general behavior and stability over larger parameter regimes as well as their origin, i.e. where they probably connect to the CW branch. In that context it would also be interesting to see if the analytical two-plateau description can be extended to higher plateau SWs. Since the plateaus in the case of SW_3 solutions occur in a fixed order a three-plateau approximation should lead to six coupled algebraic equations connecting each plateau value to its precursor plateau. Furthermore it might be interesting to do a more detailed analysis of chaotic regimes occurring in the KGTI. While this thesis focused on periodic solution and hence mostly avoided chaotic regimes, there is still a lot to explore in the structure and emergence of chaotic attractors and routes towards them.

For the newly introduced QGTI system initial analyses have been provided giving a good perspective on the rich behavior that this system has to offer. While the already found regimes of dark and bright pulses as well as SWs could be interesting for experimental realizations of the system, the high dimensional parameter space might still hide a variety of regimes that are interesting for further theoretical investigations. Especially the provided proposition for a normal form of the system in a good cavity limit is a promising candidate to help gaining a better understanding of the QGTI and the influence which the many parameters have on the resulting dynamics. A possible next step here would be a bifurcation analysis of the proposed system to investigate to what extend it is able to describe and explain the dynamics in the underlying DAE system.

A. References

[Ern08] T. Erneux. *Applied Delay Differential Equations*. Surveys and Tutorials in the Applied Mathematical Sciences. Dordrecht: Springer, 2008. URL: https://cds.cern.ch/record/1338316.

[KKP17] A. Keane, B. Krauskopf, and C. M. Postlethwaite. "Climate modelling with delay differential equations". In: (2017).

[Mac89] M. C. Mackey. "Commodity price fluctuations: Price dependent delays and nonlinearities as explanatory factors". In: *Journal of Economic Theory* 48.2 (1989), pp. 497–509. ISSN: 0022-0531. DOI: https://doi.org/10.1016/0022-0531(89)90039-2. URL: https://www.sciencedirect.com/science/article/pii/0022053189900392.

[Oro+09] G. Orosz, R. E. Wilson, R. Szalai, and G. Stépán. "Exciting traffic jams: Nonlinear phenomena behind traffic jam formation on highways". In: *Physical review E* 80.4 (2009), p. 046205.

[OWS10] G. Orosz, R. E. Wilson, and G. Stépán. "Traffic jams: dynamics and control". In: *Philosophical Transactions of the Royal Society A: Mathematical, Physical and Engineering Sciences* 368.1928 (2010), pp. 4455–4479.

[Ste+21] F. Stelzer, A. Röhm, R. Vicente, I. Fischer, and S. Yanchuk. "Deep neural networks using a single neuron: folded-in-time architecture using feedback-modulated delay loops". In: *Nature communications* 12.1 (2021), pp. 1–10.

[Ike79] K. Ikeda. "Multiple-valued stationary state and its instability of the transmitted light by a ring cavity system". In: *Optics Communications* 30.2 (1979), pp. 257–261. ISSN: 0030-4018. DOI: http://dx.doi.org/10.1016/0030-4018(79)90090-7. URL: http://www.sciencedirect.com/science/article/pii/0030401879900907.

[RBM11] M. Rossetti, P. Bardella, and I. Montrosset. "Modeling Passive Mode-Locking in Quantum Dot Lasers: A Comparison Between a Finite-Difference Traveling-Wave Model and a Delayed Differential Equation Approach". In: *Quantum Electronics, IEEE Journal of* 47.5 (May 2011), pp. 569–576. ISSN: 0018-9197. DOI: 10.1109/JQE.2010.2104135.

[Reb+11] N. Rebrova, G. Huyet, D. Rachinskii, and A. G. Vladimirov. "Optically injected mode-locked laser". In: *Phys. Rev. E* 83 (6 June 2011), p. 066202. DOI: 10.1103/PhysRevE.83.066202. URL: https://link.aps.org/doi/10.1103/PhysRevE.83.066202.

[LK80] R. Lang and K. Kobayashi. "External optical feedback effects on semiconductor injection laser properties". In: *Quantum Electronics, IEEE Journal of* 16.3 (Mar. 1980), pp. 347–355. ISSN: 0018-9197. DOI: 10.1109/JQE.1980.1070479.

[Sch21] C. Schelte. "Dynamics of Optical Localized Structures in Passively Mode-Locked Lasers". PhD thesis. Westfälische Wilhelms-Universität Münster, 2021.

[VT05] A. G. Vladimirov and D. Turaev. "Model for passive mode locking in semiconductor lasers". In: *Phys. Rev. A* 72 (3 Sept. 2005), p. 033808. DOI: 10.1103/PhysRevA.72.033808. URL: http://link.aps.org/doi/10.1103/PhysRevA.72.033808.

[Tro+04] A. C. Tropper, H. D. Foreman, A. Garnache, K. G. Wilcox, and S. H. Hoogland. "Vertical-external-cavity semiconductor lasers". In: *J. Phys. D: Appl. Phys.* 37 (2004), R75–R85.

[Sch+19a] C. Schelte, P. Camelin, M. Marconi, A. Garnache, G. Huyet, G. Beaudoin, I. Sagnes, M. Giudici, J. Javaloyes, and S. V. Gurevich. "Third Order Dispersion in Time-Delayed Systems". In: *Phys. Rev. Lett.* 123 (4 July 2019), p. 043902. DOI: 10.1103/PhysRevLett.123.043902. URL: https://link.aps.org/doi/10.1103/PhysRevLett.123.043902.

[Sch+20] C. Schelte, D. Hessel, J. Javaloyes, and S. V. Gurevich. "Dispersive Instabilities in Passively Mode-Locked Integrated External-Cavity Surface-Emitting Lasers". In: *Phys. Rev. Applied* 13 (5 May 2020), p. 054050. DOI: 10.1103/PhysRevApplied.13.054050. URL: https://link.aps.org/doi/10.1103/PhysRevApplied.13.054050.

[Sch+19b] C. Schelte, A. Pimenov, A. G. Vladimirov, J. Javaloyes, and S. V. Gurevich. "Tunable Kerr frequency combs and temporal localized states in time-delayed Gires–Tournois interferometers". In: *Optics Letters* 44.20 (2019), pp. 4925–4928.

[HGJ21] D. Hessel, S. V. Gurevich, and J. Javaloyes. "Wiggling instabilities of temporal localized states in passively mode-locked vertical external-cavity surface-emitting lasers". In: *Opt. Lett.* 46.10 (May 2021), pp. 2557–2560. DOI: 10.1364/OL.428182. URL: http://ol.osa.org/abstract.cfm?URI=ol-46-10-2557.

[JAH15] J. Javaloyes, T. Ackemann, and A. Hurtado. "Arrest of Domain Coarsening via Anti-periodic Regimes in Delay Systems". In: *Phys. Rev. Lett.* 115 (22 Nov. 2015), p. 223901. DOI: 10.1103/PhysRevLett.112.223901.

[Gia+12] G. Giacomelli, F. Marino, M. A. Zaks, and S. Yanchuk. "Coarsening in a bistable system with long-delayed feedback". In: *EPL (Europhysics Letters)* 99.5 (2012), p. 58005. URL: http://stacks.iop.org/0295-5075/99/i=5/a=58005.

[YG14] S. Yanchuk and G. Giacomelli. "Pattern Formation in Systems with Multiple Delayed Feedbacks". In: *Phys. Rev. Lett.* 112 (17 May 2014), p. 174103. DOI: 10.1103/PhysRevLett.112.174103. URL: http://link.aps.org/doi/10.1103/PhysRevLett.112.174103.

[WY06] M. Wolfrum and S. Yanchuk. "Eckhaus instability in systems with large delay". In: *Phys. Rev. Lett.* 96.22 (2006), p. 220201. DOI: 10.1103/PhysRevLett.96.220201. URL: https://link.aps.org/doi/10.1103/PhysRevLett.96.220201.

[LPM13] L. Larger, B. Penkovsky, and Y. Maistrenko. "Virtual Chimera States for Delayed-Feedback Systems". In: *Phys. Rev. Lett.* 111 (5 Aug. 2013), p. 054103. DOI: 10.1103/PhysRevLett.111.054103. URL: http://link.aps.org/doi/10.1103/PhysRevLett.111.054103.

[Doy82] J. Doyne Farmer. "Chaotic attractors of an infinite-dimensional dynamical system". In: *Physica D: Nonlinear Phenomena* 4.3 (1982), pp. 366–393. ISSN: 0167-2789. DOI: https://doi.org/10.1016/0167-2789(82)90042-2. URL: https://www.sciencedirect.com/science/article/pii/0167278982900422.

[YLM93] J. Ye, H. Li, and J. G. McInerney. “Period-doubling route to chaos in a semiconductor laser with weak optical feedback”. In: *Physical Review A* 47.3 (1993), p. 2249.

[Koc+22] E. R. Koch, T. G. Seidel, S. V. Gurevich, and J. Javaloyes. “Square-wave generation in vertical external-cavity Kerr-Gires-Tournois interferometers”. In: *Opt. Lett.* 47.17 (Sept. 2022), pp. 4343–4346. DOI: 10.1364/OL.468236. URL: http://opg.optica.org/ol/abstract.cfm?URI=ol-47-17-4343.

[Str18] S. H. Strogatz. *Nonlinear dynamics and chaos: with applications to physics, biology, chemistry, and engineering*. CRC press, 2018.

[LS88] C. C. Lin and L. A. Segel. *Mathematics applied to deterministic problems in the natural sciences*. SIAM, 1988.

[Arg+15] J. H. Argyris, G. Faust, M. Haase, and R. Friedrich. *An exploration of dynamical systems and chaos: completely revised and enlarged second edition*. Springer, 2015.

[Thi21] U. Thiele. *Lecture "Introduction to Numerical Continuation"*. Version 1. Feb. 2021. DOI: 10.5281/zenodo.4544848. URL: https://doi.org/10.5281/zenodo.4544848.

[KP02] S. G. Krantz and H. R. Parks. *The implicit function theorem: history, theory, and applications*. Springer Science & Business Media, 2002.

[TCF14] C. Tresser, P. Coullet, and E. de Faria. “Period doubling”. In: *Scholarpedia* 9.6 (2014). revision #142883, p. 3958. DOI: 10.4249/scholarpedia.3958.

[SJG22] T. G. Seidel, J. Javaloyes, and S. V. Gurevich. “A normal form for frequency combs and localized states in Kerr Gires-Tournois interferometers”. In: *Opt. Lett.* 47.12 (June 2022), pp. 2979–2982. DOI: 10.1364/OL.457777. URL: http://opg.optica.org/ol/abstract.cfm?URI=ol-47-12-2979.

[GT64] F. Gires and P. Tournois. “Interferometre utilisable pour la compression d’impulsions lumineuses modulees en frequence”. In: *C. R. Acad. Sci. Paris* 258 (1964), pp. 6112–6115.

[MB05] J. Mulet and S. Balle. “Mode-locking dynamics in electrically driven vertical-external-cavity surface-emitting lasers”. In: *IEEE journal of quantum electronics* 41.9 (2005), pp. 1148–1156.

[Bal98] S. Balle. “Simple analytical approximations for the gain and refractive index spectra in quantum well lasers”. In: *Phys. Rev. A* 57 (1998), pp. 1304–1312.

[Are+92] F. T. Arecchi, G. Giacomelli, A. Lapucci, and R. Meucci. “Two-dimensional representation of a delayed dynamical system”. In: *Phys. Rev. A* 45 (7 Apr. 1992), R4225–R4228. DOI: 10.1103/PhysRevA.45.R4225. URL: http://link.aps.org/doi/10.1103/PhysRevA.45.R4225.

[MG20] F. Marino and G. Giacomelli. “Spatiotemporal representation of long-delayed systems: An alternative approach”. In: *Phys. Rev. E* 102 (5 Nov. 2020), p. 052217. DOI: 10.1103/PhysRevE.102.052217. URL: https://link.aps.org/doi/10.1103/PhysRevE.102.052217.

[YG17] S. Yanchuk and G. Giacomelli. “Spatio-temporal phenomena in complex systems with time delays”. In: *Journal of Physics A: Mathematical and Theoretical* 50.10 (2017), p. 103001. URL: http://stacks.iop.org/1751-8121/50/i=10/a=103001.

[Wol+10] M. Wolfrum, S. Yanchuk, P. Hövel, and E. Schöll. "Complex dynamics in delay-differential equations with large delay". In: *The European Physical Journal Special Topics* 191.1 (2010), pp. 91–103.

[Niz04] M. Nizette. "Stability of square oscillations in a delayed-feedback system". In: *Phys. Rev. E* 70 (5 Nov. 2004), p. 056204. DOI: 10.1103/PhysRevE.70.056204. URL: http://link.aps.org/doi/10.1103/PhysRevE.70.056204.

[Mas+12] L. Mashal, G. Van der Sande, L. Gelens, J. Danckaert, and G. Verschaffelt. "Square-wave oscillations in semiconductor ring lasers with delayed optical feedback". In: *Optics express* 20.20 (2012), pp. 22503–22516.

[Fri+14] G. Friart, G. Verschaffelt, J. Danckaert, and T. Erneux. "All-optical controlled switching between time-periodic square waves in diode lasers with delayed feedback". In: *Opt. lett.* 39.21 (2014), pp. 6098–6101.

[Mul+07] J. Mulet, M. Giudici, J. Javaloyes, and S. Balle. "Square-wave switching by crossed-polarization gain modulation in vertical-cavity semiconductor lasers". In: *Phys. Rev. A* 76 (4 Oct. 2007), p. 043801. DOI: 10.1103/PhysRevA.76.043801. URL: http://link.aps.org/doi/10.1103/PhysRevA.76.043801.

[Mar+13] M. Marconi, J. Javaloyes, S. Barland, M. Giudici, and S. Balle. "Robust square-wave polarization switching in vertical-cavity surface-emitting lasers". In: *Phys. Rev. A* 87 (1 Jan. 2013), p. 013827. DOI: 10.1103/PhysRevA.87.013827. URL: http://link.aps.org/doi/10.1103/PhysRevA.87.013827.

[Gav+06] A. Gavrielides, T. Erneux, D. W. Sukow, G. Burner, T. McLachlan, J. Miller, and J. Amonette. "Square-wave self-modulation in diode lasers with polarization-rotated optical feedback". In: *Opt. Lett.* 31.13 (July 2006), pp. 2006–2008. DOI: 10.1364/OL.31.002006. URL: http://ol.osa.org/abstract.cfm?URI=ol-31-13-2006.

[Li+16] S. S. Li, X. Z. Li, J. P. Zhuang, G. Mezosi, M. Sorel, and S. C. Chan. "Square-wave oscillations in a semiconductor ring laser subject to counter-directional delayed mutual feedback". In: *Optics Letters* 41.4 (2016), pp. 812–815.

[Dil+19] M. Dillane, B. Tykalewicz, D. Goulding, B. Garbin, S. Barland, and B. Kelleher. "Square wave excitability in quantum dot lasers under optical injection". In: *Optics letters* 44.2 (2019), pp. 347–350.

[MN98] J. Mallet-Paret and R. D. Nussbaum. "Global continuation and asymptotic behaviour for periodic solutions of a differential-delay equation". In: *Comput. Math. Math. Phys.* 38.3 (1998), pp. 457–465. URL: http://dx.doi.org/10.1007/BF01790539.

[Gur18] S. V. Gurevich. *Runge-Kutta Methods*. 2018. URL: https://www.uni-muenster.de/Physik.TP/teaching/courses/numerical_methods_for_complex_systems_ii_ss2018.html.

[ELR02] K. Engelborghs, T. Luzyanina, and D. Roose. "Numerical Bifurcation Analysis of Delay Differential Equations Using DDE-BIFTOOL". In: *ACM Trans. Math. Softw.* 28.1 (Mar. 2002), pp. 1–21. ISSN: 0098-3500. DOI: 10.1145/513001.513002. URL: http://doi.acm.org/10.1145/513001.513002.

[PGG17] P. Parra-Rivas, D. Gomila, and L. Gelens. “Coexistence of stable dark- and bright-soliton Kerr combs in normal-dispersion resonators”. In: *Phys. Rev. A* 95 (5 May 2017), p. 053863. DOI: 10.1103/PhysRevA.95.053863. URL: https://link.aps.org/doi/10.1103/PhysRevA.95.053863.

[SGJ22] T. G. Seidel, S. V. Gurevich, and J Javaloyes. “Conservative solitons and reversibility in time delayed systems”. In: *Physical Review Letters* 128.8 (2022), p. 083901.

[BK07] J. Burke and E. Knobloch. “Homoclinic snaking: structure and stability”. In: *Chaos: An Interdisciplinary Journal of Nonlinear Science* 17.3 (2007), p. 037102.

[CH93] M. C. Cross and P. C. Hohenberg. “Pattern formation outside of equilibrium”. In: *Rev. Mod. Phys.* 65 (3 July 1993), pp. 851–1112. DOI: 10.1103/RevModPhys.65.851. URL: https://link.aps.org/doi/10.1103/RevModPhys.65.851.

[Pau97] C. A. H. Paul. “A user-guide to Archi: An explicit Runge-Kutta code for solving delay and neutral differential equations and Parameter Estimation Problems”. In: *MCCM Techical Report* 283 (1997).

B. Appendix

B.1. Runge-Kutta 4 for Time-delayed Systems

A very popular method is the fourth-order Runge-Kutta (RK4) method [Str18], which follows the scheme

$$x_{n+1} = x_n + \frac{h}{6}(k_1 + 2k_2 + 2k_3 + k_4). \tag{B.1}$$

The numbers k_i can be calculated for the system as

$$k_1 = f(x_n, x_{n-m_1}, ..., x_{n-m_N}, t_n), \tag{B.2}$$
$$k_2 = f(x_n + \frac{h}{2}k_1, x_{n-m_1+\frac{1}{2}}, ..., x_{n-m_N+\frac{1}{2}}, t_n + \frac{h}{2}), \tag{B.3}$$
$$k_3 = f(x_n + \frac{h}{2}k_2, x_{n-m_1+\frac{1}{2}}, ..., x_{n-m_N+\frac{1}{2}}, t_n + \frac{h}{2}), \tag{B.4}$$
$$k_4 = f(x_n + hk_3, x_{n-m_1+1}, ..., x_{n-m_N+1}, t_n + h). \tag{B.5}$$

As one can see the four approximations k_i for the derivative within the interval enter in Eq. (B.1) with different weights. Looking at k_1 one can recognize the Euler's method, which is based at the start of the time step and weighted with $\frac{h}{6}$. k_4 has the same weight and is located at the end of the interval. k_1 and k_4 together are a second order method, which improves the first order method, by taking the average derivative from both corner points of the time step. k_2 and k_3 are based in the middle of the interval and are each weighted $\frac{h}{3}$. In the DDE case, these two terms pose a problem, they also depend on half steps from the past, as well as their derivative.
A Hermite interpolation [Sch21] can be implemented to solve this problem as it has been used in Runge-Kutta based methods for DDEs before, such as ARCHI [Pau97]. It expresses the value $x_{n-m_i+\frac{1}{2}}$ as function of the two neighbored values x_{n-m_i} and x_{n-m_i+1}, as well as their derivatives. Therefor the coefficients of a third-order polynomial

$$p(t) = \alpha_0 + \alpha_1 t + \alpha_2 t^2 + \alpha_3 t^3, \tag{B.6}$$
$$\dot{p}(t) = \alpha_1 + 2\alpha_2 t + 3\alpha_3 t^2, \tag{B.7}$$

have to be calculated. The polynomial has to agree with the two values x_{n-m_i} and x_{n-m_i+1} as well as their derivatives at the respective relative time values. The origin t=0 can be chosen freely and is best placed at the half step, yielding

$$x_{n-m_i+\frac{1}{2}} = \alpha_0. \tag{B.8}$$

Since the known points x_{n-m_i} and x_{n-m_i+1} are now located at $t = \pm\frac{h}{2}$ on the polynomial,

$$x_{n-m_i} = \alpha_0 - \alpha_1\frac{h}{2}t + \alpha_2\frac{h^2}{4} - \alpha_3\frac{h^3}{8}, \tag{B.9}$$
$$\dot{x}_{n-m_i} = \alpha_1 - \alpha_2 h + 3\alpha_3\frac{h^2}{4}, \tag{B.10}$$
$$x_{n-m_i+1} = \alpha_0 + \alpha_1\frac{h}{2}t + \alpha_2\frac{h^2}{4} + \alpha_3\frac{h^3}{8}, \tag{B.11}$$
$$\dot{x}_{n-m_i+1} = \alpha_1 + \alpha_2 h + 3\alpha_3\frac{h^2}{4}. \tag{B.12}$$

is found. The sum of the Eqs. B.9 and B.11 leads to

$$2\alpha_0 + 2\alpha_2 \frac{h^2}{4} = x_{n-m_i+1} + x_{n-m_i}, \tag{B.13}$$

which eliminates α_1 and α_3 Finding the difference between the remaining two equations for the derivatives leads to

$$4\alpha_2 \frac{h}{2} = \dot{x}_{n-m_i+1} - \dot{x}_{n-m_i}, \tag{B.14}$$

which eliminates α_2, if inserted into Eq. (B.13). The result is

$$x_{n-m_i+\frac{1}{2}} = \frac{x_{n-m_i} + x_{n-m_i+1}}{2} + \frac{h}{8}(\dot{x}_{n-m_i} - \dot{x}_{n-m_i+1}). \tag{B.15}$$

B.2. Normal Form Calculations

In this appendix section the steps from the calculation of the normal form are contained in more detail. Inserting only f and the nonlinearity, the equation turns to

$$\begin{aligned}\epsilon\mathcal{T}\left[E(t) + \eta E(t-1)\right] =& -\left[1 + i\delta\right]E(t) + \left[h - 1 - i\delta\right]\eta E(t-1) + hY_0\sqrt{1-\eta^2} \\ &+ \epsilon^2 f(iR_0 - I_0)(E(t) + \eta E(t-1)) \\ &+ \epsilon^3 f(iR_1 - I_1)\left(D(t)E(t) + \eta D(t-1)E(t-1)\right). \end{aligned} \tag{B.16}$$

This can be solved for $E(t)$:

$$\begin{aligned}E(t) =& \frac{[h-1-\epsilon^2 fI_0] - i[\delta - \epsilon^2 fR_0]}{[1+\epsilon^2 fI_0] + i[\delta - \epsilon^2 fR_0]}\eta E(t-1) \\ &- \epsilon\mathcal{T}\frac{E(t) + \eta E(t-1)}{[1+\epsilon^2 fI_0] + i[\delta - \epsilon^2 fR_0]} + hY_0\frac{\sqrt{1-\eta^2}}{[1+\epsilon^2 fI_0] + i[\delta - \epsilon^2 fR_0]} \\ &+ \epsilon^3\frac{f(iR_1 - I_1)}{[1+\epsilon^2 fI_0] + i[\delta - \epsilon^2 fR_0]}\left(D(t)E(t) + \eta D(t-1)E(t-1)\right). \end{aligned} \tag{B.17}$$

In the next step the term $W = \frac{[h-1-\epsilon^2 fI_0] - i[\delta - \epsilon^2 fR_0]}{[1+\epsilon^2 fI_0] + i[\delta - \epsilon^2 fR_0]}$ is expanded for small ϵ. Alongside the first parameter $h = 2$ can be inserted. So the expansion turns into

$$W = \frac{1 - i\delta}{1 + i\delta} - \epsilon^2\frac{2(fI_0 - ifR_0)}{(1+i\delta)^2} + \mathcal{O}(4) \tag{B.18}$$

$$= \frac{1 - i\delta}{1 + i\delta} - \epsilon^2 2W_1 + \mathcal{O}(4). \tag{B.19}$$

The same way $V = \frac{1}{[1+\epsilon^2 fI_0] + i[\delta - \epsilon^2 fR_0]}$ can be written as

$$V = \frac{1}{1 + i\delta} - \epsilon^2\frac{fI_0 - ifR_0}{(1+i\delta)^2} + \mathcal{O}(\epsilon^4) \tag{B.20}$$

$$= \frac{1}{1 + i\delta} - \epsilon^2 W_1 + \mathcal{O}(\epsilon^4). \tag{B.21}$$

These two expansions where able to remove any orders of ϵ from the denominators which is important to treat the orders of ϵ separately. Including the found expansions leads to

$$\begin{aligned}E =& \frac{1 - i\delta}{1 + i\delta}\eta E(t-1) - \epsilon^2 2W_1\eta E(t-1) - \epsilon\mathcal{T}\frac{E + \eta E(t-1)}{1 + i\delta} + \epsilon^3 W_1\mathcal{T}\left(E(t) + \eta E(t-1)\right) \\ &+ 2Y_0\frac{\sqrt{1-\eta^2}}{1 + i\delta} + \epsilon^3\frac{f(iR_1 - I_1)}{1 + i\delta}\left(D(t)E(t) + \eta D(t-1)E(t-1)\right). \end{aligned} \tag{B.22}$$

The expansion of W leads to a new term, which is of $\mathcal{O}(\epsilon^2)$ describing the small shift in δ and the constant due to the active medium. The expansion of V introduces a new term of $\mathcal{O}(\epsilon^3)$. Since all other terms containing V are at least $\mathcal{O}(\epsilon^2)$, only the $\frac{1}{1+i\delta}$ survives. Especially the injection term, though not yet obvious, will be of $\mathcal{O}(\epsilon^2)$ as well.

The term $\frac{1-i\delta}{1+i\delta} = e^{i\theta}$ is a phase since $|\frac{1-i\delta}{1+i\delta}| = 1$. This leads to $\theta = -2\arctan(\delta)$, using the arg function again. Assuming small values of δ the imaginary part becomes small as well. This enables an expansion for small θ into $\theta = \epsilon^2\theta_2 + \epsilon^3\theta_3$. In total the expansion is

$$\begin{aligned}\eta e^{i\theta} &= (1+\epsilon^2\eta_2)(1+\epsilon^2 i\theta_2 + \epsilon^3 i\theta_3) && \text{(B.23)}\\ &= 1 + \epsilon^2(\eta_2 + i\theta_2) + \epsilon^3 i\theta_3 + \mathcal{O}(\epsilon^4), && \text{(B.24)}\end{aligned}$$

resulting in two new terms. Now one can insert $\eta = 1 + \epsilon^2\eta_2$ and $Y_0 = \epsilon\gamma_1 + \epsilon^2\gamma_2$ which leads to

$$\begin{aligned}E =& E(t-1) - \epsilon\mathcal{T}\frac{E + (1+\epsilon^2\eta_2)E(t-1)}{1+i\delta} - \epsilon^2(-\eta_2 + 2W_1 - i\theta_2)E(t-1)\\ &+ \epsilon(\gamma_1 + \epsilon\gamma_2)\frac{2\sqrt{1-\eta^2}}{1+i\delta} + \epsilon^3 W_1\mathcal{T}\left(E(t) + E(t-1)\right)\\ &+ \epsilon^3\frac{f(iR_1 - I_1)}{1+i\delta}\left(D(t)E(t) + D(t-1)E(t-1)\right) \qquad \text{(B.25)}\end{aligned}$$

A Taylor simplifies the square root

$$\begin{aligned}\sqrt{1-\eta^2} &= \sqrt{1-(1+\epsilon^2\eta_2)^2} && \text{(B.26)}\\ &= \sqrt{-2\epsilon^2\eta_2 + \epsilon^4\eta_2^2} && \text{(B.27)}\\ &= \epsilon\sqrt{-2\eta_2 + \epsilon^2\eta_2^2} && \text{(B.28)}\\ &= \epsilon\sqrt{-2\eta_2} + \mathcal{O}(\epsilon^3). && \text{(B.29)}\end{aligned}$$

Inserting it in the injection term reveals its true order of ϵ. At this point the equation has turned into

$$\begin{aligned}E =& E(t-1) - \epsilon\mathcal{T}\frac{E + (1+\epsilon^2\eta_2)E(t-1)}{1+i\delta} - \epsilon^2(-\eta_2 + 2W_1 - i\theta_2)E(t-1)\\ &+ \epsilon^2(\gamma_1 + \epsilon\gamma_2)\frac{2\sqrt{-2\eta_2}}{1+i\delta} + \epsilon^3 W_1\mathcal{T}\left(E(t) + E(t-1)\right)\\ &+ \epsilon^3\frac{f(iR_1 - I_1)}{1+i\delta}\left(D(t)E(t) + D(t-1)E(t-1)\right). \qquad \text{(B.30)}\end{aligned}$$

This result shall now be reduced by collecting and redefining constants. At this point

one has to ensure that no orders of ϵ are included in the new constants

$$L_2 = -\eta_2 + 2W_1 - i\theta_2 \tag{B.31}$$

$$\Gamma_2 = \gamma_1 \frac{2\sqrt{-2\eta_2}}{1+i\delta}, \tag{B.32}$$

$$\Gamma_3 = \gamma_2 \frac{2\sqrt{-2\eta_2}}{1+i\delta}, \tag{B.33}$$

$$N_3 = \frac{f(iR_1 - I_1)}{1+i\delta}, \tag{B.34}$$

$$V_0 = \frac{1}{1+i\delta}, \tag{B.35}$$

$$V_0^* = \frac{1}{1-i\delta}. \tag{B.36}$$

The reduced equation is

$$\begin{aligned} E =& E(t-1) - \epsilon V_0 \mathcal{T}(E + E(t-1)) - \epsilon^2 L_2 E(t-1) + \epsilon^2 \Gamma_1 + \epsilon^3 \Gamma_2 \\ &+ \epsilon^3(-V_0\eta_2 + W_1)\mathcal{T}E(t-1) + \epsilon^3 W_1 \mathcal{T}E(t) + \epsilon^3 N_3 \left(D(t)E(t) + D(t-1)E(t-1)\right). \end{aligned} \tag{B.37}$$

To improve the previous result a small trick can be done. Since

$$e^{i\theta}\frac{1+i\delta}{1-i\delta} = 1, \tag{B.38}$$

a 1 can be introduced without limiting generality an expanded into

$$1 = \frac{1+i\delta}{1-i\delta}(1 + \epsilon^2 i\theta_2 + \epsilon^3 i\theta_3), \tag{B.39}$$

$$= \frac{V_0^*}{V_0}(1 + \epsilon^2 i\theta_2 + \epsilon^3 i\theta_3). \tag{B.40}$$

This leads to

$$\begin{aligned} E =& E(t-1) - \epsilon\mathcal{T}(V_0 E + V_0^* E(t-1)) - \epsilon^2 L_2 E(t-1) + \epsilon^2 \Gamma_1 \\ &+ \epsilon^3 \Gamma_2 + \epsilon^3(-V_0^*\eta_2 + W_1 - iV_0^*\theta_2)\mathcal{T}E(t-1) + \epsilon^3 W_1 \mathcal{T}E(t) \\ &+ \epsilon^3 N_3 \left(D(t)E(t) + D(t-1)E(t-1)\right) + \mathcal{O}(\epsilon^4) \end{aligned} \tag{B.41}$$

$$\begin{aligned} =& E(t-1) - \epsilon\mathcal{T}(V_0 E + V_0^* E(t-1)) - \epsilon^2 L_2 E(t-1) + \epsilon^2 \Gamma_1 \\ &+ \epsilon^3 \Gamma_2 + \epsilon^3(-V_0^*\eta_2 + \frac{V_0^*}{V_0}W_1 - iV_0^*\theta_2)\mathcal{T}E(t-1) + \epsilon^3 W_1 \mathcal{T}E(t) \\ &+ \epsilon^3 N_3 \left(D(t)E(t) + D(t-1)E(t-1)\right) + \mathcal{O}(\epsilon^4). \end{aligned} \tag{B.42}$$

Another trick was used by introducing $\frac{V_0^*}{V_0}$ in a third order term since the correction terms fall into $\mathcal{O}(\epsilon^5)$. The usefulness of this step will become clear later. Now

$$L_3 = (-V_0^*\eta_2 + \frac{V_0^*}{V_0}W_1 - iV_0^*\theta_2), \tag{B.43}$$

is introduced, yielding

$$\begin{aligned} E =& E(t-1) - \epsilon\mathcal{T}(V_0 E + V_0^* E(t-1)) - \epsilon^2 L_2 E(t-1) + \epsilon^2 \Gamma_1 \\ &+ \epsilon^3 \Gamma_2 + \epsilon^3 L_3 \mathcal{T}E(t-1) + \epsilon^3 W_1 \mathcal{T}E(t) + \epsilon^3 N_3 \left(D(t)E(t) + D(t-1)E(t-1)\right). \end{aligned} \tag{B.44}$$

Time Operator, Shift Operator and Field Expansion:
Now the new time scales and the shift operator will be included explicitly:

$$\begin{aligned} E(t_0) =& \mathcal{S}E(t_0-1) - \epsilon\mathcal{T}(V_0E(t_0) + V_0^*\mathcal{S}E(t_0-1)) - \epsilon^2 L_2\mathcal{S}E(t_0-1) + \epsilon^2\Gamma_2 + \epsilon^3\Gamma_3 \\ &+ \epsilon^3 L_3\mathcal{T}E(t_0-1) + \epsilon^3 W_1\mathcal{T}E(t_0) + \epsilon^3 N_3\left(D(t_0)E(t_0) + D(t_0-1)E(t_0-1)\right) \\ &+ \mathcal{O}(\epsilon^4). \end{aligned} \tag{B.45}$$

For the third order terms, only $S_0 = 1$ enters. Using this as well as the time derivative operator $\mathcal{T}$ leads to

$$\begin{aligned} E(t_0) =& \mathcal{S}E(t_0-1) - \epsilon(\mathcal{T}_0 + \epsilon\mathcal{T}_1 + \epsilon^2\mathcal{T}_2(V_0E(t_0) + V_0^*\mathcal{S}E(t_0-1)) \\ &- \epsilon^2 L_2\mathcal{S}E(t_0-1) + \epsilon^2\Gamma_2 + \epsilon^3\Gamma_3 + \epsilon^3 L_3\mathcal{T}E(t_0-1) \\ &+ \epsilon^3 W_1\mathcal{T}_0E(t_0) + \epsilon^3 N_3\left(D(t_0)E(t_0) + D(t_0-1)E(t_0-1)\right) \quad + \mathcal{O}(\epsilon^4), \end{aligned} \tag{B.46}$$

and with the full shift operator

$$\begin{aligned} E(t_0) - E(t_0-1) =& \epsilon\left(\left[S_1 - V_0^*T_0\right]E(t_0-1) - V_0T_0E(t_0)\right) \\ &+ \epsilon^2\left(\left[S_2 - V_0^*T_0S_1 - V_0^*T_1 - L_2\right]E(t_0-1) - V_0T_1E(t_0) + \Gamma_2\right) \\ &+ \epsilon^3\left(\left[S_3 - V_0^*T_0S_2 - V_0^*T_1S_1 - V_0^*T_2 - L_2S_1 + L_3\partial_0\right]E(t_0-1) + \Gamma_3\right. \\ &\quad \left. + \left[W_1\partial_0 - V_0T_2\right]E(t_0) + N_3(D(t_0)E(t_0) + D(t_0-1)E(t_0-1))\right) \\ &+ \mathcal{O}(\epsilon^4). \end{aligned} \tag{B.47}$$

Finally the field expansion $E(t) = E_0(t) + \epsilon E_1(t) + \epsilon^2 E_2(t) + \epsilon^3 E_3(t)$ yields

$$\begin{aligned} &\left(E_0(t_0) - E_0(t_0-1)\right) \\ &+\epsilon\left(E_1(t_0) - E_1(t_0-1)\right) \\ &+\epsilon^2\left(E_2(t_0) - E_2(t_0-1)\right) \\ &+\epsilon^3\left(E_3(t_0) - E_3(t_0-1)\right) =& \epsilon\left(\left[S_1 - V_0^*T_0\right]E_0(t_0-1) - V_0T_0E_0(t_0)\right) \\ &&+ \epsilon^2\left(\left[S_1 - V_0^*T_0\right]E_1(t_0-1) - V_0T_0E_1(t_0)\right) \\ &&+ \left[S_2 - V_0^*T_0S_1 - V_0^*T_1 - L_2\right]E_0(t_0-1) - V_0T_1E_0(t_0) + \Gamma_2\right) \\ &&+ \epsilon^3\left(\left[S_1 - V_0^*T_0\right]E_2(t_0-1) - V_0T_0E_2(t_0)\right) \\ &&+ \left[S_2 - V_0^*T_0S_1 - V_0^*T_1 - L_2\right]E_1(t_0-1) - V_0T_1E_1(t_0) + \Gamma_3 \\ &&+ \left[S_3 - V_0^*T_0S_2 - V_0^*T_1S_1 - V_0^*T_2 - L_2S_1 + L_3\partial_0\right]E_0(t_0-1) \\ &&+ \left[W_1\partial_0 - V_0T_2\right]E_0(t_0) + N_3(D(t_0)E_0(t_0) + D(t_0-1)E_0(t_0-1))\right) \\ &&+ \mathcal{O}(\epsilon^4). \end{aligned} \tag{B.48}$$

This results in the full equation, which has to be solved separated by orders of ϵ.

B.3. Normal Form Orders in Detail

$\mathcal{O}(\epsilon^0)$**:**

$$E_0(t_0) - E_0(t_0-1) = 0. \tag{B.49}$$

This equation describes a simple periodic solution.

$\mathcal{O}(\epsilon^1)$**:**
Using the results from $\mathcal{O}(\epsilon^0)$, the next order becomes

$$E_1(t_0) - E_1(t_0-1) = [S_1 - V_0^* T_0]\, E_0(t_0-1) - V_0 T_0 E_0(t_0) \tag{B.50}$$
$$= (S_1 - V_0^* T_0 - V_0 T_0) E_0(t_0) \tag{B.51}$$
$$= \left(-\omega_1 - \frac{1 - i\delta + 1 + i\delta}{\delta^2 + 1}\right) \partial_0 E_0(t_0) \tag{B.52}$$
$$= \left(-\omega_1 - \frac{2}{\delta^2 + 1}\right) \partial_0 E_0(t_0). \tag{B.53}$$

To get periodic solutions in every order the parameters can be chosen in a way that the right-hand side vanishes. This also clarifies the meaning of the expansion in ω as compensation for potential drift. Without the first order term $\omega_1 \partial_0 E_0(t_0)$ a nonvanishing drift of E_0 on the time scale t_0 is observed. The drift is compensated through the result for the small frequency correction $\epsilon\omega_1$ by choosing:

$$\omega_1 = \frac{-2}{1 + \delta^2}. \tag{B.54}$$

Note as well

$$V_0 + V_0^* = -\omega_1 \tag{B.55}$$

for later simplifications.
$\mathcal{O}(\epsilon^2)$**:**
Collecting the second order leads to

$$\begin{aligned} E_2(t_0) - E_2(t_0-1) = &[S_1 - V_0^* T_0]\, E_1(t_0-1) - V_0 T_0 E_1(t_0)) \\ &+ [S_2 - V_0^* T_0 S_1 - V_0^* T_1 - L_2]\, E_0(t_0-1) \\ &- V_0 T_1 E_0(t_0) + \Gamma_2. \end{aligned} \tag{B.56}$$

Then the result from $\mathcal{O}(\epsilon^0)$ can be included, to find

$$[S_1 - V_0^* T_0 - V_0 T_0] E_1(t_0 - 1) = 0, \tag{B.57}$$

which can be solved with the result for ω_1 from $\mathcal{O}(\epsilon^1)$. The remaining terms are

$$0 = [S_2 - V_0^* T_0 S_1 - V_0^* T_1 - V_0 T_1 - L_2] E_0(t_0) + \Gamma_2 \tag{B.58}$$
$$= \left[\frac{\omega_1^2}{2}\partial_0^2 - \omega_2 \partial_0 - \partial_2 + \frac{\omega_1}{1 - i\delta}\partial_0^2 - \frac{\omega_1}{1 - i\delta}\partial_0 - \frac{\omega_1}{1 + i\delta}\partial_0 - L_2\right] E_0(t_0) + \gamma_1 \frac{2\sqrt{-2\eta_2}}{1 + i\delta} \tag{B.59}$$
$$= \left[-\omega_2 - \frac{2\omega_1}{1 + \delta^2}\right] \partial_0 E_0(t_0) + \left[\frac{\omega_1^2}{2} + \frac{\omega_1}{1 - i\delta}\right] \partial_0^2 E_0(t_0) + (-\partial_2 - L_2)\, E_0(t_0) + \Gamma_2. \tag{B.60}$$

The first bracket yields

$$\omega_2 = \omega_1^2, \tag{B.61}$$

while the diffusion term reduces to

$$\frac{\omega_1^2}{2} + \frac{\omega_1}{1 - i\delta} = \frac{\omega_1^2}{2} + \frac{2\omega(1 + i\delta)}{2(1 + \delta^2)} \tag{B.62}$$
$$= \frac{\omega_1^2}{2} - \frac{\omega_1^2}{2}(1 + i\delta) \tag{B.63}$$
$$= -i\delta \frac{\omega_1^2}{2}. \tag{B.64}$$

The resulting PDE

$$\partial_2 E_0(t_0) = \left[-i\delta\frac{\omega_1^2}{2}\partial_0^2 - L_2\right] E_0(t_0) + \Gamma_2 \tag{B.65}$$

can be used as solvability condition in later orders. The operator L_2 contains the first term from the nonlinearity. But the third-order nonlinearity does not enter until $\mathcal{O}(\epsilon^3)$. With all the results from above, one can write yet again:

$$E_2(t_0) = E_2(t_0 - 1). \tag{B.66}$$

$\mathcal{O}(\epsilon^3)$**:**
One finds

$$\begin{aligned} E_3(t_0) - E_3(t_0-1) =& \left[S_1 - V_0^* T_0\right] E_2(t_0-1) - V_0 T_0 E_2(t_0)) \\ &+ \left[S_2 - V_0^* T_0 S_1 - V_0^* T_1 - L_2\right] E_1(t_0-1) - V_0 T_1 E_1(t_0) + \Gamma_3 \\ &+ \left[S_3 - V_0^* T_0 S_2 - V_0^* T_1 S_1 - V_0^* T_2 - L_2 S_1 + L_3\partial_0\right] E_0(t_0-1) \\ &+ \left[W_1\partial_0 - V_0 T_2\right] E_0(t_0) + N_3(D(t_0)E_0(t_0) + D(t_0-1)E_0(t_0-1)). \end{aligned} \tag{B.67}$$

Collecting the results from the first orders, a few simplifications can be done already

$$0 = \left[S_1 - V_0^* T_0 - V_0 T_0\right] E_2(t_0), \tag{B.68}$$

is an equation that has already appeared before. It is solved by $\omega_1 = \frac{-2}{1+\delta^2}$. Next

$$\begin{aligned} 0 =& [S_2 - V_0^* T_0 S_1 - (V_0 + V_0^*) T_1 - L_2] E_1(t_0) + \Gamma_3 + 2N_3 D(t_0) E_0(t_0) \\ &+ [S_3 - V_0^* T_0 S_2 - V_0^* T_1 S_1 - (V_0^* + V_0) T_2 - L_2 S_1 + L_3\partial_0 + W_1\partial_0] E_0(t_0) \qquad \text{(B.69)} \\ =& [S_2 - V_0^* T_0 S_1 + \omega_1 T_1 - L_2] E_1(t_0) + \Gamma_3 + 2N_3 D(t_0) E_0(t_0) \\ &+ [S_3 - V_0^* T_0 S_2 - V_0^* T_1 S_1 + \omega_1 T_2 - L_2 S_1 + L_3\partial_0 + W_1\partial_0] E_0(t_0) \qquad \text{(B.70)} \end{aligned}$$

is found. This equation can be brought into the more organized form

$$\partial_3 E_0 + \partial_2 E_1 = [2N_3 D(t_0) + S_3 - V_0^* T_0 S_2 - V_0^* T_1 S_1 + \omega_1 T_2 - L_2 S_1 + L_3\partial_0 + W_1\partial_0] E_0(t_0) \tag{B.71}$$

$$= [\mathcal{N}D + S_3 - V_0^* T_0 S_2 - V_0^* T_1 S_1 + \omega_1 T_2 - L_2 S_1 + L_3\partial_0 + W_1\partial_0] E_0(t_0) \tag{B.72}$$

$$\begin{aligned} =& \left[-\omega_3 + \omega_1\omega_2 + L_2\omega_1 + L_3 + W_1\right] \partial_0 E_0(t_0) \\ &+ [\omega_1\omega_2 - V_0^*\omega_1^2 + V_0^*\omega_2]\partial_0^2 E_0(t_0) \qquad \text{(B.73)} \\ &+ \left[\frac{-\omega_1^3}{6} - V_0^*\frac{\omega_1^2}{2}\right]\partial_0^3 E_0(t_0) \\ &+ \left[\omega_1\partial_0 + V_0^*\partial_0 + \omega_1\right]\partial_2 E_0(t_0) \\ &+ \mathcal{N}DE_0 + \left[-i\delta\frac{\omega_1^2}{2}\partial_0^2 - L_2\right] E_1(t_0) + \Gamma_3, \qquad \text{(B.74)} \end{aligned}$$

where $\mathcal{N} = 2N_3$ has been used. For $\partial_2 E_0$ the solvability condition from the last order can be inserted, yielding

$$\begin{aligned}
\partial_3 E_0 + \partial_2 E_1 =& \left[-\omega_3 + \omega_1\omega_2 + L_2\omega_1 + L_3 + W_1\right]\partial_0 E_0(t_0) \\
&+ [\omega_1\omega_2 + V_0^*\omega_1^2 + V_0^*\omega_2]\partial_0^2 E_0(t_0) \\
&+ \left[\frac{-\omega_1^3}{6} - V_0^*\frac{\omega_1^2}{2}\right]\partial_0^3 E_0(t_0) \\
&+ [\omega_1\partial_1 + V_0^*\partial_0 + \omega_1]\left(\left[-i\delta\frac{\omega_1^2}{2}\partial_0^2 - L_2\right]E_0(t_0) + \Gamma_2\right) \\
&+ \mathcal{N}DE_0 + \left[-i\delta\frac{\omega_1^2}{2}\partial_0^2 - L_2\right]E_1(t_0) + \Gamma_3 \qquad \text{(B.75)} \\
=& \left[-\omega_3 + \omega_1\omega_2 + L_2\omega_1 + L_3 + W_1 - V_0^*L_2 - \omega_1 L_2\right]\partial_0 E_0(t_0) \\
&+ [\omega_1\omega_2 + V_0^*\omega_1^2 + V_0^*\omega_2 - i\delta\frac{\omega_1^3}{2}]\partial_0^2 E_0(t_0) \\
&+ \left[\frac{-\omega_1^3}{6} - V_0^*\frac{\omega_1^2}{2} - i\delta V_0^*\frac{\omega_1^2}{2} - i\delta\frac{\omega_1^3}{2}\right]\partial_0^3 E_0(t_0) \\
&+ [\mathcal{N}D - \omega_1 L_2]E_0 + \left[-i\delta\frac{\omega_1^2}{2}\partial_0^2 - L_2\right]E_1(t_0) + \Gamma_3 + \omega_1\Gamma_2. \qquad \text{(B.76)}
\end{aligned}$$

For ω_3 this orders drift correction term reduces to $\omega_3 = \omega_1^3$ since the three other terms, all coming from the nonlinearity, cancel out:

$$\begin{aligned}
\omega_3 &= \omega_1^3 + L_2\omega_1 + L_3 + W_1 - V_0^*L_2 - \omega_1 L_2 && \text{(B.77)} \\
&= \omega_1^3 + L_3 + W_1 - V_0^*L_2 && \text{(B.78)} \\
&= \omega_1^3 - V_0^*\eta_2 + \frac{V_0^*}{V_0}W_1 - iV_0^*\theta_2 + W_1 + V_0^*\eta_2 - 2V_0^*W_1 + iV_0^*\theta_2 && \text{(B.79)} \\
&= \omega_1^3 + W_1\left(\frac{V_0^*}{V_0} + 1 - 2V_0^*\right) && \text{(B.80)} \\
&= \omega_1^3 + W_1\left(\frac{1+i\delta}{1-i\delta} + \frac{1-i\delta}{1-i\delta} - \frac{2}{1-i\delta}\right) && \text{(B.81)} \\
&= \omega_1^3. && \text{(B.82)}
\end{aligned}$$

This simplification is possible due to the previously mentioned trick with the factor $\frac{V_0^*}{V_0}$. Otherwise a complex frequency ω_3 would be found.
The diffusion simplifies to

$$[\omega_1\omega_2 + V_0^*\omega_1^2 + V_0^*\omega_2 - i\delta\frac{\omega_1^3}{2}]\partial_0^2 E_0(T_0) = -i\frac{3\delta}{2}\omega_1^3\partial_0^2 E_0(t_0), \qquad \text{(B.83)}$$

while the third order dispersion can be written as

$$\begin{aligned}
\left[\frac{-\omega_1^3}{6} - V_0^*\frac{\omega_1^2}{2} - i\delta V_0^*\frac{\omega_1^2}{2} - i\delta\frac{\omega_1^3}{2}\right]\partial_0^3 E_0(t_0) &= \left[\frac{-\omega_1^3}{6} - V_0^*\frac{\omega_1^2}{2} - i\delta\frac{\omega_1^2}{2}(V_0^* + \omega_1)\right]\partial_0^3 E_0(t_0) && \text{(B.84)} \\
&= \left[\frac{-\omega_1^3}{6} - V_0^*\frac{\omega_1^2}{2} + i\delta\frac{\omega_1^2}{2}\frac{1-i\delta}{1+\delta^2}\right]\partial_0^3 E_0(t_0) && \text{(B.85)} \\
&= \frac{1-3\delta^2}{12}\omega_1^3\partial_0^3 E_0(t_0). && \text{(B.86)}
\end{aligned}$$

The final equation for the third order containing all simplifications, has the form

$$\begin{aligned}\partial_3 E_0 + \partial_2 E_1 = &- i\frac{3\delta}{2}\omega_1^3\partial_0^2 E_0(t_0) + \frac{1-3\delta^2}{12}\omega_1^3\partial_0^3 E_0(t_0) \\ &+ [\mathcal{N}D - \omega_1 L_2]E_0 + \left[-i\delta\frac{\omega_1^2}{2}\partial_0^2 - L_2\right] E_1(t_0) + \Gamma_3 + \omega_1\Gamma_2. \qquad \text{(B.87)}\end{aligned}$$

Declaration of Academic Integrity

I hereby confirm that this thesis on

"Square-waves and pulsating dynamics in time-delayed active micro-cavities"

is solely my own work and that I have used no sources or aids other than the ones stated. All passages in my thesis for which other sources, including electronic media, have been used, be it direct quotes or content references, have been acknowledged as such and the sources cited.

_____

(Date and Signature of Student)

I agree to have my thesis checked in order to rule out potential similarities with other works and to have my thesis stored in a database for this purpose.

_____

(Date and Signature of Student)